

Katteden Kamiev

DESIGN AND TESTING OF AN ARMATURE- REACTION-COMPENSATED PERMANENT MAGNET SYNCHRONOUS GENERATOR FOR ISLAND OPERATION

Thesis for the degree of Doctor of Science (Technology) to be presented with due permission for public examination and criticism in the Auditorium 1381 at Lappeenranta University of Technology, Lappeenranta, Finland on the 15th of November, 2013, at noon.

Acta Universitatis
Lappeenrantaensis 539

Supervisors Professor Juha Pyrhönen
Department of Electrical Engineering
LUT Institute of Energy Technology (LUT Energy)
LUT School of Technology
Lappeenranta University of Technology
Finland

D.Sc. Janne Nerg
Department of Electrical Engineering
LUT Institute of Energy Technology (LUT Energy)
LUT School of Technology
Lappeenranta University of Technology
Finland

Reviewers Professor Sergey Shirinskii
Department of Electromechanics
National Research University
“Moscow Power Engineering Institute”
Russia

D.Sc. Yacine Amara
Department of Electrical Engineering
University of Le Havre
France

Opponents Professor Sergey Shirinskii
Department of Electromechanics
National Research University
“Moscow Power Engineering Institute”
Russia

D.Sc. Yacine Amara
Department of Electrical Engineering
University of Le Havre
France

ISBN 978-952-265-485-4
ISBN 978-952-265-486-1 (PDF)
ISSN-L 1456-4491
ISSN 1456-4491
Lappeenrannan teknillinen yliopisto
Yliopistopaino 2013

Abstract

Katteden Kamiev

Design and testing of an armature-reaction-compensated permanent magnet synchronous generator for island operation

Lappeenranta 2013

140 pages

Acta Universitatis Lappeenrantaensis 539

Diss. Lappeenranta University of Technology

ISBN 978-952-265-485-4, ISBN 978-952-265-486-1 (PDF)

ISSN-L 1456-4491, ISSN 1456-4491

At present, permanent magnet synchronous generators (PMSGs) are of great interest. Since they do not have electrical excitation losses, the highly efficient, lightweight and compact PMSGs equipped with damper windings work perfectly when connected to a network. However, in island operation, the generator (or parallel generators) alone is responsible for the building up of the network and maintaining its voltage and reactive power level. Thus, in island operation, a PMSG faces very tight constraints, which are difficult to meet, because the flux produced by the permanent magnets (PMs) is constant and the voltage of the generator cannot be controlled. Traditional electrically excited synchronous generators (EESGs) can easily meet these constraints, because the field winding current is controllable. The main drawback of the conventional EESG is the relatively high excitation loss.

This doctoral thesis presents a study of an alternative solution termed as a hybrid excitation synchronous generator (HESG). HESGs are a special class of electrical machines, where the total rotor current linkage is produced by the simultaneous action of two different excitation sources: the electrical and permanent magnet (PM) excitation. An overview of the existing HESGs is given. Several HESGs are introduced and compared with the conventional EESG from technical and economic points of view.

In the study, the armature-reaction-compensated permanent magnet synchronous generator with alternated current linkages (ARC-PMSG with ACL) showed a better performance than the other options. Therefore, this machine type is studied in more detail. An electromagnetic design and a thermal analysis are presented. To verify the operation principle and the electromagnetic design, a down-sized prototype of 69 kVA apparent power was built. The experimental results are demonstrated and compared with the predicted ones. A prerequisite for an ARC-PMSG with ACL is an even number of pole pairs ($p = 2, 4, 6, \dots$) in the machine. Naturally, the HESG technology is not limited to even-pole-pair machines. However, the analysis of machines with $p = 3, 5, 7, \dots$ becomes more complicated, especially if analytical tools are used, and is outside the scope of this thesis.

The contribution of this study is to propose a solution where an ARC-PMSG replaces an EESG in electrical power generation while meeting all the requirements set for generators given for instance by ship classification societies, particularly as regards island operation.

The maximum power level when applying the technology studied here is mainly limited by the economy of the machine. The larger the machine is, the smaller is the efficiency benefit. However, it seems that machines up to ten megawatts of power could benefit from the technology. However, in low-power applications, for instance in the 500 kW range, the efficiency increase can be significant.

Keywords: armature-reaction-compensated permanent magnet synchronous generator, island operation, hybrid excitation synchronous generator, permanent magnet synchronous generator, radial flux, synchronous generator

UDC 621.313.8:621.313.322:51.001.57

Acknowledgements

This work was carried out at the Department of Electrical Engineering, the Institute of Energy Technology (LUT Energy) at Lappeenranta University of Technology, Finland, between 2008 and 2013. The research work was funded by LUT DPEEE FiDiPro Fellowship in Permanent Magnet Machines.

I would like to thank my supervisors, Professor Juha Pyrhönen and D.Sc. Janne Nerg, for their valuable guidance and new knowledge obtained during this work. I wish to express my thanks to Professor Valeriy Zaboin from Saint-Petersburg State Polytechnical University for his interesting discussions and valuable advices. I also would like to thank Juan Tapia from University of Concepcion, Markus Mesimäki from Wärtsilä and Jussi Puranen for their useful discussions within FiDiPro project.

I am grateful to the honoured pre-examiners of the thesis, D.Sc. Yacine Amara from University of Le Havre and Professor Sergey Shirinskii from National Research University “Moscow Power Engineering Institute”, for their valuable comments to improve the manuscript.

I also wish to thank Jouni Ryhänen, Juha Karppinen and AXCO motors for building the prototype. Special thanks go to Markku Niemelä, Martti Lindh and Kyösti Tikkanen for the technical implementation of the test setup.

I am also in gratitude to PhD Julia Vauterin for her support in the educational process and PhD Hanna Niemelä for the proofreading of the thesis and the improvement of the English language.

I would like to express a word of attitude to Professor Vasiliy Titkov, Professor Elena Lomonova, Professor Rogel Wallace and Peter Jones for their interesting courses.

I would like to thank all my friends in Finland, India, Kazakhstan, Russia and Switzerland who have helped me to make my life whole and supported me in different ways throughout my study.

I would like to express my deepest gratitude to my mother Orynsha and to my brother Takhai, his wife Aliya and their son Tair whose love and support made all this possible.

Last but not least, I express my deepest gratitude to my dearest Yulia for her love and support during these years.

Katteden Kamiev
September 2013
Lappeenranta, Finland

Dedicated

to the memory of my father Kuanysh Kamiev

Contents

Abstract

Acknowledgements

Contents

Nomenclature	11
1 Introduction	15
1.1 Constraints.....	17
1.2 Generators in island operation.....	20
1.3 Overview of HESMs	26
1.3.1 Classification.....	26
1.3.2 Operation principle	34
1.3.3 Special features	34
1.3.4 Applications	35
1.4 Outline of the thesis.....	35
1.5 Scientific contributions and publications	36
2 Feasibility of an ARC-PMSG in island operation	39
2.1 Design considerations.....	39
2.1.1 Salient or non-salient pole construction.....	39
2.1.2 Radial or axial flux construction.....	40
2.2 SGs with different excitations	40
2.2.1 Conventional EESG	41
2.2.2 Proposed topologies	41
2.3 Finite element analysis	46
2.3.1 No-load test.....	46
2.3.2 On-load test.....	52
2.3.3 Short-circuit test.....	55
2.4 Excitation systems of the generators	56
2.5 Comparison of SGs	59
2.6 Economic aspects	61
2.7 Summary	63
3 Design procedure of an ARC-PMSG with ACL	65
3.1 Electromagnetic design	65
3.1.1 Electrically-excited pole	67
3.1.2 Damper winding.....	69
3.1.3 PM pole.....	71
3.1.4 Magnetic circuit	72
3.1.5 Mechanical consideration	73
3.1.6 Synchronous inductances.....	74
3.1.7 No-load characteristic	76
3.1.8 Phasor diagram.....	77

3.1.9	Compensating winding	78
3.1.10	Machine parameters	78
3.2	Thermal analysis.....	80
3.3	Summary	84
4	Test machine	87
4.1	Design requirements.....	87
4.2	Main dimensions	87
4.3	Finite element analysis	88
4.4	Experimental prototype	95
4.5	Summary	96
5	Experimental results	97
5.1	Stator winding measurements	99
5.2	No-load test	101
5.3	Sudden three-phase short-circuit test	105
5.4	On-load test in island operation.....	109
5.4.1	Quadrature-axis inductance.....	110
5.4.2	External and regulating characteristics	111
5.4.3	Losses and efficiency	112
5.5	Locked rotor test.....	113
5.5.1	Damper winding parameters	116
5.5.2	Compensating winding parameters	117
5.6	Network operation	118
5.7	Thermal analysis.....	120
5.8	Summary	122
6	Conclusions	123
6.1	Suggestions for future work	124
	References	127
	Appendix A	135
A.1	Base values.....	135
	Appendix B	136
B.1	Definitions of the thermal resistances	136
B.2	Definitions of the node numbers	137
	Appendix C	138
C.1	Stator winding concept of the test machine	138
C.2	Properties of Ne795a grade data by Neorem Magnets.....	138
C.3	Electrical schematics of the short circuits.....	139
	Appendix D	140
D.1	Electrical schematic of the no-load tests.....	140
D.2	Electrical schematic of the on-load tests.....	140

Nomenclature

Roman letters

A	linear current density	A/m
a	number of parallel branches	-
B	flux density	Vs/m ²
b	width	m
D	diameter	m
E	electromotive force	V
F	force	N
f	frequency	Hz
H	magnetic field strength	A/m
h	height	m
i_f	excitation/field/compensating current	A
I	current	A
k	coefficient	-
k_C	Carter coefficient	-
k_{w1}	winding factor for the fundamental harmonic	-
L	inductance	H
l	length	m
m	mass	kg
m	number of phases	-
N_{ph}	number of turns	-
n	rotational speed	min ⁻¹
P	power	W
p	number of pole pairs	-
Q	heat flow	W
Q	slot number	-
q	number of slots per pole and phase	-
R	resistance	Ohm
r	radius	m
S	area	m ²
S	apparent power	VA
T	torque	Nm
t	temperature	°C
t	time	s
U	voltage	V
v	velocity	m/s
X	reactance	Ohm
x	x-coordinate (width)	m
Z	impedance	Ohm
z_Q	number of conductors in a slot	-

U underlined symbols are RMS phasors

Greek alphabet

α	coefficient	-
α	convection coefficient	W/(m ² K)
δ	air gap	m
δ	load angle	°
η	efficiency	%
Θ	current linkage	A
λ	thermal conductivity	W/(mK)
μ	permeability	H/m
ν	harmonic order	-
ρ	electrical resistivity	Ohm·m
σ	electrical conductivity	S
σ	leakage	
τ	time constant	s
τ	pitch factor	m
Φ	magnetic flux	Vs
φ	phase angle	°
Ψ	flux linkage	Vs
Ω	(capital omega)	
ω	angular velocity	rad/s

Superscripts

'	equivalent
'	transient
"	subtransient

Subscripts

0	initial value
a	air gap
Amb	ambient
av	average
b	bolt
C	Carter factor
c	centrifugal
d	direct-axis
D	damper winding direct-axis
e	electromagnetic
eff	effective
f	field/excitation/compensating winding
Fe	iron losses
ind	inductive load

m	magnetizing, air gap
max	maximum value
mc	measuring coil
md	direct-axis magnetizing
mq	quadrature-axis magnetizing
n	nominal value
p	pole, Potier
ph	phase
PM	permanent magnet
Q	damper winding, quadrature axis
q	quadrature-axis
r	rotor, remanence
s	stator phase, synchronous
sat	saturated
sc	short-circuit, search coil
t	tooth
tot	total value
U	phase U
V	phase V
W	phase W
w1	fundamental harmonic
δ	air gap
σ	leakage

Abbreviations

2D	two-dimensional
3D	three-dimensional
AC	alternating current
ARC	armature-reaction-compensated
ACL	alternated current linkages
DC	direct current
DESM	double excited synchronous machine
DOL	direct-on-line
CPPM	consequent pole permanent magnet
CRHE	combinational rotor hybrid excitation
EE	electrically excited
EESG	electrically excited synchronous generator
EMF	electromotive force
FEA	finite element analysis
FEM	finite element method
G	grid, generator
HEFS	hybrid excitation flux-switching
HESG	hybrid excitation synchronous generator
HESM	hybrid excitation synchronous machine

IPM	interior permanent magnet
L	load
mmf	magnetomotive force
NdFeB	neodymium-iron-boron
PM	permanent magnet
PMSG	permanent magnet synchronous generator
PMSM	permanent magnet synchronous machine
p.u.	per unit
RMS	root mean square
SCL	series current linkages
SG	synchronous generator
SM	synchronous machine
SPM	surface permanent magnet
TE	totally enclosed

1 Introduction

Permanent magnet (PM) technology offers superior efficiency, and therefore, PM generators have become an attractive alternative to conventional electrically excited synchronous generators (EESGs) in applications where controlled voltage or reactive power is not needed. In addition, the availability and acceptable cost of high-energy PM materials encourage applying PM technology in ships. Further, the doctoral thesis studies opportunities to apply PM excitation in ship generators to produce constant frequency and voltage.

A conventional EESG comprises an armature winding in the stator and an excitation or field winding in the rotor, as shown in Fig. 1.1. The rotor is turned by a prime mover, in ships by diesel or gas engines, and the DC current is supplied to the excitation winding through brushes or a brushless exciter.

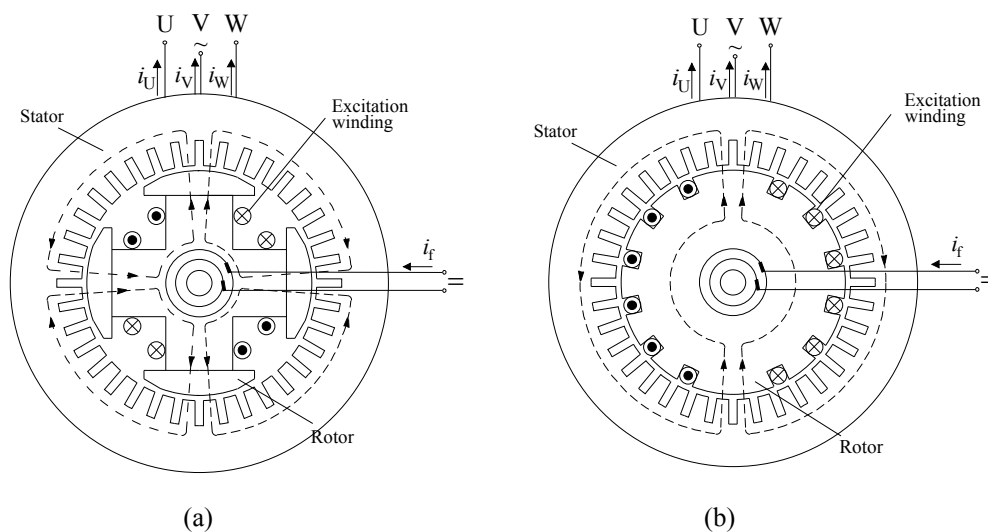


Fig. 1.1: Conventional electrically excited synchronous generators (EESGs).

(a) Four-pole salient pole topology.

(b) Two-pole non-salient pole topology.

Conventional synchronous generators (SGs) in marine and other island applications have proven to be technologies that provide good voltage regulation by deploying the field windings, high sustainable or steady-state short-circuit currents and the high-power capabilities of the machine. However, such machines have certain disadvantages. To generate the necessary flux levels, SGs must have heavy field windings, which cause mechanical problems in the rotor and also produce significant losses thereby contributing to the larger size of the machine. The rotor field winding losses dissipate into heat, and thus, proper cooling systems are needed. Moreover, the efficiency of the

generator decreases. Indeed, these and other factors make traditional SGs complex, large-size and massive.

Because of their high energy efficiency, PM generators are of great interest at present. A permanent magnet synchronous generator (PMSG) also consists of an armature winding in the stator and an excitation system in the rotor with the exception that the rotor field winding is replaced by PMs, see Fig. 1.2. The efficiency of a low-power (some hundreds of kW) PMSG may be several per cent units higher than that of similar power traditional EESGs, because the rotor of a PM generator does not need permanent energy supply for excitation. Such an increase in the overall efficiency of a generator set is very significant as a similar improvement in the overall efficiency is very difficult to achieve by any other means.

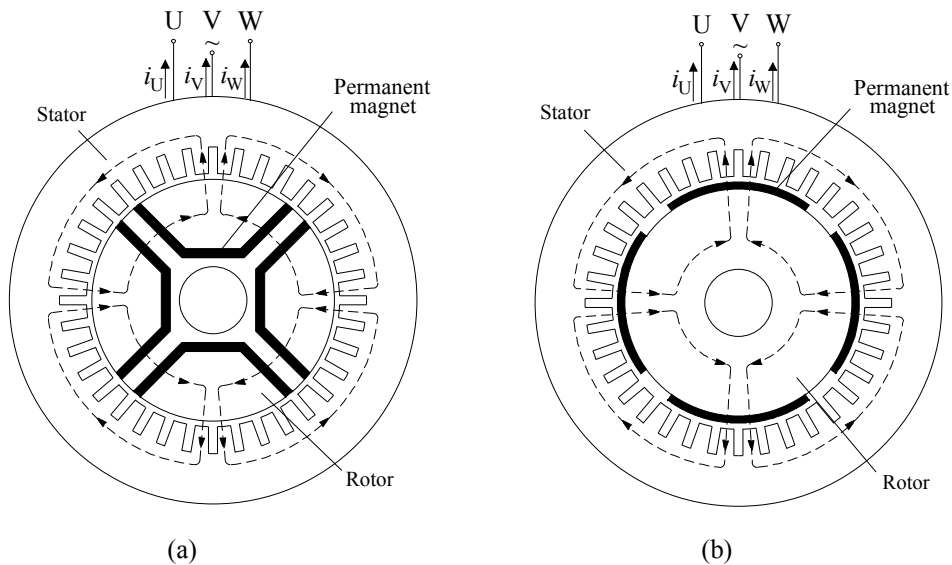


Fig. 1.2: Permanent magnet synchronous generators (PMSGs).
 (a) Embedded magnet machine with U-shaped magnets.
 (b) Rotor surface permanent magnet machine.

Since PMs are part of the magnetic circuit of the machine, they have a considerable effect on the total reluctance of the magnetic circuit. The relative permeability of modern PM materials, for example NdFeB, is about 1.04–1.05, and hence, the equivalent air gap length is significant. Consequently, in permanent magnet synchronous machines (PMSMs), the synchronous inductance L_d is low. Using PMs also results in a higher overall efficiency because of low excitation losses. A further advantage of a PM machine is that it has fewer components, and its simpler configuration makes it cost effective at least in principle.

A PM generator has also some disadvantages. The voltage regulation is problematic in machines of this kind because they do not have a field excitation control. This can be corrected by using an external voltage control such as large capacitor banks or power electronics, or by choosing the number turns of the stator winding properly to produce the required rated voltage. The generator internal voltage E_{PM} is also affected by temperature. The PM remanent flux density gets lower as the temperature increases. These properties make the use of PM generators in direct-on-line (DOL) applications challenging.

A comparison between conventional EESGs and PMSGs is presented in Table 1.1.

Table 1.1: Comparison between conventional EESGs and PMSGs.

Generator type	Advantages	Disadvantages
EESG	Easy voltage or reactive power regulation High power capabilities Proven, robust design	Low efficiency in the low power range up to a few MW Large support system
PMSG	Simple configuration High efficiency Smaller size and weight No excitation supply or field windings required Low synchronous inductance L_d	No excitation control Risk of PM demagnetization High material costs

1.1 Constraints

The requirements for synchronous machine (SM) performance are defined by national and international standards and classification societies. They set the limits for the variation of voltage and current quality in steady-state operation as well as in transients and, especially, in fault conditions.

Large current pulses may occur if there is a phase, frequency or amplitude difference between the grid voltage and generator EMF when connecting to the grid. Because the grid is weak in island operation, large current pulses cause large voltage sags. Usually, synchronization takes place at speeds close to the nominal one, at a correct phase sequence and a correct voltage phase. For instance, according to (Standard EN 50160, 2004), the voltage amplitudes may differ by $\pm 10\%$.

Some classification societies, for example (Lloyd's Register, 2011), require an SG to produce a sufficient sustainable short-circuit current during a symmetrical three-phase short-circuit fault. The requirement comes from the network safety devices, for example, old-fashioned protection relays, which require the sustainable short-circuit

current to be at least three times the rated current.

In island operation, a power factor is determined by the load power factor. The load of an SG can be resistive-capacitive, resistive-inductive or purely resistive. Typically, SGs produce the inductive current for the inductive load, such as induction motors, solenoids and relays. As it is known, in the case of an active-inductive load, the armature reaction is demagnetizing. An SG must be capable of compensating the demagnetizing armature reaction by a field winding current control.

Natural oscillations are inherent in an SM, since it constitutes an oscillating system when connected to a grid or other SMs. Such oscillations occur at any sudden unbalances or if there are changes in the load conditions of the SM (e.g. load surge or load shedding, a decrease in the input voltage, a change in the excitation current). In the case of an SM, during oscillations, the rotor of the machine rotates irregularly, that is, with some positive and negative slip around the synchronous speed, and its speed oscillates at some frequency at about an average value, which indicates that there are rotor oscillations. Rotor oscillations affect the synchronous operation of the machine, and may cause a high level of noise.

An effective means to damp the rotor oscillations is to apply a damper winding producing a high damper torque. The mechanical analogue of an SM connected to the grid or another parallel SG is shown in Fig. 1.3, where the spring emulates the link between the grid and the SM. Because of disturbances (a change in L), there will be oscillations (of the load angle δ) in the system, which are dampened by the amortisseur (shock absorber) as a result of the damper torques. Therefore, in order to provide smooth and stable characteristics and to operate in parallel with other similar generators, an SG must have an efficient damper winding.

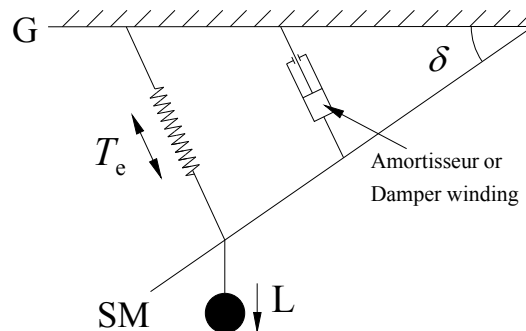


Fig. 1.3: Mechanical analogue of an SM connected to the grid or another parallel SG. Notations: G is the grid or another parallel SG, L is the load of machine, T_e is the electromagnetic torque and δ is the load angle.

For PMSMs, a damper winding plays an important role by protecting the PMs from demagnetization in asynchronous operation and in possible fault conditions by not letting the armature fields to penetrate the rotor. The most dangerous event for the PMs is a short circuit. In the case of a short circuit there is a risk of irreversible PM demagnetization resulting from the strong opposing armature reaction at the beginning of the short circuit when the peak of the stator current is high enough. Figure 1.4 illustrates the armature reaction (a) at the beginning of a sudden short circuit and (b) after the attenuation of the damper winding currents or without a damper winding at a sustainable short circuit. It can be said that the flux lines of the armature reaction at the beginning of the short circuit are expelled because of the damper winding currents, and the total flux goes around the PMs thereby preventing irreversible PM demagnetization.

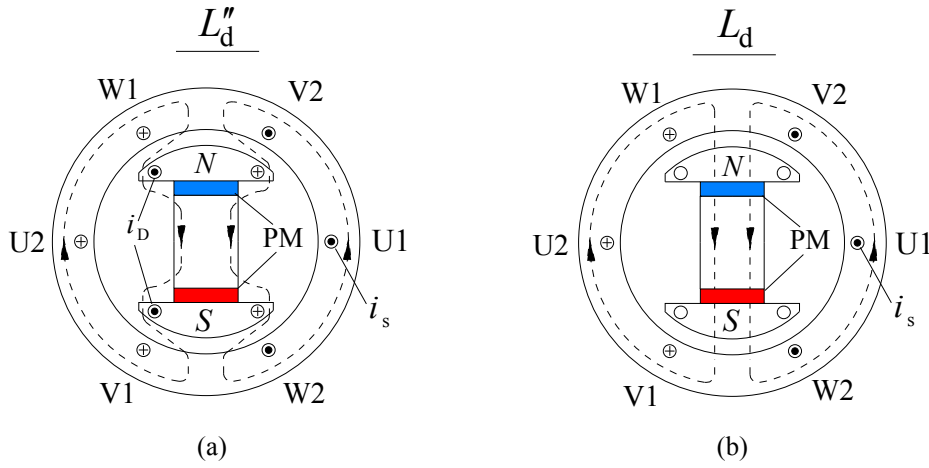


Fig. 1.4: Armature reaction during a PMSG short circuit.

(a) At the beginning of the short circuit.

(b) Sustained short circuit, i.e., after the attenuation of the damper winding currents.

Notations: i_D is the damper winding current, i_s is the stator current, L_d'' is the d-axis subtransient synchronous inductance and L_d is the d-axis synchronous inductance.

All the above-mentioned requirements define the main constraints for an SG operating in an AC island, see Table 1.2. These constraints must be taken into account in the design of an SG.

Table 1.2: Main constraints for an SG in AC island operation.

Parameter	Condition
Terminal voltage range in normal operation	$(0.9 \div 1.1)U_{ph}$
Sustainable short-circuit current, I_{sc}	$3I_n$
Power factor capability at rated load, $\cos \varphi$	0.8_{ind}
Damper winding	Obligatory

1.2 Generators in island operation

The main weakness of PMSGs in island operation is that the internal voltage E_{PM} of the generator cannot be controlled similarly as in EESGs and is affected by temperature. This is mainly the reason why small PMSGs equipped with a damper winding are normally used only in rigid networks, which maintain the voltage irrespective of the behaviour of the PMSG. Such PM machines are lightweight and economically competitive. If the reactive power of such a PMSG must be kept at a certain level, the size of the generator has often to be increased.

In island operation, especially in ships, an SG has to meet all the above-mentioned constraints. One of the most challenging requirements is the 300 % sustained short-circuit current. According to the equation

$$I_{sc} = \frac{E_f}{L_d} \text{ (p.u.)}, \quad (1.1)$$

the p.u. short circuit current I_{sc} depends on the p.u. induced voltage E_f and the p.u. direct-axis synchronous inductance L_d . The synchronous inductance is the sum of the magnetizing inductance L_m and the stator leakage inductance L_{sc} . In these types of machines, the synchronous inductance consists mainly of the magnetizing inductance L_m , the value of which depends on the machine dimensions and windings and can be written as in (Pyrhönen et al., 2008)

$$L_m = \mu_0 \frac{m}{\pi^2} \frac{2}{p} \frac{\tau_p}{\delta_{eff}} l' (k_{w1} N_s)^2. \quad (1.2)$$

Here, μ_0 is the permeability of vacuum, m is the number of phases, δ_{eff} is the effective air gap, τ_p is the pole pitch, p is the pole pair number, l' is the effective length of the machine and $k_{w1} N_s$ is the effective number of turns in series per stator winding. Similarly as the magnetizing inductance is dominating in the synchronous inductance, the air gap voltage of the machine E_m is also producing the main proportion of the terminal voltage U_s . According to Faraday's law, the air gap voltage can be calculated as

$$E_m = \frac{1}{\sqrt{2}} \omega k_{w1} N_s \hat{\Phi}_m, \quad (1.3)$$

where ω is the electric angular frequency. The amplitude of the air gap flux of the machine $\hat{\Phi}_m$ is

$$\hat{\Phi}_m = \int_0^{l'} \int_0^{\tau_p} (\hat{B}_\delta) dx dy, \quad (1.4)$$

where \hat{B}_δ is the amplitude of the air gap flux density. The required number of turns can be written as

$$N_s = \frac{E_m \sqrt{2}}{\omega k_{w1} \hat{\Phi}_m} = \frac{E_m \sqrt{2}}{\omega k_{w1} \alpha_i \hat{B}_\delta \tau_p l'}, \quad (1.5)$$

where α_i is the factor of the arithmetical per unit average of the air gap flux density (Pyrhönen et al., 2008). Inserting this in Eq. (1.2) gives

$$L_m = \mu_0 \frac{m}{\pi^2} \frac{2}{p} \frac{1}{\delta_{\text{eff}} \tau_p l'} \left(\frac{E_m \sqrt{2}}{\omega \alpha_i \hat{B}_\delta} \right)^2. \quad (1.6)$$

The pole pitch of the machine is

$$\tau_p = \frac{\pi D_\delta}{2p}, \quad (1.7)$$

where D_δ is the air gap diameter. Eq. (1.6) is rewritten with Eq. (1.7) into

$$L_m = \mu_0 \frac{m}{\pi^2} \frac{4}{\delta_{\text{eff}} \pi D_\delta l'} \left(\frac{E_m \sqrt{2}}{\omega \alpha_i \hat{B}_\delta} \right)^2. \quad (1.8)$$

As it can be seen in Eq. (1.8), the magnetizing inductance with a constant voltage and phase number is minimized by selecting a large effective air gap δ_{eff} , a large diameter D_δ or a large effective length l' for the machine. Maximizing the air gap flux density also has a clear effect but the air gap flux density usually remains in quite tight limits. As an example, increasing the air gap flux density from 0.8 T to 1 T reduces the magnetizing inductance by 36 % as the number of winding turns is simultaneously reduced by 20 %.

If the sustainable short-circuit current is three times the rated current and the induced voltage is $E_f = 1.1$ p.u., the maximum allowable p.u. d-axis synchronous inductance L_d is

$$L_{d\text{max}} = \frac{E_f}{I_{\text{sc}}} = \frac{1.1}{3} = 0.37 \text{ (p.u.)}. \quad (1.9)$$

To consider an SG in island operation that meets all the desired requirements, let us next investigate the phasor diagram of an SG. Figure 1.5 presents a phasor diagram of an SG, where the voltage U_s and current I_s are set to 1 p.u. to achieve the apparent power $S = 1$ p.u. The stator resistance is neglected. It should be kept in mind that the

following analysis is made by applying per unit values, which are obtained by dividing each dimension by a base value given in Appendix A.

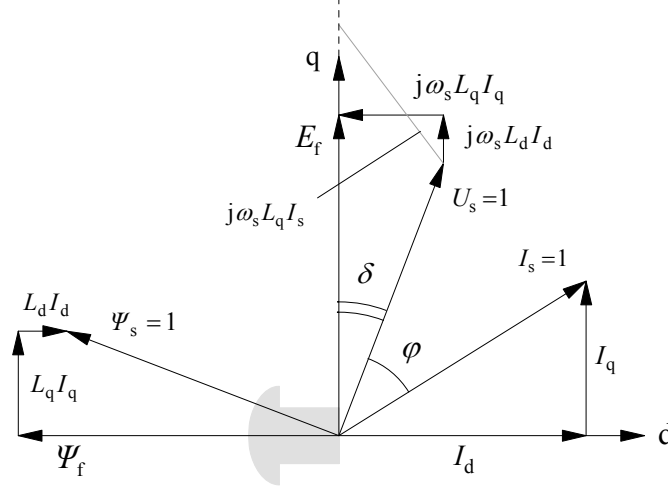


Fig. 1.5: Phasor diagram of an SG.

To achieve the rated apparent power $S = 1$ p.u., the voltage U_s and the current I_s are set to 1 p.u.

According to the phasor diagram, it is possible to write the following equations

$$U_s \cos \delta + \omega_s L_d I_d = E_f, \quad (1.10)$$

$$U_s \sin \delta = \omega_s L_q I_q, \quad (1.11)$$

where the stator current components I_d and I_q can be expressed by the load angle δ and the power factor angle φ as

$$I_d = I_s \sin(\delta + \varphi), \quad (1.12)$$

$$I_q = I_s \cos(\delta + \varphi). \quad (1.13)$$

By inserting Eqs. (1.12) and (1.13) into Eqs. (1.10) and (1.11), respectively, it is possible to define the synchronous inductances L_d , L_q as functions of the load angle δ

$$L_d = \frac{E_f - U_s \cos \delta}{\omega_s I_s \sin(\delta + \varphi)}, \quad (1.14)$$

$$L_q = \frac{U_s \sin \delta}{\omega_s I_s \cos(\delta + \varphi)}. \quad (1.15)$$

As it can be seen in Eqs. (1.14) and (1.15), only the d-axis synchronous inductance L_d depends on the induced voltage E_f . Figure 1.6 illustrates the behaviour of the synchronous inductances L_d and L_q as functions of the load angle δ at the unity power factor and $\cos \varphi = 0.8_{\text{ind}}$ and their ratios L_q/L_d as a function of the load angle δ when $\cos \varphi = 0.8_{\text{ind}}$ and $E_f = 1.1$ p.u. The d-axis synchronous inductance L_d in Fig. 1.6a and Fig. 1.6b is presented at three different induced voltages $E_f = 1.1$ p.u., $E_f = 1.3$ p.u. and $E_f = 1.5$ p.u. as a function of the load angle δ .

As it can be seen in Fig. 1.6, it can be noticed that

- the black line that corresponds to $L_q = f(\delta)$ divides the areas in the figure, see Fig. 1.6a and Fig. 1.6b, into two parts: $L_q < L_d$ and $L_q > L_d$;
- the intersection of the black line with the coloured lines that represent $L_d = f(\delta)$ gives $L_d = L_q$, that is, an SG becomes a non-salient pole machine. Further, when $E_f = 1.1$ p.u. and $\cos \varphi = 0.8_{\text{ind}}$, see Fig. 1.6b, the synchronous inductance $L_s = L_d = L_q = 0.15$ p.u. and the load angle $\delta = 6.6^\circ$. At $E_f = 1.1$ p.u. and a unity power factor, see Fig. 1.6a, the synchronous inductance $L_s = L_d = L_q = 0.44$ p.u. is generally the minimum, and it is more than 0.37 p.u. Therefore, in principle, a pure PMSG that is designed with a unity power factor cannot meet the short-circuit requirement;
- when $L_d < L_q$ an SG can be only a pure PMSG. Moreover, to meet this condition, the direct-axis reaction field must go through the PMs to increase the magnetic reluctance;
- in the case when $L_d > L_q$, an SG can be either a traditional SG or an inverse salient PMSG (Moncada et al., 2009). By varying the induced voltage of a traditional EESG, it is possible to determine the corresponding values for the synchronous inductances L_d, L_q ;
- as far as the induced voltage E_f is increasing, the d-axis synchronous inductance L_d inevitably has to increase because at a resistive-inductive load the generator armature reaction is demagnetizing;
- within the set limits, $E_{\text{PM}} = 1.1$ p.u., $\cos \varphi = 0.8_{\text{ind}}$ and $L_{\text{dmax}} = 0.37$ p.u., the synchronous inductance ratio L_q/L_d is more than 10, see Fig. 1.6c, which is difficult to deliver in a PMSG. (Liaw et al., 2005) considered a PMSG where $L_q/L_d = 7.5$ with $p = 2$. Probably $L_q/L_d < 7.5$ seems more realistic in a PMSG with $p \geq 2$;
- therefore, finding acceptable values of L_q is possible only when $L_d \leq 0.22$ p.u. The values determined for L_d are low even for a pure PMSM. As it was shown above, with a constant voltage and phase number, the d-axis synchronous inductance L_d , which mainly depends on the magnetizing inductance, can be minimized at the cost of a large effective air gap δ_{eff} , a large diameter D_δ , or a large effective length l' for the machine. Obviously, each of these parameters leads to the overdimensioning of a pure PMSG meeting the constraints. However, normal variation in the manufacturing and materials may result in a generator that does not meet the voltage condition despite the large machine size;

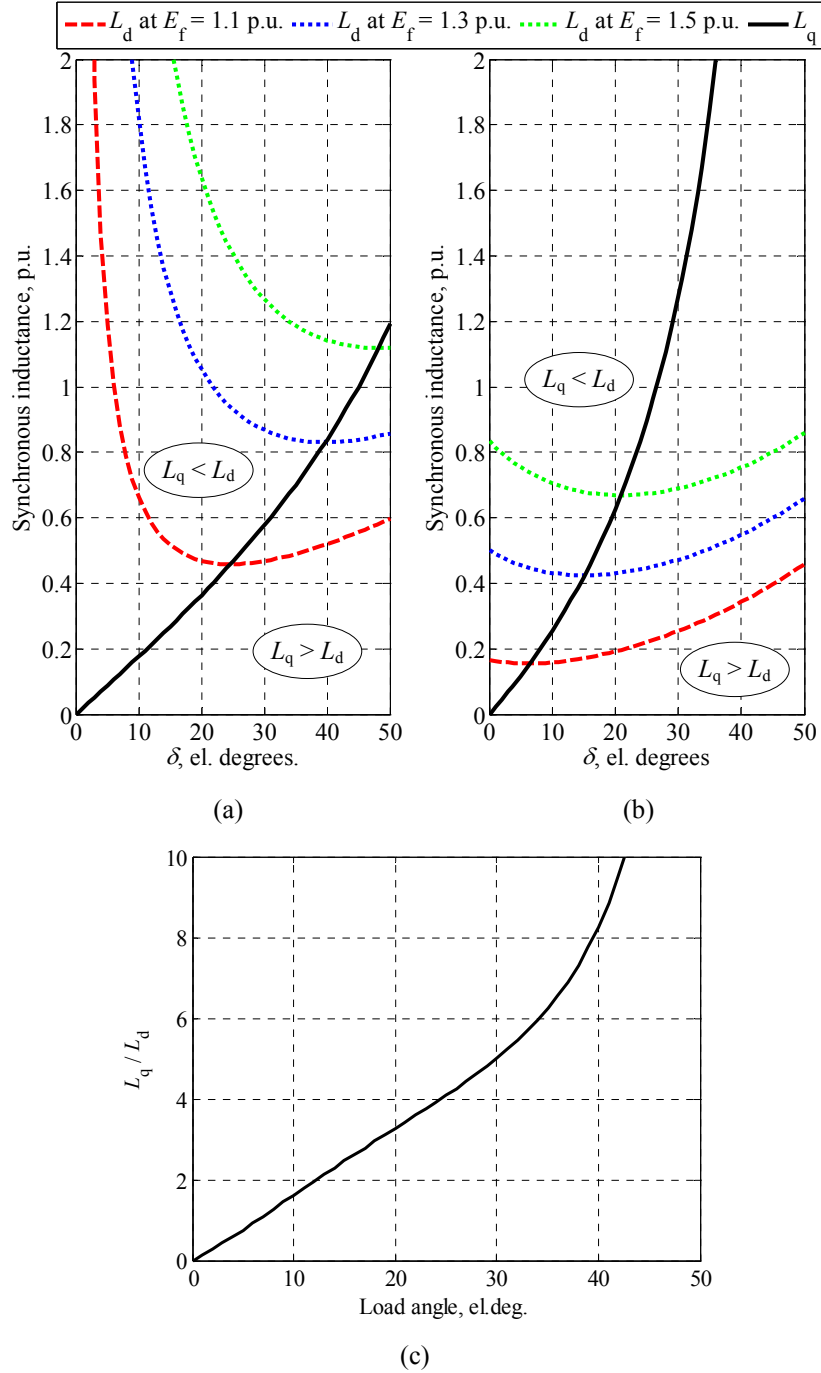


Fig. 1.6: Synchronous inductances and their ratios as functions of load angle.
 (a) Synchronous inductances L_q , L_d as functions of the load angle δ at a unity power factor.
 (b) Synchronous inductances L_q , L_d as functions of the load angle δ at $\cos \varphi = 0.8_{\text{ind}}$.
 (c) Ratio L_q/L_d as a function of the load angle δ when $\cos \varphi = 0.8_{\text{ind}}$ and $E_{PM} = 1.1$ p.u.

- although avoiding the short-circuit requirement, which is due to the old-fashioned relays, a pure PMSG is still economically inefficient when the power factor is $\cos \varphi = 0.8_{\text{ind}}$.

It may be concluded that a traditional PM generator (whether non-salient pole or salient pole) that meets all the requirements faces the following problems:

- to meet all the requirements, a very large machine should be built or
- there is a need to increase the PM generator no-load voltage exceeding the maximum allowed value $E_{\text{PM}} = 1.1$ p.u., and
- the d-axis synchronous inductance L_d must be made considerably smaller than $L_d = 0.6$ p.u., which should be sufficient to meet the 160 % torque demand.

Another important conclusion is that an SG with acceptable synchronous inductances can easily meet the desired requirements only if it can change the internally induced voltage, that is, it is able to change the excitation flux, which is possible by applying an electrical excitation.

Conventional EESGs easily meet the voltage or reactive power regulation and short-circuit requirements because the field winding current is controllable. During a short circuit, extra field winding current is supplied by two cascaded excitation generators having a large voltage reserve for the short-circuit excitation. In brushed machines, suitable current transformers can be used to supply extra current to the field winding during a short circuit. Such arrangements guarantee a compact main generator capable of meeting the constraints mentioned above. The only problem related to energy efficiency is that an SG tightly following the main boundary requirements easily becomes quite a low-efficiency machine. For example, a 500 kW, 400 V SM may have a rated point efficiency of only 94 % (Soldatenkova and Boronina, 1993) while the best PMSGs of the same power and speed can reach even 98 % because of low rotor losses and some machine overdimensioning.

If all the conditions are met, one problem still remains: the machine does not tolerate capacitive loads at low power because the voltage would increase above accepted values. However, capacitive loads are rare and can be present, in practice, only by accident for instance when a compensating capacitor bank control fails and the capacitors are connected to the grid at low inductive loads. Because the occurrence of such a problem is rare, it can be neglected at the design stage.

The above-mentioned problems can be avoided in island operation by an alternative technology that is assumed to apply a hybrid excitation generator. The hybrid excitation generator is built using PMs and traditional field windings combining the best features of the PMSG and the EESG.

A hybrid PM generator could solve the problem in quite a traditional way. Such a machine would act as a traditional EESG with the exception that the poles would also

be magnetized by PMs. The machine has both the benefits and disadvantages of a PM generator and a traditional SG. Therefore, the properties must be a compromise. A good compromise is searched in this doctoral thesis.

1.3 Overview of HESMs

Attempts to maintain the benefits and to mitigate the deficiencies of both the EESMs and the PMSMs have led to the invention of a hybrid excitation machine; an electrical machine with both the PM and field winding excitations included. In the literature, such machines are referred to with different names, the most common being ‘a hybrid excitation synchronous machine’ (Yiping and Haizhen, 2001; Hlioui et al., 2008; Patin et al., 2008; Li et al., 2009; Zhao, 2009; Shushu et al., 2010; Kosaka et al., 2010; Zhang et al., 2010; Han et al., 2011; Liu et al., 2011; Hoang et al., 2011), ‘a double excitation synchronous machine’ (Fodorean et al., 2007; Bali et al., 2010; Nedjar et al., 2011; Amara et al., 2011), ‘a combined excitation synchronous machine’ (But, 1990) or ‘a permanent-magnet assisted synchronous generator’ (Fukami and Shima, 2010; Hosoi et al., 2012; Yamazaki et al., 2012). Comprehensive reviews of such machines are provided for example in (Zhu and Chan, 2008; Al-Adsani and Schofield, 2009; Amara et al., 2009; Kamiev et al., 2010; Gieras, 2012). The term ‘hybrid excitation synchronous machine’ (HESM) seems to be the most frequent one used in the literature, and is therefore adopted in this thesis also.

HESMs are a relatively novel class of electrical machines. Such machines are mostly used as generators, where the total magnetic flux is produced by the simultaneous action of two different excitation sources: a PM excitation and a wound field excitation (an electrical excitation winding). The target behind using two excitation sources is to combine the advantages of PM-excited machines and wound field synchronous machines. The PMs produce the main excitation flux while the electrical excitation winding generates an additional excitation flux effectively improving the flux weakening or strengthening capability. Thanks to PMs, the electrical excitation losses are much lower than those of SMs with a traditional electrical excitation.

In this connection, it is worth remembering that in large SGs, multiple-pole excitation generators with one or two PM poles have been quite widely used in the industry. Such exciter machines are intended for generators in island operation to make the voltage build-up possible in machines operating outside a utility grid. However, such machines have totally different properties and are not regarded as HESMs in this thesis.

1.3.1 Classification

In the family of SMs, HESMs are found between separately magnetized SMs and PMSMs. A further classification of HESMs can be made depending on the factors considered in the following.

HESMs can be classified according to the magnetic flux paths through PMs and through field windings:

- a) series hybrid excitation and
- b) parallel hybrid excitation.

Examples of series and parallel HESMs with 2D radial flux paths are presented in Fig. 1.7. In the first group, the PMs and the excitation coils are connected in series: the flux produced by the excitation coils passes through the PMs. As a result of the magnetic properties of the PMs, there are some evident drawbacks related to the flux weakening capability:

- a powerful excitation winding is needed to produce a high current linkage to decrease the flux of modern NdFeB magnets with high remanent flux densities and high coercive forces, and
- there is a slight risk of PM demagnetization.

In the second group, the trajectory of the PM excitation flux differs from the flux produced by the excitation winding. Contrary to the series HESM, the parallel HESM have more flux weakening capability and allow a wide variety of structures.

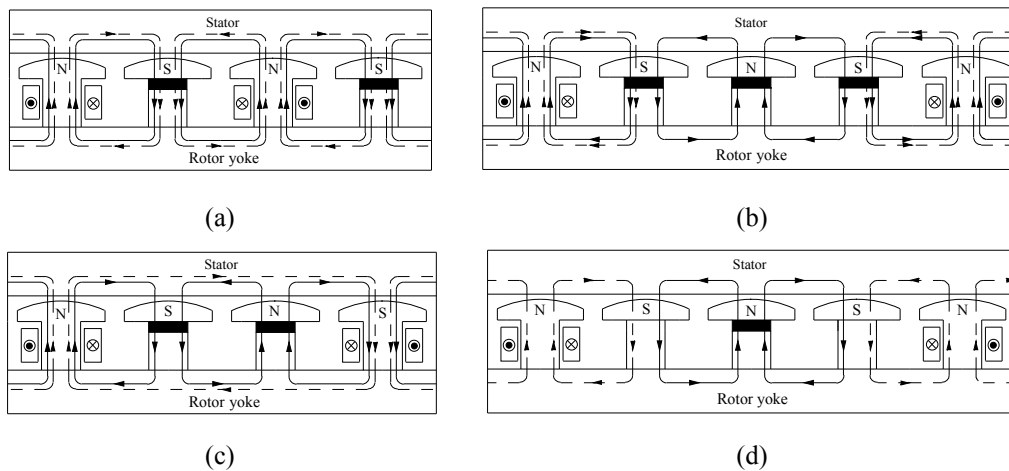


Fig. 1.7: Examples of series and parallel HESMs with 2D radial flux paths.

(a) and (b) Series hybrid excitation (in (b) partly parallel)

(c) and (d) Parallel hybrid excitation

The solid lines correspond to the magnetic flux paths resulting from the PM excitation, and the dotted lines indicate the electrical excitation.

According to the behaviour of the magnetic flux, HESMs can be radial, axial or combinations of these two.

There are various ways of implementing HESMs. The excitation winding (EW) can be placed either in the rotor similarly as the PMs, which introduces slip rings and brushes, or in the stator, which leads to different constructions. Classification of HESMs based on the design location of the excitation winding and PMs is shown in Fig. 1.8. Depending on the position of the excitation winding, the constructions can be with or without brushes.

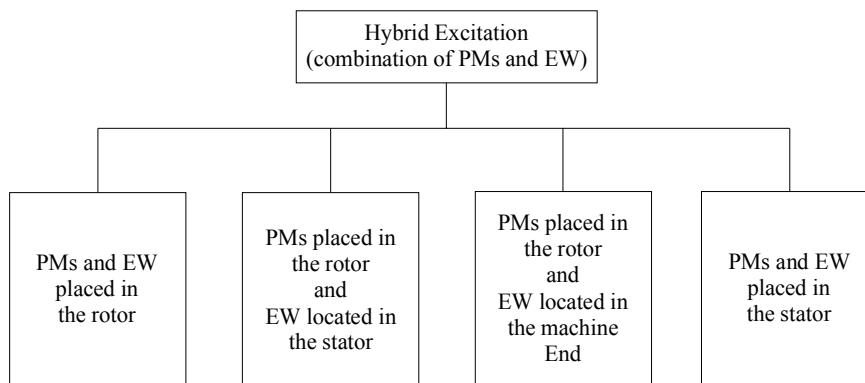


Fig. 1.8: Classification of HESMs based on the design location of the excitation winding (EW) and PMs.

HESMs have received a good recognition and become a hot topic for research. There are many different topologies presented in various technical papers and patent applications (Syverson and Curtiss, 1996; Schüller and Brandes, 1998; Geral and Manoj, 2002; Amara et al., 2004; Akemakou, 2006; Ganev et al., 2007; Babajanyan and Reutlinger, 2010; Reutlinger, 2010; Dooley, 2011; Gieras and Rozman, 2011). Examples of HESMs classified according to Fig. 1.8 are considered in the following.

Figure 1.9 provides some examples of HESMs where the PMs and excitation windings are placed in the rotor retaining a conventional stator. The stator carries a normal winding. These machines may have slip rings and brushes because the DC field winding is mounted on the rotor side. HESMs referred to this group are more similar to conventional SMs (either wound field SMs or PMSMs), and hence, they should be more robust, reliable and easy for manufacturing than machines in the other groups.

(Luo and Lipo, 1999) presented an electrical machine termed the SynPM machine, which is shown in Fig. 1.9a. The SynPM machine has four PM poles and two electrically excited poles. The SynPM machine works almost similarly as the PM machine with the exception that it has field regulation characteristics. By adjusting the excitation current, the SynPM machine varies not only by the air-gap flux, but also by the number of poles from six to two. The PM has two different flux paths, of which one passes the other PM bordered with it and the other passes through an electrically excited (EE) pole close to it. The flux of the electrical excitation is circulated between two

electrically excited poles because they have different polarities. This is possible only when the pole pair number p is odd. The SynPM machine becomes unsuitable in the cases when the pole pair number p must be even or this number must not change at different excitation currents (positive, zero or negative values). Fluxes caused by PMs and DC field windings are radial fluxes. Since the flux produced by the excitation coils does not pass through the PMs, according to the classification, the SynPM belongs to the parallel hybrid excitation group.

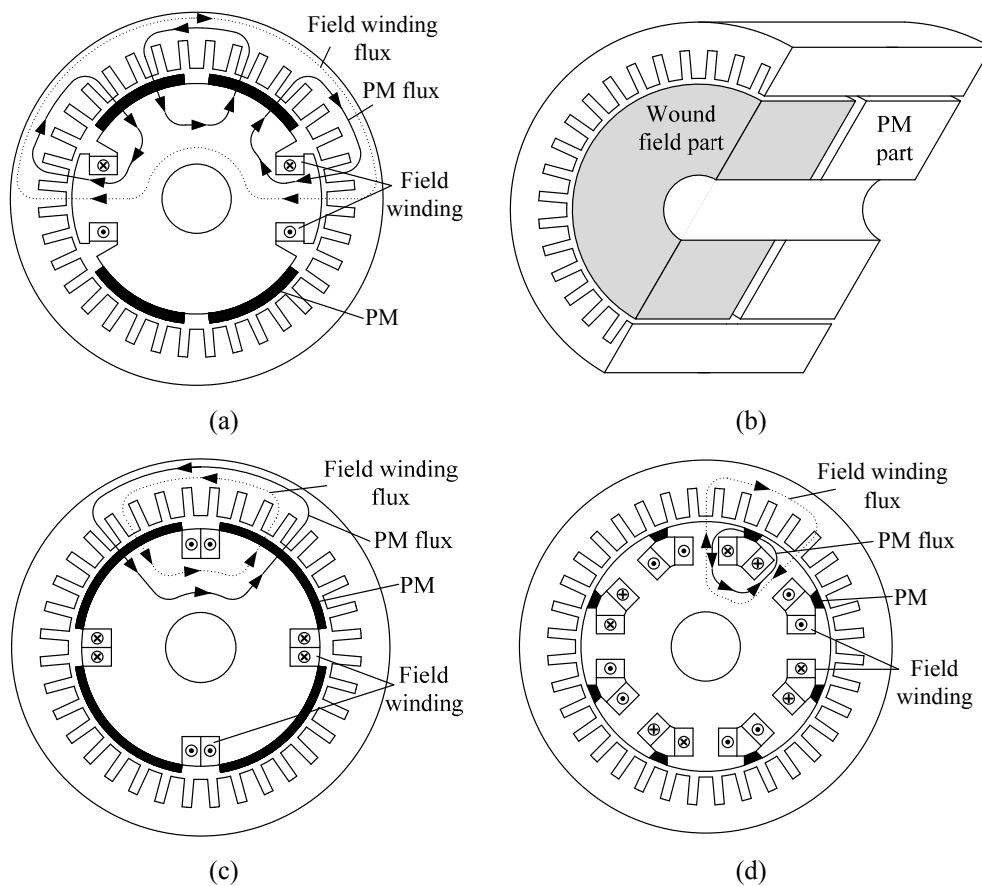


Fig. 1.9: Examples of HESMs where PMs and excitation windings are placed in the rotor.
 (a) SynPM machine.
 (b) Combined rotor hybrid excitation machine (CRHE).
 (c) Double excited synchronous machine (DESM).
 (d) Permanent-magnet-assisted salient-pole synchronous generator.

(Chalmers et al., 1997) have presented a structure with a combined rotor, where unlike in other SMs, the machine has two rotor parts; one is a PM part and the other is a reluctance part. Later in 2001, (Naoe and Fukami, 2001) presented a machine in which

the reluctance machine part is replaced by an electrically excited part, Fig. 1.9b. This construction is termed a combined rotor hybrid excitation machine (CRHE). PMs may be mounted on the rotor surface or embedded in the rotor. The magnetic paths of the two parts are independent of each other, and each path is radial. Thus, the machine belongs to the parallel hybrid excitation group. Some space is needed between the two rotors: first, to avoid PM leakage and second, to place the excitation end winding, which in turn increases the length of the machine.

The construction presented in Fig. 1.9c was studied in (Fodorean et al., 2007) and called in the paper as the double excited synchronous machine (DESM). In the DESM, PMs are mounted on the rotor surface and the excitation coils are placed in the rotor slots. The magnetization sources of the DESM are in series, in other words, the flux produced by the excitation coils passes through the PMs. The magnetic paths of both sources are radial.

The last example of this group is called the permanent-magnet-assisted salient-pole synchronous generator, Fig. 1.9d. In the PM-assisted salient-pole SG, the PMs are placed between adjacent pole shoes. In the rotor pole cores, the flux produced by the PM is generated in the direction opposite to the flux produced by the excitation winding. Thus, the magnetic saturation in the rotor pole cores is reduced, and a higher EMF can be induced in the stator armature winding. This construction suffers from certain deficiencies, which may raise problems in some cases. First, from the mechanical point of view, the installation of the PMs must be carefully considered because of the centrifugal forces. Second, from the thermal point of view, the generator must be equipped with a good cooling because the PMs are placed close to the excitation windings, which produce heat according to Joule's law. Finally, because of a sudden three-phase short circuit, which can take place either on the network or in island operation, there is a significant risk of irreversible demagnetization in the whole area of the PMs.

(Mizuno, 1997) patented a configuration where the PMs are placed in the rotor and the excitation winding is placed in the stator, as shown in Fig. 1.10. Later it was called a consequent pole PM machine (CPPM). A machine of this kind was studied also in Japan and the USA. The machine consists of a rotor divided into two sections. One section has partial rotor-surface-mounted PMs that are radially magnetized while the other has a laminated iron pole. The stator is composed of a laminated core, a solid iron yoke and a conventional AC three-phase winding located in the slots. A circumferential field winding is placed in the middle of the stator, which is excited by a DC current that is externally controlled to allow variable excitation.

An important component in the machine operation is the axial flux, which is provided by the solid stator and rotor parts, which constitute a low reluctance path. The radial flux caused by the PMs circulates from one PM to the next one through the air gap, teeth, the stator and the rotor yoke. The axial flux produced by the field winding passes from one iron pole to the next one across the air gap, teeth, the stator and the rotor yoke.

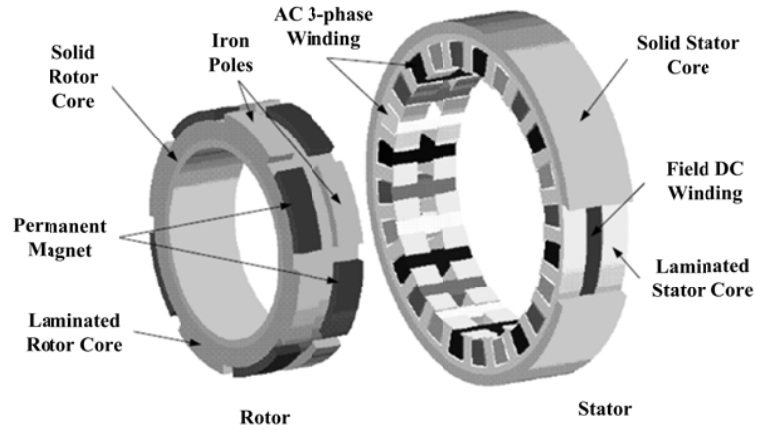


Fig. 1.10: Consequent pole PM machine (CPPM) (Tapia, 2002).

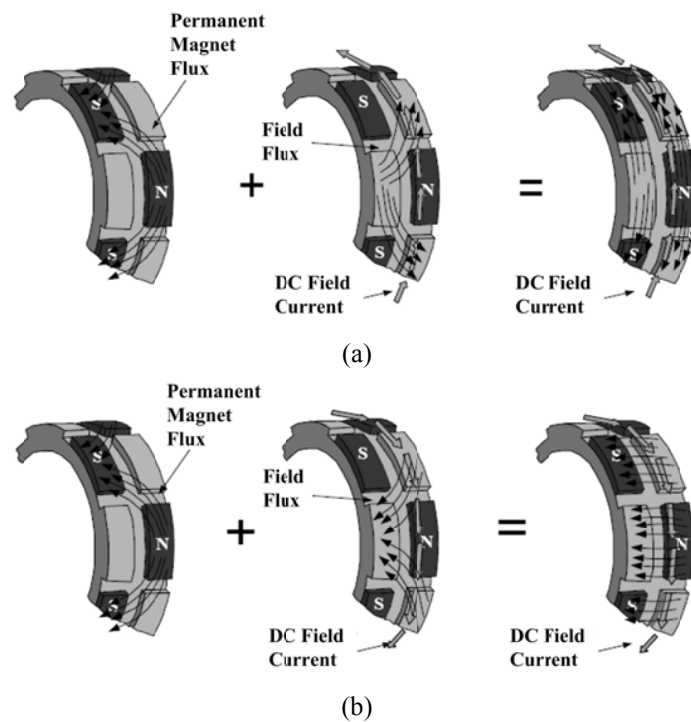


Fig. 1.11: Operation principle of the CPPM machine (Tapia, 2002).
 (a) strengthening effect
 (b) weakening effect

The radial and axial fluxes converge in the air gap, and depending on the polarity of the field current, a strengthening or weakening operation takes place as presented in Fig.

1.11. The magnetic paths of the two magnetization sources can be considered independent of each other, and hence, this construction represents the parallel hybrid excitation group.

Owing to the excitation winding placed in the stator, no brushes or slip rings are needed. The absence of the demagnetization risk for the PMs, which is due to the relatively independent magnetic paths of the two magnetization sources gives yet another advantage of the CPPM.

In contrast to the advantages, the CPPM has some drawbacks that are due to its special configuration. According to (Gieras, 2012) the space required for the field winding tends to increase the outer diameter. In addition, the field winding decreases the power density. Finally, there are also some manufacturing problems.

Figure 1.12 shows the hybrid excitation machine with a powdered iron core where the PMs are placed on the rotor surface and the excitation coils are mounted in the machine ends. The configuration was studied in (Kosaka and Matsui, 2008). The machine employs a consequent pole rotor and a conventional stator with a three-phase armature winding. Both the stator and rotor consist of two sections: the laminated and powdered iron cores. The laminated cores provide a two-dimensional flux path similarly as in a PMSM. The powdered iron cores ensure the three-dimensional flux paths.

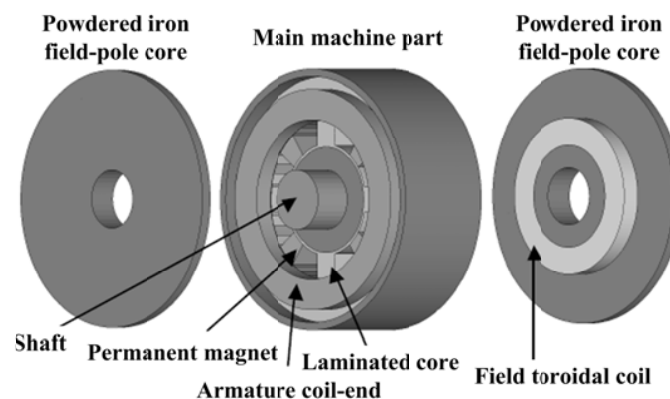


Fig. 1.12: Hybrid excitation machine with a powdered iron core (Kosaka and Matsui, 2008).

The field strengthening operation principle of the machine is illustrated in Fig. 1.13. The flux produced by the PMs is radial while the flux caused by the toroidal excitation coils is axial. The field weakening operation is achieved by changing the direction of the DC current. Since the flux generated by the toroidal field coil does not pass the PMs, this construction belongs to the parallel hybrid excitation group.

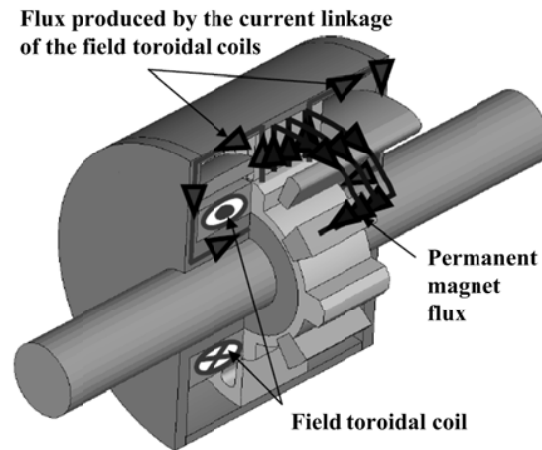


Fig. 1.13: Field strengthening operation principle of the hybrid excitation machine with a powdered iron core (Kosaka and Matsui, 2008).

The construction of the topologies where both the excitation systems are located in the stator is quite similar to the switched reluctance machines. One of the possible examples called a hybrid excitation flux-switching (HEFS) machine (Hua et al., 2009; Hoang et al., 2010; Sulaiman et al., 2011) is presented in Fig. 1.14. The stator carries a three-phase armature winding, the PMs and the excitation windings. The rotor of the HEFS machine is as simple as that of the switched reluctance machine.

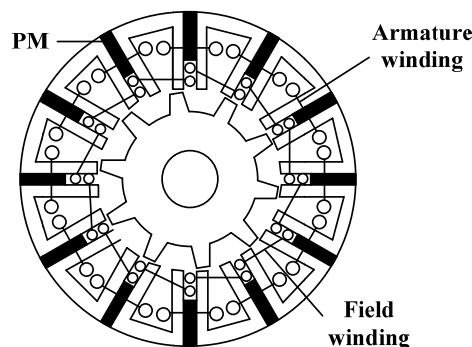


Fig. 1.14: Hybrid excitation flux-switching (HEFS) machine (Hua et al., 2009).

The operation principle is shown in Fig. 1.15. When the electrical excitation coincides with the PM excitation, the strengthening operation is achieved, see Fig. 1.15a, otherwise the machine is in the weakening operation, Fig. 1.15b. According to the classification of HESMs based on the fluxes of two different excitation sources, HEFS machines can be referred either to the series hybrid excitation group as in Fig. 1.14 or to the parallel one. The machines of the last group are termed as parallel hybrid excitation

flux-switching (PHEFS) machines. They can be produced by dividing the machine stator into two parts: the first part contains only PMs and the second one has only field coils. By controlling the polarity and amplitude of the excitation current, the strengthening/weakening operations can be achieved.

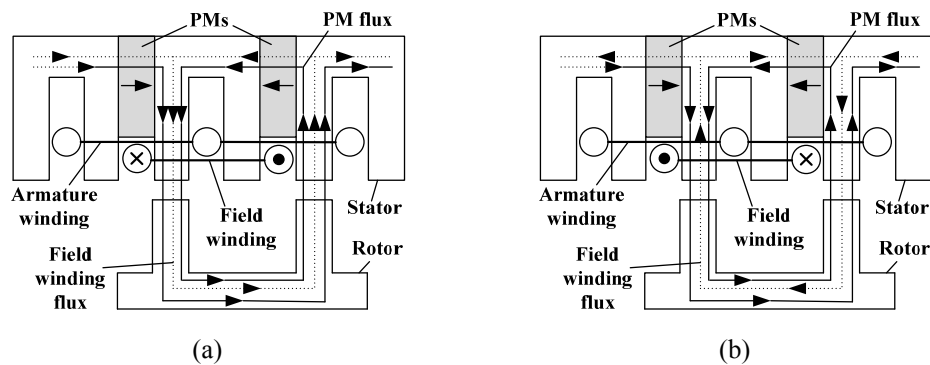


Fig. 1.15: Operation principle of the HEFS machine (Hua et al., 2009).

(a) Strengthening operation

(b) Weakening operation

When the electrical excitation coincides with the PM excitation, the strengthening operation is achieved, otherwise the machine is in the weakening operation.

The main advantage of HEFS machines is the absence of slip rings because the field winding is placed in the stator. The additional advantages such as sinusoidal EMF, good flux-regulation capability and passive rotor structure make HEFS machines attractive for example for traction applications. However, in higher power ratings, that is, above 500 kW the stator outer diameter of an HEFS machine tends to increase in order to carry the corresponding excitation current linkage, which is disadvantageous from the perspective of the machine size.

1.3.2 Operation principle

An HESM has two magnetization sources. One is the PM source that provides the magnetic circuit with a constant current linkage, and the other is the field winding (with the DC current) that acts as the current linkage source to mitigate the stator armature reaction. During the operation, depending on the direction of the armature reaction, the air gap flux can be enhanced or reduced by adjusting the magnitude and direction of the excitation current in the field winding.

1.3.3 Special features

The special features of the HESM make it different from other types of electrical machines:

- two magnetization sources, which can be connected either in series or in parallel;
- location of the PMs and the field windings;
- bidirectional DC current.

Different excitation sources and their physical locations in the machine set some limitations on using parallel paths in an armature integer slot winding. The machine in this case must be analysed by dividing it into similar sections. This can result in a significant reduction in options of using parallel winding paths. This constraint is the easiest one in the case of alternating excitation sources thereby making a two-pole system suitable for a base winding in a machine.

1.3.4 Applications

Owing to their special configurations, HESMs have certain merits that are inaccessible for PMSMs and traditional wound field SMs. Thus, theoretically, HESMs have potential to be used in various application fields. HESMs can be used both as motors and generators. As a generator, they can be used in island operation (e.g. island in a ship). As a motor, an HESM is attractive for traction applications because of its field weakening characteristic. As the price of an HESM is high for traction applications, it is most likely found in large power drives.

1.4 Outline of the thesis

The objective of this doctoral thesis is to find the best possible HESG solution for high-power island operation. Because the traditional solution, namely the conventional SG, suffers from a low efficiency, and the pure PMSG has to be seriously overdimensioned in island operation, the research focuses on an alternative technology that is assumed to apply a hybrid excitation synchronous generator (HESG) provided with damper windings. With this target in mind, the research can be considered to comprise two main phases.

The first phase is the feasibility study of an HESG in island operation. It includes a review of the HESMs, a proposal of suitable topologies for island operation and their comparison with the traditional solutions. The comparison includes technical and economic aspects. An HESG must meet all the requirements of an AC island:

- the generator terminal voltage must remain within $\pm 10\%$ in all cases in normal operation;
- the generator sustainable short-circuit current must be three times the rated current at least for two seconds;
- the generator must be capable of supplying inductive loads with $\cos \varphi = 0.8_{\text{ind}}$, and

- the generator must be equipped with an effective damper winding to enable parallel operation of several synchronous machines.

In the second phase, a design procedure of the proposed topology that shows the best performance in island operation is considered. The design procedure includes electromagnetic and thermal analyses verified by finite element analyses and experimental measurements. The electromagnetic design is based on analytical calculation.

This doctoral thesis consists of six chapters, the structure and contents of which are organized as follows:

Chapter 1 presents the main requirements in island operation. The problems faced by an SG in an AC island are considered. An HESG is proposed as an alternative solution. An overview of HESM topologies is given. The targets and contributions of the study are presented.

In **Chapter 2**, the feasibility of SGs with different excitations in island operation is discussed. The design aspects of an SG are considered. Based on the properties of different HESM topologies, three different HESGs are proposed. The technical and economic comparison of the proposed HESGs is made with the traditional EESG.

Chapter 3 presents a design procedure of a special type of HESGs. Based on its operation principle and special configuration, the proposed topology can be described as an armature-reaction-compensated permanent magnet synchronous generator with alternated current linkages (ARC-PMSG with ACL). The electromagnetic analysis based on the analytical calculation is presented. The thermal analysis of the proposed topology is studied.

Chapter 4 introduces the test machine, which was built to verify the operation principle and predicted results of the studied ARC-PMSG with ACL. The design requirements and main dimensions of the test machine are presented.

Chapter 5 presents the experimental results and their comparison with the results of the analytical and finite element analysis (FEA).

In **Chapter 6**, the scientific contributions of the doctoral dissertation are discussed and suggestions are given for the future work.

1.5 Scientific contributions and publications

The main scientific contributions of this thesis are the following:

- The thesis presents a general overview of the HESMs: classifications, operation principles and different topologies with their advantages and drawbacks.

- The thesis shows the feasibility of SGs with different excitations in island operation. The main constraints are presented. The two proposed special types of HESGs termed as ARC-PMSG with SCL and ARC-PMSG with ACL are compared with the traditional EESG and PMSG in island operation.
- The thesis provides an electromagnetic design based on the analytical calculation of the proposed ARC-PMSG with ACL.
- The thesis considers the thermal modeling and analysis of the studied ARC-PMSG with ACL.
- The thesis demonstrates the test machine, which was built to verify the operation principle and predicted results of an ARC-PMSG with ACL. The experimental results are compared with the results of the analytical and numerical calculations.

The results described in the thesis have been published in the following papers:

1. Kamiev K., Nerg J. and Pyrhönen J., “Design of damper windings for direct-on-line radial flux permanent magnet synchronous generators,” in *IEEE EUROCON conference (EUROCON 2009)*, Saint-Petersburg, Russia, pp. 783–790.
2. Kamiev, K., Nerg J., Pyrhönen J. and Zaboin V., “Hybrid excitation synchronous generators for island operation,” in *IEEE International Conference on Electrical Machines (ICEM 2010)*, Rome, Italy, pp. 1–6.
3. Kamiev K., Zaboin V. and Pyrhönen J., “Hybrid excitation synchronous generators for diesel gensets,” in *Marine conference in SMTU*, Saint-Petersburg, Russia, 2012.
4. Kamiev K., Nerg J., Pyrhönen J., Zaboin V. and Tapia J., “Feasibility of different excitation methods of synchronous generators in island operation,” in *IEEE International Conference on Electrical Machines (ICEM 2012)*, Marseille, France, pp. 2902–2908.
5. Kamiev K., Nerg J., Pyrhönen J., Zaboin V., Hrabovcová V. and Rafajdus P., “Hybrid excitation synchronous generators for island operation,” *IET Electric Power Applications*, vol. 6, no. 1, January 2012, pp. 1–11.
6. Kamiev K., Nerg J., Pyrhönen J., Zaboin V. and Tapia J., “Feasibility of an armature-reaction-compensated permanent magnet synchronous generator in island operation,” *IEEE Transactions on Industrial Electronics*, forthcoming.

7. Kamiev K., Pyrhönen J., Nerg J., Zaboyn V. and Tapia J., “Modelling and testing of an armature-reaction-compensated permanent magnet synchronous generator,” *IEEE Transactions on Energy Conversion*, forthcoming.

2 Feasibility of an ARC-PMSG in island operation

This chapter considers the feasibility of an ARC-PMSG in island operation based on a comparison with the traditional EESG. The comparison focuses on technical and economic aspects. The design considerations are discussed, and the proposed topologies of ARC-PMSGs are presented. The performance of SGs in island operation is studied by the two-dimensional (2D) FEA.

2.1 Design considerations

Table 2.1 presents the design requirements of a fictitious low-power SG for island operation. In general, an SG can be built as a salient or non-salient pole, and a radial or axial flux construction. To narrow down the design considerations, these criteria are discussed below.

Table 2.1: Design requirements of a fictitious 400 kW, low-voltage SG for island operation.

Parameter	Value	Unit
Phase number, m	3	-
Nominal power, P_n	400	kW
Nominal line-to-line voltage, U_n	450	V
Frequency, f	60	Hz
Rotational speed, n	900	rpm
No-load induced phase voltage, E_{ph}	$(0.9 \div 1.1)U_{ph}$	V
Sustainable short-circuit current, I_{sc}	$3I_n$	A
Power factor at rated load, $\cos \varphi$	0.8_{ind}	-

2.1.1 Salient or non-salient pole construction

The conventional non-salient pole EESGs are constructed with the pole pair numbers $p = 1$ and $p = 2$, and hence, they operate at relatively high rotational speeds (for example, at the 60 Hz frequency, the rotational speeds are 3600 rpm and 1800 rpm, respectively). The salient pole EESGs are usually produced with the pole pair number $p \geq 2$, and hence, the rotational speed is lower than 1800 or 1500 rpm at the 60 or 50 Hz frequency, respectively. Because of the required rotational speed (see Table 2.1), an EESG usually represents a salient pole construction.

In PMSMs, the PMs can be placed either on the surface of the rotor or buried in the rotor (interior PM rotor). In principle, a machine with rotor-surface-mounted PMs (SPM) refers to the non-salient pole SMs because the permeability of modern NdFeB PMs $\mu_r \approx 1.04\text{--}1.05$, which is close to the permeability of air. Further, the machine with

an interior PM (IPM) rotor belongs to salient pole machines. The comparison of the machines with the SPM and IPM rotors is given in Table 2.2 (Kamiev et al., 2012).

Table 2.2: Comparison of PMSMs with SPM and IPM rotors.

Rotor type	SPM rotor	IPM rotor
Demagnetizing field strength	high	low
Magnets mechanically	vulnerable	protected
Damper winding construction	difficult	easy
PM leakage flux	low	high

Based on Table 2.2 and the above statements, it is natural to prefer a salient pole PMSG to a non-salient pole one in island operation.

2.1.2 Radial or axial flux construction

The two main mechanical constructions of electrical machines are radial and axial flux machines. An axial flux machine is inherently short but has a large diameter. A radial flux machine may be constructed with different length-to-diameter ratios. The traditional design guideline for well-designed multiple-pole synchronous machines is $l/D \approx \pi/4/p^{0.5}$ (Pyrhönen et al., 2008). As a result, low-speed multiple-pole machines usually have a low length-to-diameter ratio (l/D) while high-speed machines have a high length-to-diameter ratio. The advantages of the radial flux machine versus the axial flux machine are:

- the rotor of a radial flux machine can be more robust compared with the rotor of an axial flux machine;
- ideally, there are no axial forces in a radial flux machine between the stator and the rotor like in axial flux machines;
- in some cases, the rotor of a radial flux machine can be built as hollow, and is thus easier to cool;
- a required damper winding is easier to arrange in a radial flux machine, and
- to produce a suitable inertia for the prime mover, the dimensions of the radial flux rotor can easily be adjusted.

Summarizing the above arguments, an SG for island operation can be favourably built with salient poles and a radial main flux.

2.2 SGs with different excitations

In the previous chapter, it was shown that a pure PMSG for island operation has to be heavily overdimensioned and will thus be economically inefficient. Therefore, a pure PMSG was not considered. Only the conventional EESG and the proposed topologies of HESGs were designed in the study. The SGs were designed based on (Sergeev, 1969).

2.2.1 Conventional EESG

The main geometry data of the conventional EESG that satisfies the design requirements given in Table 2.1 are presented in Table 2.3. The cross-sectional view of the conventional EESG is shown below together with other studied SGs, see Fig. 2.2a. The laminated stator of the SG is made of M600-50A. The iron poles of the laminated rotor, the material of which is Fe52, are attached to the solid rotor yoke, which is made of Fe52C.

Table 2.3: Main geometry data of the designed SGs for island operation.

Parameter	EESG	6-2 HESG	ARC-PMSG with SCL	ARC-PMSG with ACL
Air gap diameter, D_δ	730 mm	730 mm	730 mm	730 mm
Active length, l	512 mm	422 mm	476 mm	446 mm
Air gap length, δ	5 mm	5 mm	5 mm	5 mm
Number of stator slots, Q_s	48	48	48	48
Number of slots per phase and pole, q	2	2	2	2
Number of phase turns, N_{ph}	16	16	16	16
Number of field winding turns per pole, N_f	44	44	27	44
PM dimensions, $h_{PM} \times w_{PM}$	-	$22 \times 143,$ $22 \times 135,$ mm^2	$25 \times 203,$ mm^2	$25 \times 150,$ mm^2

2.2.2 Proposed topologies

As it was mentioned above, the HESMs can be classified according to the magnetic flux paths produced by the PMs and the field windings. Figure 2.1a presents the operating principle of a series HESM, where the flux generated by the field winding passes through the PMs. Further, Fig. 2.1b depicts a tentative operating principle of a parallel HESM, where the flux produced by the field winding does not pass the PMs.

In the previous chapter, it was shown that to meet the requirements in island operation, an HESG must change its rotor excitation flux in such a way that it effectively compensates the armature reaction. By comparing the series and parallel hybrid excitation groups, it is evident that the machines of the series hybrid excitation group suit better for applications where the d-axis demagnetizing armature reaction is high. They evenly compensate the armature reaction and have a lower d-axis inductance L_d because the d-axis armature reaction flux goes through the PM material. Moreover, it is much easier to keep the air gap flux density almost constant with a series HESM rather than with a parallel HESM.

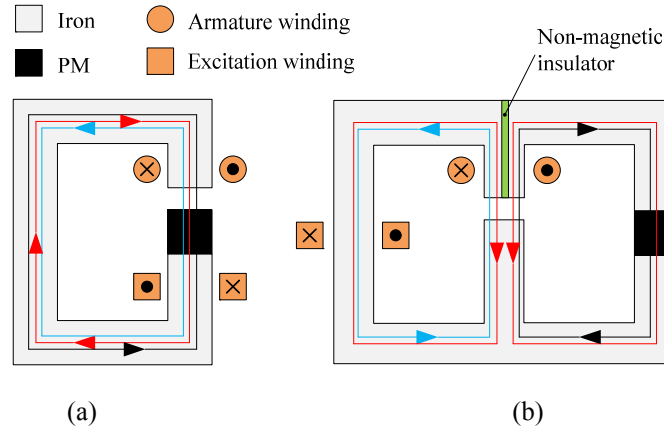


Fig. 2.1: Operation principles of series and parallel HESMs.

(a) Series HESM.

(b) Parallel HESM.

The red line represents the armature reaction, the black lines correspond to the PM flux and the blue lines refer to the flux generated by the excitation winding. In a parallel HESM, only a part of the armature reaction flux can be compensated, and therefore, this version has a somewhat limited capacity for the compensation compared with the series HESM.

Table 2.4 presents the comparison of different HESMs considered in the previous chapter. Considering the advantages and drawbacks of different HESMs, we may conclude that all the machines are not suitable for island operation. The variation in the pole number of the SynPM machine in a constant speed operation becomes a drawback, because the machine requires a frequency converter to keep the frequency constant. A CRHE applies a simple structure, but because of the rotor end windings it tends to be a long machine, which is a disadvantage in applications where the space is limited, especially in ships. A DESM applies the same operation principles that are needed in island operation. But since the PMs are placed on the surface of the rotor, the machine has a high PM demagnetization risk during a sudden short-circuit, which is of a common occurrence in island operation. A PM-assisted SG as the DESM cannot meet the short-circuit requirement because of the harmful eddy currents induced on the PM surfaces during a sudden three-phase short circuit. Despite a low PM demagnetization risk, a CPPM suffers from a low efficiency and manufacturing problems. Moreover, a CPPM machine belongs to the group of parallel HESM. A hybrid excitation machine with a powdered iron core would have some manufacturing problems, and since the topology is totally closed, it may require water cooling, which further complicates the system. A field winding of an HEFS, as in the case of a CPPM in the desired power rating, tends to increase the dimensions of the stator.

Table 2.4: Comparison of different HESMs.

Topology	Magnetization sources	Flux type	Advantage	Disadvantage
Syn/PM machine	Series/ Parallel	Radial	<ul style="list-style-type: none"> - number of poles varies from 6 to 2 - simple structure - easy fabrication - high torque density 	<ul style="list-style-type: none"> - possible presence of slip rings and brushes
Combined rotor hybrid excitation machine (CRHE)	Parallel	Radial	<ul style="list-style-type: none"> - simple structure - easy fabrication - high torque density 	<ul style="list-style-type: none"> - possible presence of slip rings and brushes - long axial length due to the rotor end windings
Double excited synchronous machine (DESM)	Series	Radial	<ul style="list-style-type: none"> - simple structure - easy fabrication 	<ul style="list-style-type: none"> - possible presence of slip rings and brushes - high PM demagnetization risk during a sudden short circuit
PM-assisted salient pole SG	Parallel	Radial	<ul style="list-style-type: none"> - simple structure - easy fabrication 	<ul style="list-style-type: none"> - PM thermal danger - problems with PM installations at high speeds - high risk of irreversible PM demagnetization in three-phase short circuits - possible presence of slip rings and brushes
Consequent pole PM hybrid excitation machine (CPPM)	Parallel	Radial/ axial	<ul style="list-style-type: none"> - convenient control - low risk of PM demagnetization - no slip rings and brushes 	<ul style="list-style-type: none"> - low efficiency - field winding tends to increase the outer diameter - manufacturing problems
Hybrid excitation machine with a powdered iron core	Parallel	Radial/ axial	<ul style="list-style-type: none"> - no slip rings and brushes - low risk of PM demagnetization 	<ul style="list-style-type: none"> - manufacturing problems
Hybrid excited flux switching (HEFS) machine	Series	Radial	<ul style="list-style-type: none"> - simple rotor configuration - no slip rings or brushes 	<ul style="list-style-type: none"> - field winding tends to increase the outer diameter

However, in a correctly designed series HESG for island operation, the excitation current in the rotor is needed only to compensate the armature reaction and not to significantly control the air gap flux density. Consequently, the series excitation works perfectly and cannot be regarded as a drawback. Thus, instead of the excitation winding, the rotor winding could be called a compensating winding, and the whole machine ‘an armature-reaction-compensated permanent magnet synchronous generator’ (ARC-PMSG). Of course, the compensating winding does not compensate the q-axis armature reaction but only the d-axis one. The power factor $\cos\varphi = 0.8_{\text{ind}}$ results in a large demagnetizing component on the d-axis, and therefore, a q-axis compensator is not necessary as it is not necessary in traditional SGs either.

Applying the same principles of a series HESM, Figs. 2.2b–2.2d present the proposed topologies of the HESGs. The proposed HESGs employ the same identical laminated stator iron cores as for the conventional EESG illustrated in Fig. 2.2a. The rotor iron cores contain PMs and field winding coils. Table 2.3 provides the main geometry data of the proposed HESGs. The materials used in the HESGs are the same as for the EESG. The main disadvantage of these machines is the possible presence of slip rings and brushes. Since the structures and operation principle of the proposed machines resemble PMSMs because the PM poles still produce a large enough air gap flux density even without electrical excitation, the maintenance of brushes is easier than it would be for the conventional EESG. In emergency cases, the machines should work satisfactorily without any excitation current with a slightly reduced load.

The topology shown in Fig. 2.2b is called the 6-2 HESG because it has six PM poles and two EE poles. There are two PMs embedded in a V position in each of the PM poles. The 6-2 HESG resembles the SynPM machine, which has four PM poles and two EE poles. In reality these are two different topologies. As it was mentioned above, the electrical poles in the SynPM machine have different polarities, which can be produced only when the number of pole pairs is odd; $p = 3, 5, 7$ etc., which includes one pair of EE poles. The proposed construction has the pole pair number $p = 4$, in other words, the pole pair number is even. In such machines where the number of pole pairs is even, $p = 2, 4, 6, 8$ etc., the electrically excited poles will always have the same polarity and the flux is not circulated between two field winding poles. The SynPM machine can also be used among the proposed constructions, but this will require the application of a frequency converter on the grid to maintain the desired speed. To avoid the use of extra devices, the SynPM machine is not considered. The compensating windings of the 6-2 version do not fully compensate the armature reaction as the effect of the field windings is limited to certain physical sectors of the machine. This is why the compensating capability of the version is somewhat weaker than the compensating capabilities of the 4-4 and 8-8 versions presented in the following sections.

The structure illustrated in Fig. 2.2c has four pairs of both PM and EE poles. In such a construction, the PMs and the excitation coils are located in every pole, and the flux resulting from the electrical excitation passes through the PMs. Since the current linkages are connected in series, the machine can be described as the ARC-PMSG with

series current linkages (ARC-PMSG with SCL). The PMs are embedded into the pole shoe leaving some space for iron bridges (iron space between the PM and the edge of the pole shoe).

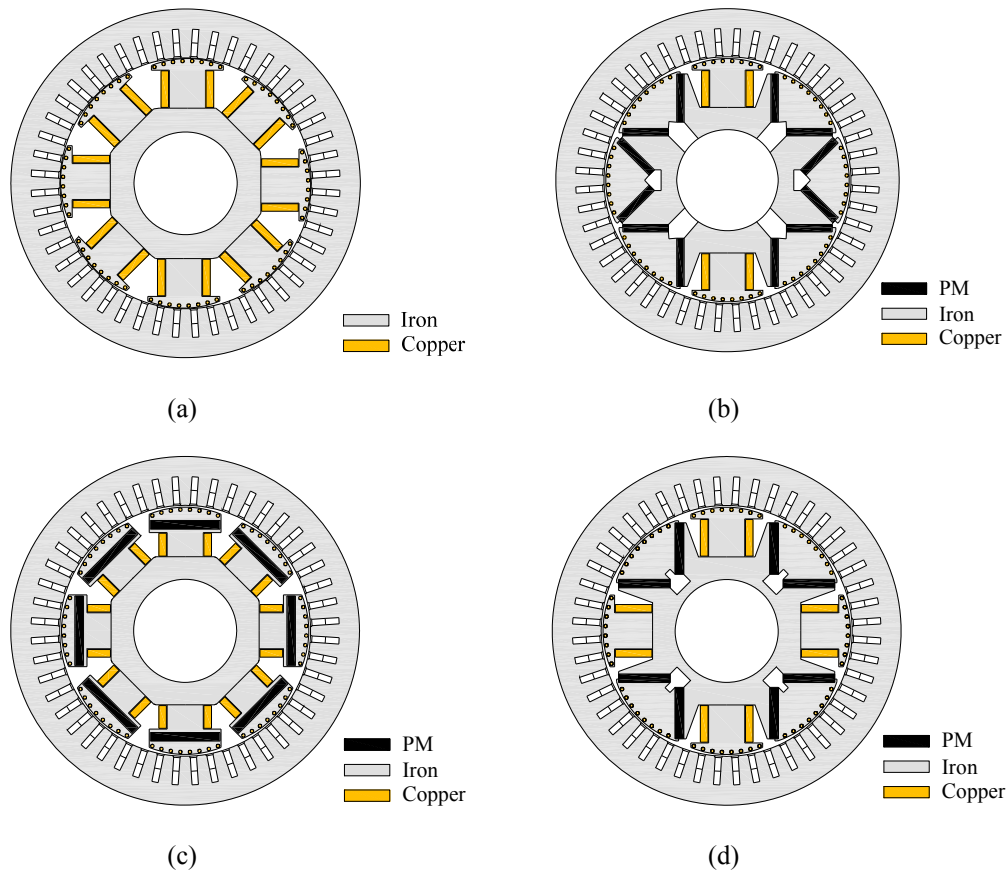


Fig. 2.2: Designed SGs with different excitations.

(a) EESG.

(b) 6-2 HESG.

(c) 8-8 ARC-PMSG with SCL.

(d) 4-4 ARC-PMSG with ACL.

The topology shown in Fig. 2.2d has four PM poles with the same polarity and four EE poles again with the same but opposite polarity. The current linkages of the PMs and the field windings are alternated in this topology. When the rotor is rotated, a phase of the stator winding alternatively sees the current linkages of the PMs or the field windings. Therefore, this topology can be termed as the ARC-PMSG with alternated current linkages (ARC-PMSG with ACL). There are two PMs embedded in a V position in each of the PM poles. What is special to this topology is that all of its PM poles are of the

same polarity. At no load this causes a slight magnetic unbalance in the machine with a small DC flux offset. This, however, causes no special harm to the machine operation except that the winding arrangements are limited to some extent.

The proposed HESGs are dimensioned so that at no-load the machines work without electrical excitation, that is, there is only PM excitation. In rated operation, the field winding has some positive current. During a short circuit, the excitation current is also positive to meet the short-circuit requirement. The possible field weakening operation is not used in this study unless the no-load voltage is reduced from 1.1 to 1 p.u. In such a case, a negative field winding current is needed.

2.3 Finite element analysis

To estimate the operation of the SGs, three different simulated tests (no-load, on-load and short circuit) were performed applying the Flux-2D software package by Cedrat Ltd.

2.3.1 No-load test

In the no-load test, the rotor of the generator is rotated at the nominal speed and the electrical excitation is changed. Each phase of the generator outputs is connected to a resistive load, which has a high enough value to imitate an open circuit. Figure 2.3 shows the no-load flux lines of the EESG and the proposed HESGs. The air gap flux density distributions of the SGs are presented in Fig. 2.4.

Figure 2.3 shows that from the electromagnetic point of view, the ARC-PMSGs remain symmetrical at different rotor current linkages. Therefore, modelling only a quarter of the rotor (two poles) is enough; this in turn will decrease the calculation time. Such symmetry also leads to the easy analytic calculation of the machines. In the case of the 6-2 HESG, when there is zero excitation current, the symmetry goes only through half of the model, which allows analysing only half of the generator in the FEA. Such a construction also sets some limitations to the stator winding arrangements. The asymmetry of flux lines per pole in Fig. 2.3b makes the design process of the 6-2 HESG more difficult compared with the ARC-PMSGs. The same is naturally valid for all odd-pole-pair machines.

There are two relatively different magnetic circuits in the 6-2 HESG. The first magnetic circuit consists of the electrically excited and neighbouring PM poles. The second magnetic circuit includes pure PM poles. Both the magnetic circuits should be included in the design procedure.

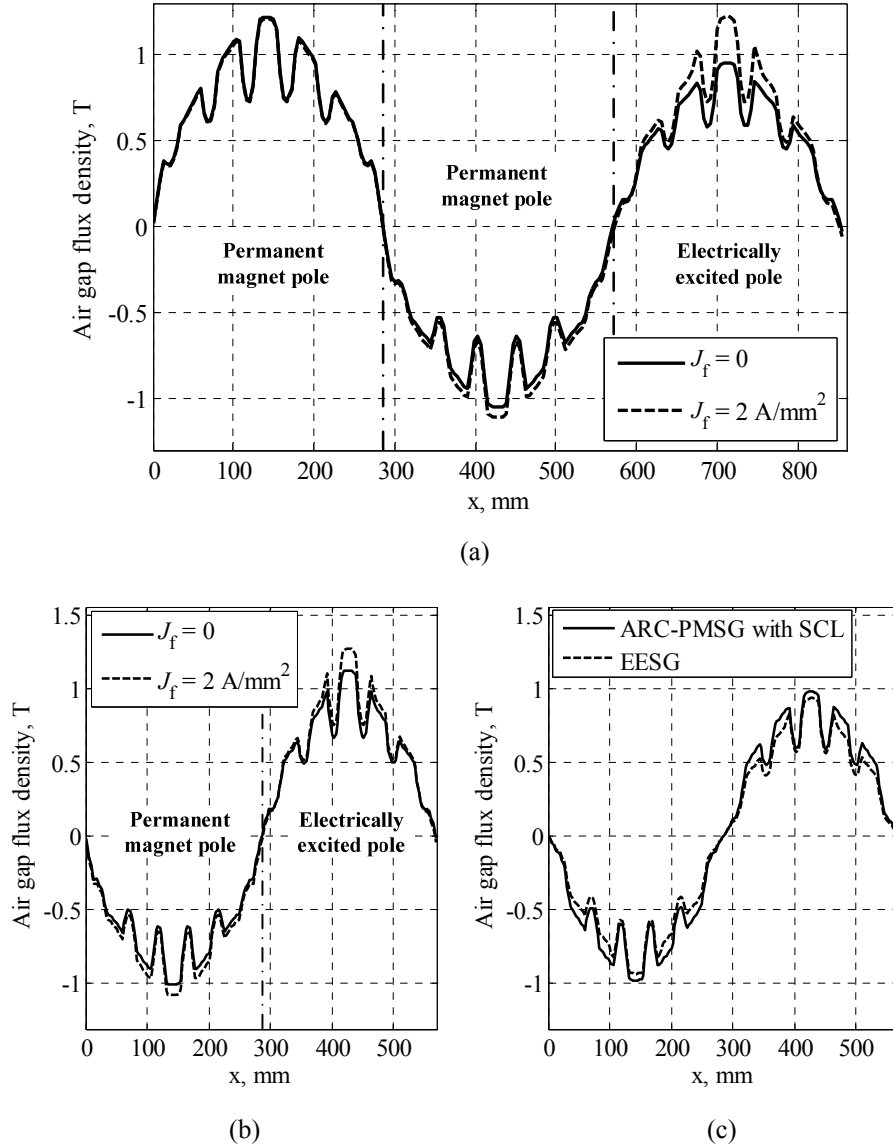


Fig. 2.4: Air gap flux density distributions.
 (a) 6-2 HESG.
 (b) ARC-PMSG with ACL.
 (c) ARC-PMSG with SCL and EESG.

According to Faraday's law, the RMS voltage induced in the conductor under each pole can be expressed as

$$E_{\text{cond}} = B_{\delta} l_c v, \quad (2.1)$$

where B_{δ} is the RMS value of the air gap flux density over a pole, l_c is the length of the conductor and v is the surface speed, which can be expressed as

$$v = \frac{\pi D_{\delta} n}{60}, \quad (2.2)$$

where D_{δ} is the air gap diameter and n is the rotational speed in [rpm].

Table 2.5: Fundamental components of the air gap flux densities at three different excitation current densities for the SGs.

Parameter	EESG	6-2 HESG	ARC-PMSG with SCL	ARC-PMSG with ACL
$B_{1\delta\text{peak}}, T$ at $J_f = 0$ p.u.	0	0.96 (1 p.u.)	0.87 (1 p.u.)	0.93 (1 p.u.)
$B_{1\delta\text{peak}}, T$ at $J_f = 1$ p.u.	0.94 (1.22 p.u.)	1.06 (1.1 p.u.)	0.96 (1.1 p.u.)	1.02 (1.1 p.u.)
$B_{1\delta\text{peak}}, T$ at $J_f = -1$ p.u.	-0.94 (-1.22 p.u.)	0.68 (0.71 p.u.)	0.78 (0.9 p.u.)	0.71 (0.76 p.u.)

Based on Eq. (2.1), the voltages induced in the conductors under different poles will have different values in the 6-2 HESG and the ARC-PMSG with ACL because they have different air gap flux densities under different poles. This effect causes some limitations in the winding arrangement of these machines. In the case of the EESG and the ARC-PMSG with SCL there are no limitations in the winding arrangement because of the symmetrical air gap flux densities.

A common winding used in diesel generators is an ordinary three-phase double-layer distributed winding, and it is therefore applied to the following analysis also. In a three-phase double-layer distributed winding, the number of coil groups is equal to the number of poles $2p$. Therefore, the maximum number of parallel paths a in this winding is equal to the number of poles $2p$. For example, in the considered SGs, the winding can be made with $a = 1, 2, 4$ and 8 . Figure 2.5 presents the winding arrangement of the ARC-PMSG with ACL and the rotor pole positions when the voltage induced in the coils is due to one pole, which is either electrically or PM excited.

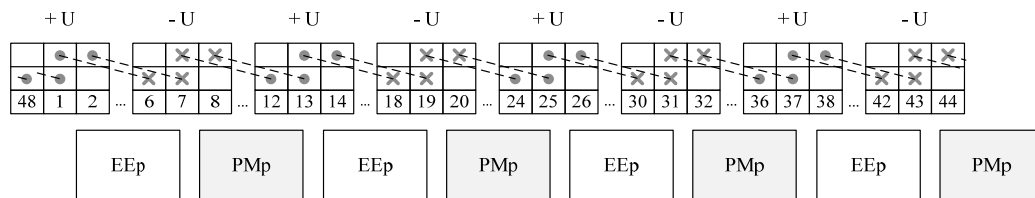


Fig. 2.5: Winding arrangement of the ARC-PMSG with ACL of the phase U. Notations: EEp is the EE pole and PMp is the PM pole.

Figure 2.6 shows the connection of the winding coils in the ARC-PMSG with ACL. In Fig. 2.6a, the winding contains eight parallel paths, whereas in Fig. 2.6b, the winding has four parallel paths. Observing these connections, it is evident that the winding of this machine with $a = 8$ will have unbalanced parallel paths, that is, the voltages induced in the parallel paths will be different. This in turn produces circulating currents in the winding, and as a result, unnecessary copper losses. However, the winding with $a = 4$ gives balanced parallel paths. Therefore, the maximum allowable number of parallel paths for the ARC-PMSG with ACL is $a = p$.

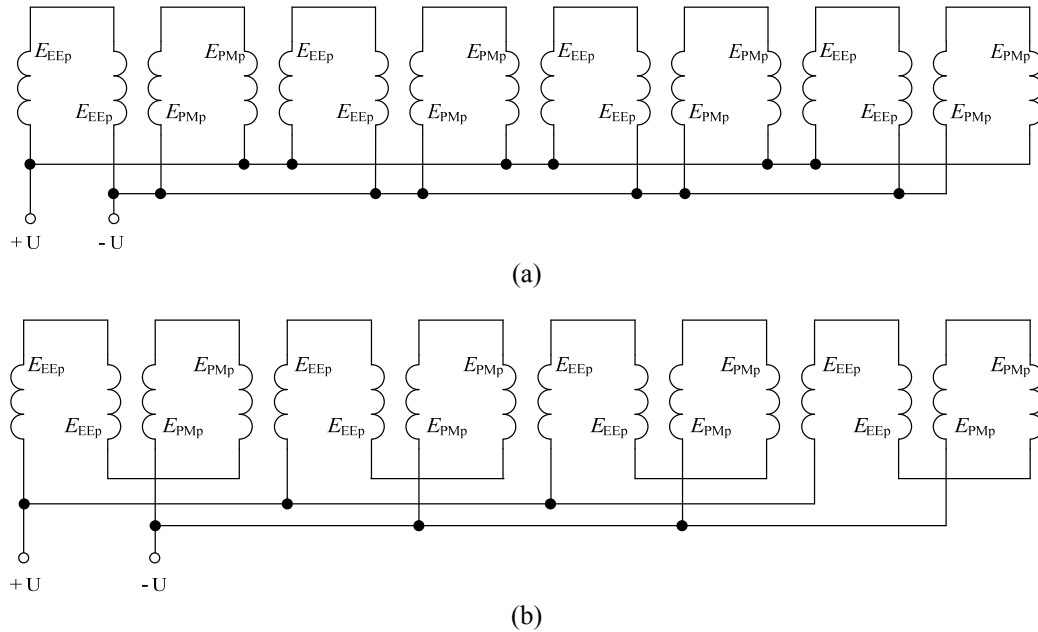


Fig. 2.6: Connection of the winding coils in the ARC-PMSG with ACL.

(a) Winding contains eight parallel paths (not feasible).

(b) Winding contains four parallel paths.

Notations: E_{EEp} is the EMF due to the EE pole and E_{PMp} is the EMF due to the PM pole.

In the case of the 6-2 HESG there are three poles at a run with different air gap flux density magnitudes in the machine. Figure 2.7 provides the winding arrangement of the 6-2 HESG and the rotor pole positions when the voltage induced in the coils is due to one pole, which is either electrically or PM excited.

As it can be seen in Fig. 2.7, if the stator winding of the 6-2 HESG is connected with $a = 8$, obviously, the winding will contain unbalanced parallel paths similarly as in the ARC-PMSG with ACL. The same situation with unbalanced parallel paths occurs when the winding of the 6-2 HESG contains $a = 4$, see Fig. 2.8a. However, when $a = 2$, see Fig. 2.8b, the voltages induced in the parallel paths are equal, and thus, the parallel paths are equal. Therefore, the winding of the 6-2 HESG is limited to two parallel paths.

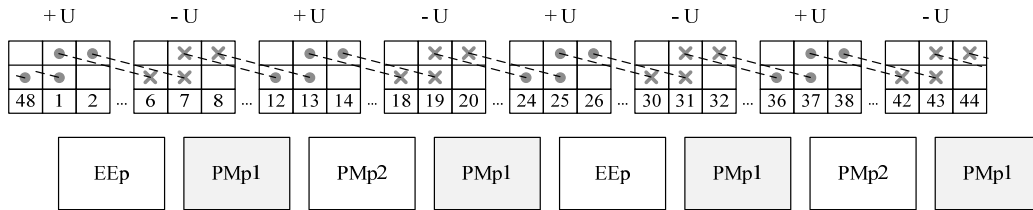


Fig. 2.7: Winding arrangement of the 6-2 HESG. Notations: EEp is the EE pole, PMp1 is the PM pole close to the EE pole and PMp2 is the PM pole next to the previous one.

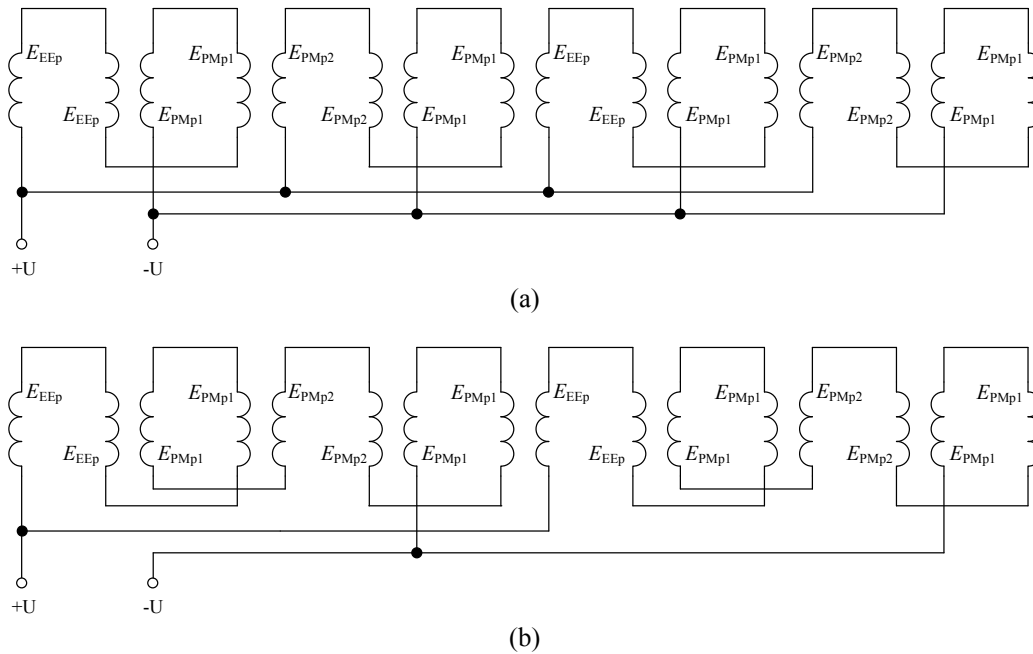


Fig. 2.8: Connection of the winding coils in the 6-2 HESG. (a) Winding with four parallel paths (not feasible). (b) Winding with two parallel paths. Notations: E_{EEp} is the EMF due to the EE pole, E_{PMp1} is the EMF caused by the PM pole close to the EE pole and E_{PMp2} is the EMF caused by the PM pole next to the previous one.

Yet another effect resulting from the different magnitudes of air gap flux densities in the 6-2 HESG and the ARC-PMSG with ACL is the saturation of some teeth at no load. Nevertheless, this saturation is slight, and under load the difference between the magnitudes of air gap flux densities under different poles becomes smaller.

Despite the original purpose of the armature reaction compensation according to Fig. 2.4 and Table 2.5, the air gap flux densities effectively change as the electrical excitation current varies. When the field winding current is positive, it strengthens the rotor excitation, and the air gap flux density increases compared with the case of no electric excitation current. According to Table 2.5, the variation ranges of the air gap flux densities compared with the no-load air gap flux density or 1 p.u. at the excitation current density of 1 p.u. reach 10 % for all proposed HESGs. When the field winding current is negative, it weakens the rotor excitation, and the air gap flux density decreases compared with the air gap flux density corresponding to a zero excitation current.

The maximum values of the air gap flux densities of the 6-2 HESG and the ARC-PMSG with ACL, especially under PM poles, seem somewhat higher than the common values (0.85–1.05 T). Nevertheless, the normal components of the flux densities in the stator teeth and yoke are within acceptable limits given in (Pyrhönen et al., 2008) to avoid saturation. Table 2.5 and Fig. 2.4 demonstrate the general operation principle of an HESM: the PM source provides the air gap with a constant current linkage, and the excitation winding acts as the flux regulator to adjust the air gap flux distribution and the total amount of flux.

According to the machine constraints, the generator voltage must be kept between ± 10 % in all cases. Thus, all the machines are designed so that at no load the field winding current is equal to zero and the no-load induced phase voltage $E_{PM} = 1.1$ p.u.

2.3.2 On-load test

In this test, the generator is rotated at the nominal speed, and it supplies the load at three different power factors: $\cos \varphi = 0.9_{\text{cap}}$, $\cos \varphi = 1$ and $\cos \varphi = 0.8_{\text{ind}}$. The active-capacitive and pure resistive loads are studied to observe the terminal voltage of the SGs, while the active-inductive load is used to calculate the efficiencies of the SGs at nominal power, that is, 400 kW.

Figure 2.9a provides the curves of the terminal voltages of the SGs as a function of load current when the excitation current of the EESG is equal to its nominal value and the proposed HESGs work without electrical excitation, that is, $U_s = f(I_s)$ at $i_f = \text{const}$, $\cos \varphi = \text{const}$ and $f = f_n$. According to these curves, the voltages of the SGs at $\cos \varphi = 0.9_{\text{cap}}$ are more than the allowed maximum value, in other words, 110 % of the rated voltage. This is because of the magnetizing armature reaction. To get the allowed terminal voltage, the excitation current must be decreased. Figure 2.9b demonstrates how the excitation current must be changed to get the rated voltage, that is, $i_f = f(I_s)$ at $U_s = 1$ p.u., $\cos \varphi = 0.9_{\text{cap}}$ and $f_n = \text{const}$. At a pure resistive load the voltages of all proposed HESGs are within the allowed range, that is, ± 10 % of the rated value, whereas the terminal voltage of the EESG at the rated excitation current is above 1.1 p.u, see Fig. 2.9a.

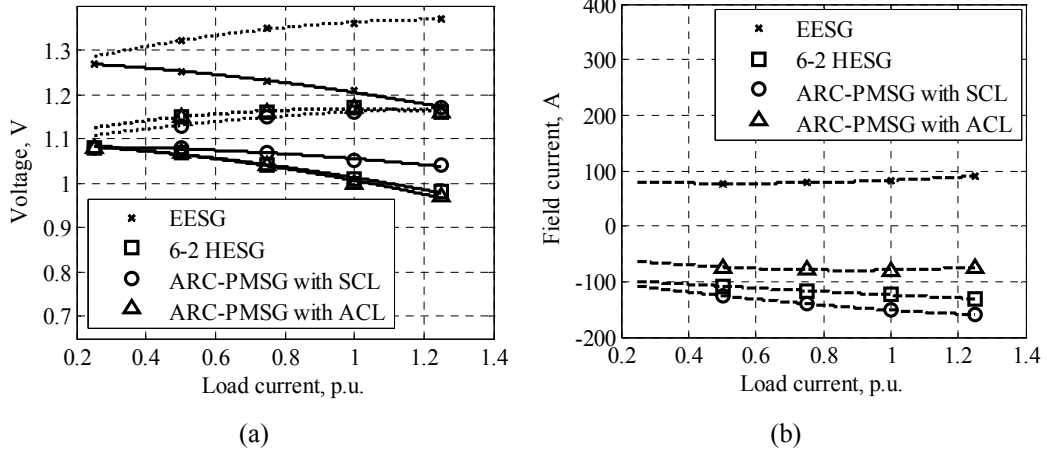


Fig. 2.9: Characteristics of the SGs.

(a) Terminal voltage as a function of load current, $U_s = f(I_s)$ at $i_f = \text{const}$, $\cos \varphi = \text{const}$ and $f = f_n$. The dotted lines refer to $\cos \varphi = 0.9_{\text{cap}}$ and the solid ones correspond to $\cos \varphi = 1$. The curves of the 6-2 HESG and the ARC-PMSG with ACL coincide. The excitation current of the EESG is the nominal value, while the proposed HESGs have a zero excitation current.

(b) Excitation current as a function of load current, $i_f = f(I_s)$ at $U_s = 1$ p.u., $\cos \varphi = 0.9_{\text{cap}}$ and $f_n = \text{const}$.

As it can be seen in Fig. 2.9b, the excitation current of the EESG is positive while the excitation currents of the proposed HESGs must be negative to get $U_s = 1$ p.u. This requirement must be taken into account in the excitation system of the proposed HESGs.

In general, the machine efficiency is a ratio of the output to input powers, where the last term is a sum of the output power and the total losses. The total losses of an SG include mechanical losses, stator and rotor copper losses, stator iron losses and additional losses. The losses of the proposed HESGs can also contain PM losses. The efficiencies, loss distributions and power densities in the rated point of different SGs are given in Table 2.6.

Mechanical losses are a consequence of bearing friction and windage. Bearing losses depend on the shaft speed, bearing type, properties of the lubricant and the load on the bearing. The overall mechanical losses of the horizontal-shaft salient pole generator can be expressed according to (Kasyanov, 1951) as

$$P_{\text{mech}} = 1.83 \cdot 2p \sqrt{l_1} \left(\frac{v}{40} \right)^3, \quad (2.3)$$

where $2p$ is the number of poles, l_1 is the stator length and v is the surface speed.

Table 2.6: Efficiencies, loss distributions and power densities of SGs in the rated operating point.

Parameter	EESG	6-2 HESG	HESG with SCL	HESG with ACL
Mechanical losses, W	6400	5800	6200	6000
Stator iron losses, W	3900	4600	4300	4600
PM losses, W	0	6.4	4	4
Stator copper losses, W	2500	2400	2500	2400
Rotor copper losses, W	10300	5800	3400	3100
Additional no-load losses, W	2000	2000	2000	2000
Additional on-load losses, W	2000	2000	2000	2000
Output power, W	400000	400000	400000	400000
Efficiency, %	93.65	94.65	95.15	95.22
Power density, W/kg	146	169	153	159

The stator and rotor copper losses are the Joule losses expressed as

$$P_{s,Cu} = m I_s^2 R_s \quad (2.4)$$

$$P_{r,Cu} = I_f^2 R_f \quad (2.5)$$

where m is the number of phases, I_s is the stator phase current, R_s is the stator phase resistance, I_f is the field winding current and R_f is the field winding resistance.

The stator iron losses and PM losses are estimated by the FEA. According to (Ugalde et al., 2009), the eddy current losses in PMs are calculated as the active power dissipated in these regions considering the magnets as solid conductors. The losses in electrical sheets are computed by the tool termed as Loss Surface Model (LSM) which is integrated in the FEM software FLUX®.

The additional losses can be divided into two types: no-load and on-load additional losses. The first ones occur at no-load and do not change as a function of load. The load-dependent additional losses are generated when the load current increases. At no-load, because of the stator slot openings, the air gap flux density pulsates, which in turn produces circulating losses on the rotor pole shoes. The on-load additional losses appear

- in the stator teeth as a result of the third harmonic in the resultant magnetic flux. There is a third harmonic in the magnetic flux because of the excitation and a third harmonic in the armature reaction;
- on the rotor poles shoes as a result of the tooth harmonics in the stator current linkage,
- in the stator press plate as a result of the end leakage fluxes
- and also in the mechanical parts of the machine.

The calculation of the additional losses includes the calculations of the additional losses both in the no-load and on-load operation.

The no-load additional losses are the surface losses resulting from the fluctuations in the air gap flux density. The air gap flux density always decreases at the slot opening and increases at the tooth part. The frequency of such fluctuations depends on the number of slots and rotational speed. The additional losses at no load can be determined as in (Kopylov et al., 2005)

$$P_{\text{add,nl}} = 0.5 \cdot 2p \alpha_p \tau_p l_1 k_0 \left(\frac{Q_s n}{10^4} \right)^{1.5} (B_{1\delta} (k_{C1} - 1) \tau_{us} \cdot 10^3)^2 \cdot 10^{-3}, \quad (2.6)$$

where $2p$ is the number of poles, α_p is the relative pole width, τ_p is the stator pole pitch, l_1 is the stator core length including cooling channels, Q_s is the stator slot number, n is the rotational speed in [rpm], τ_{us} is the stator slot pitch, k_0 is equal to 4.6, 8.6 and 23.3 for the 1 mm and 2 mm core sheet thicknesses of the rotor pole and solid pole shoes, respectively, $B_{1\delta}$ is the fundamental harmonic of the air flux density and k_{C1} is the Carter factor for the stator slots assuming a smooth rotor using for example the equations given in (Pyrhönen et al., 2008).

The additional losses in on-load operation for the machines with the active power lower than 1 MW are assumed 0.5 % of the generator output power P_n , whereas for the generators with $P_n > 1$ MW they are determined as (0.25–0.4) % of the generator output power P_n . These values are determined for the rated power; to calculate the additional losses for other power values, the following expression can be used (Pyrhönen et al., 2008)

$$P_{\text{add}} \sim I_s^2 f^{1.5}, \quad (2.7)$$

where I_s is the stator current and f is the frequency.

As it can be seen in Table 2.6, the PM losses can be neglected. In actual machines there should be no significant PM losses because the PMs are buried quite deep. Moreover, because of the presence of the damper winding and the rotor lamination, the flux produced by the high harmonics should not penetrate deep enough.

According to the calculated results, the efficiencies and power densities of HESGs are higher compared with the EESG. The ARC-PMSGs have higher efficiencies than the 6-2 HESG, whereas the 6-2 HESG has the highest power density because it is the shortest construction.

2.3.3 Short-circuit test

The short-circuit test is carried out to verify whether the short-circuit requirement mentioned in the machine constraints is met: the sustained short-circuit current must be

300 % of the rated current for at least 2 s. This condition is one of the most challenging requirements for pure PMSGs. During the test, the generator is rotated at the nominal speed, and all the three output phases are short circuited through switches. At the beginning, the switches are turned off and the generator is running at no load. After 0.0333 s (two periods), the switches are turned on. The objective of the test is to observe the sustained short-circuit current. The results of the short-circuit tests are given in Table 2.7.

Table 2.7: Results of the short-circuit test.

Parameter	EESG	6-2 HESG	ARC-PMSG with SCL	ARC-PMSG with ACL
Sustained short-circuit current, I_{sc}	2040 A	2240 A	2880 A	2190 A
Field winding current linkage, Θ_f	9970 A/pole	11460 A/pole	3360 A/pole	5480 A/pole
Number of poles excited electrically	8	2	8	4
Sum on field winding current linkages	79760	22920	26880	21920
Current ratio, I_{sc}/I_s	3	3.5	4.5	3.4

As it can be seen in Table 2.7, the ARC-PMSGs have lower current linkages per pole than the EESG and 6-2 HESG to meet the short-circuit requirement. However, the sum of the compensating current linkages is in the same range in all the HESGs. With the ARC-PMSG with SCL and the ARC-PMSG with ACL, the minimum desired short-circuit current is achieved at 1.7 A/mm² and 2.75 A/mm², while with the EESG and the 6-2 HESG, the field current densities are 5 A/mm² and 5.75 A/mm². The results of the short-circuit test fully demonstrate that all SGs can meet the short-circuit requirement.

2.4 Excitation systems of the generators

As the studied generators have field windings, an excitation control system supplying field winding current is needed. This is a disadvantage compared with a pure PM generator. However, this excitation system ensures the option to control the island voltage or the reactive power balance of the machine and to provide the short-circuit current required by the standards.

Different excitation systems are considered for example in (Kundur, 1994; Pyrhönen, 2007; Lipo, 2011). In principle, there are two methods to magnetize a separately excited machine:

1. with slip rings and brushes and
2. brushless excitation.

In the first method, the excitation current is conducted through slip rings to the field winding in the rotor. In island operation, the excitation current is supplied by a PMSG through a thyristor bridge, as shown in Fig. 2.10. The rotor of the PMSG is mounted on the same axis as the EESG, and therefore, the mechanical power needed for the excitation is obtained from the prime mover shaft. In network operation, the field winding can be fed from the grid by a thyristor bridge. A drawback of this method is that the excitation current passes through the slip rings of the EESG, and therefore, brushes are required. These brushes can carry high currents and therefore require constant maintenance. In comparison with the brushless system, the method where the excitation current is brought through slip rings and brushes gives a fast-responding excitation control despite the high inductance of the field winding.

In the second method, the brushless system, there are three machines on the same shaft in island operation: 1) the main SG, that is, the EESG; 2) either an outer pole SG having its field windings in the stator and the armature on the rotor or a wound rotor IM supplying the field winding current for the main machine; and 3) a PMSG, which supplies the power to the second machine, see Fig. 2.11. In network operation, the third machine can be replaced with the grid, and therefore, the second machine is excited with a network supply. A thyristor bridge is needed to control the current. On the rotating rotor there is also a diode bridge that rectifies the current supplied by the second machine. A brushless system gives a maintenance-free EESG. However, the excitation current is changed by the time constants of the three machines, which results in a slow control of the excitation current. This is a disadvantage of the method.

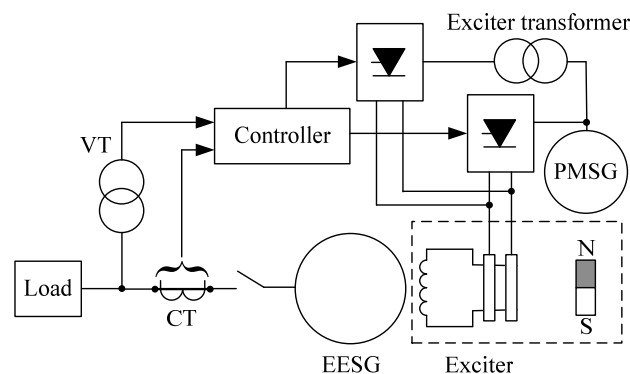


Fig. 2.10: Excitation system of the slip-ring EESG.

During a short circuit, a large field winding current can be supplied through the exciter transformer.

Notations: VT is the voltage transformer to the terminal voltage and CT is the current transformer to measure the current.

The proposed HESGs can use the same excitation methods as the EESG to supply the DC current to the field winding. Figure 2.12 presents the excitation system of the proposed HESGs where the excitation current is brought through slip rings. Since the

proposed machines are dimensioned so that at no load the field winding current is equal to zero, the excitation system is needed only during the on-load and short circuit. As the proposed HESGs produce a constant E_{PM} , the excitation energy can be taken from the machine terminals through the power transformer. To ensure a sufficient short-circuit field winding current, the excitation system could be equipped for instance with a supercapacitor supplying the field winding current during a stator short circuit and zero terminal voltage. To supply a negative field winding current, antiparallel thyristor bridges operated in a four-quadrant current-voltage plane are needed.

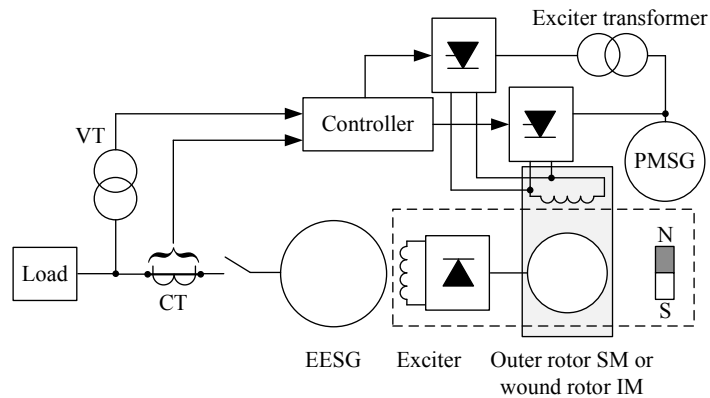
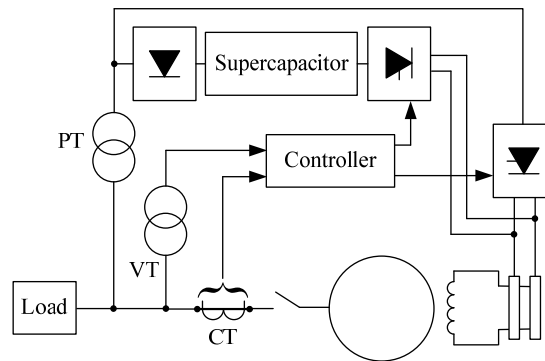


Fig. 2.11: Excitation system of the brushless EESG.

During a short circuit, a large field winding current can be supplied through the exciter transformer.

Notations: VT is the voltage transformer to the terminal voltage, and CT is the current transformer to measure the current.



6-2 HESG or ARC-PMSG

Fig. 2.12: Excitation system of the proposed slip-ring HESGs.

During a short circuit, the excitation system can be equipped with a supercapacitor to ensure a sufficient short-circuit current.

Notations: PT is the power transformer to supply the excitation system, VT is the voltage transformer to the terminal voltage, and CT is the current transformer to measure the current.

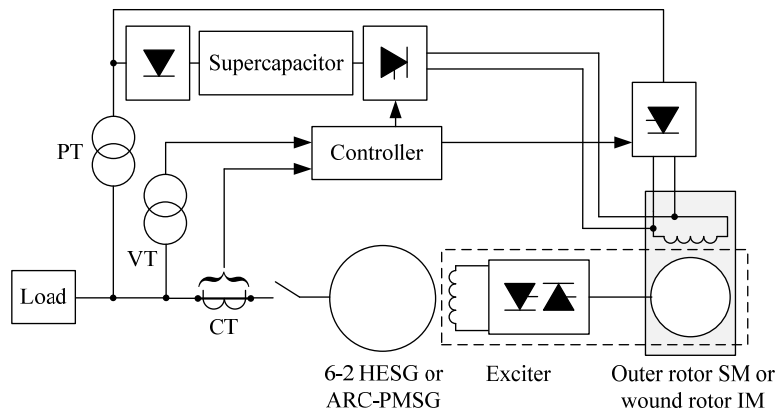


Fig. 2.13: Excitation system of the proposed brushless HESGs.

During a short circuit, the excitation system can be equipped with a supercapacitor to ensure a sufficient short-circuit current.

Notations: PT is the power transformer to supply the excitation system, VT is the voltage transformer to the terminal voltage, and CT is the current transformer to measure the current.

In the case of the brushless method, the excitation system becomes more complex to implement as rotating controlled electronics are needed, see Fig. 2.13. To produce the excitation power for the field winding, an additional outer rotor SM or a wound rotor IM mounted on the common shaft is needed. A diode bridge is rotated together with the shaft to rectify the current supplied by the additional machine. To conduct the excitation current in two directions, antiparallel thyristor bridges operated in a four-quadrant current-voltage plane are required.

A brushed system is the most inexpensive solution to control the excitation in a hybrid generator. However, the brushes should last long as the field winding current in rated operation should be low when the generator is correctly designed. The benefits of the slip ring system are that it can easily change the direction of the field winding current and yields a fast-responding excitation control.

2.5 Comparison of SGs

The results of the FEA showed that all the SGs can meet the set requirements. However, the proposed HESGs showed better performances than the EESG. The proposed HESGs can work without electrical excitation in no-load operation, while in rated operation they can supply inductive loads with a load power factor $\cos\varphi = 0.8_{\text{ind}}$, and during the short circuit, they can all meet the short-circuit requirement. A comparison of the active masses of the studied SGs is shown in Table 2.8.

Table 2.8: Active mass comparison of the SGs.

Masses	EESG	6-2 HESG	ARC-PMSG with SCL	ARC-PMSG with ACL
PM, kg	0	120	150	110
Stator iron, kg	1010	820	930	880
Rotor iron, kg	820	750	740	780
Rotor copper, kg	660	610	640	620
Stator copper, kg	250	60	150	120
Total mass, kg	2740	2360	2610	2510

According to Table 2.8, the proposed HESGs have lower total masses than the EESG. The 6-2 HESG has the lowest total mass. Regarding the PM mass, the ARC-PMSG with ACL has the lowest mass of the PMs. In general, modern PM materials are the most expensive components in an electrical machine. Therefore, considering the machine cost, the HESG with ACL seems the best one of the versions studied.

Figure 2.14 demonstrates a comparison of the calculated efficiencies of the SGs with different excitations. The efficiencies are calculated based on the results of the rated load test, that is, all the SGs supply inductive loads with a load power factor $\cos\varphi = 0.8_{\text{ind}}$, and the electrical load is varied in the range of 25–125 % of the nominal load. As can be seen in Fig. 2.14, the efficiencies of the HESGs are obviously higher than that of the EESG in the range of 25–110 % of the nominal load. The maximum values of the efficiencies of the EESG, the 6-2 HESG, the ARC-PMSG with SCL and the ARC-PMSG with ACL are 93.76 %, 95.17 %, 95.27 % and 95.32 %, respectively.

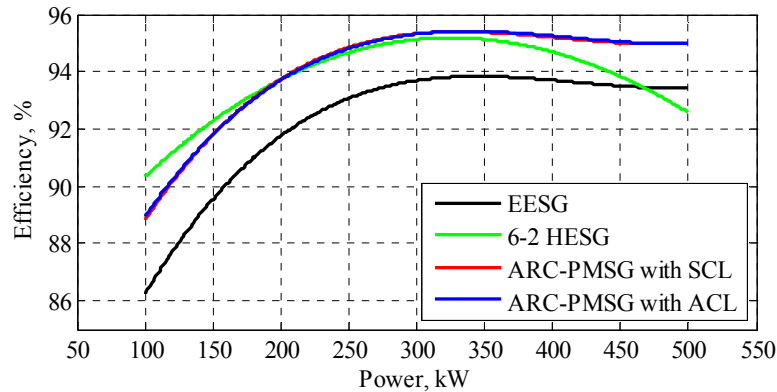


Fig. 2.14: Comparison of the efficiencies of the SGs with different excitations. The efficiencies of the ARC-PMSGs are on top of each other.

The results in Table 2.6 and Fig. 2.14 show that the efficiencies of the ARC-PMSGs are higher compared with the 6-2 HESG mainly because of the rotor copper losses. This can be explained by the fact that the electrically excited poles of the 6-2 HESG compensate

the armature reaction non-uniformly, whereas the ARC-PMSGs have more symmetrical compensating windings, which evenly compensate the armature reaction. The 6-2 HESG needs more excitation current to compensate the armature reaction.

2.6 Economic aspects

Despite the fact that the proposed HESGs have better efficiencies and power densities than the conventional EESG, they can be criticized for the expensive NdFeB PMs, which essentially increase the total price of the generators. Therefore, an economic comparison of the proposed HESGs with the EESG is required. It is emphasized that all the calculations are simplified.

In 2012, the price for a small order of a non-oriented fully processed electrical steel M600-50A coated and cut to a width according to the customer's wish was about 1 €/kg, including delivery (Surahammars Bruk, 2013). Let us assume that the prices for the electrical and constructional steels installed are the same, and they are 2 €/kg.

By assuming that the price for insulated copper wire is 10 €/kg, it is possible to calculate the material cost of iron and copper, which is approximately 60–70 % of the total material cost (iron and copper + insulation, frame, bearings with end shields etc.).

The price for the PM material depends for instance on the quantity, delivery time schedule, magnet shape, dimensional tolerances and surface quality. Therefore, the PM price has to be evaluated case by case. For the sake of simplicity, it is supposed that the PM price of Neorem 493a (Neorem Magnets, 2008) is 150 €/kg.

The use of PM material does not usually make the production process more difficult to manage. Assuming that the manufacturer's profit is 25 % of the total material cost, the generator price is

$$\begin{aligned} \text{Generator price [€]} &= \\ &= \text{PM price [€]} \times 1.25 + (\text{Iron price [€]} + \text{Copper price [€]}) \times 1.6 \times 1.25. \end{aligned} \quad (2.8)$$

The calculated generator prices are presented in Table 2.9.

Table 2.9: Calculated SG prices.

Material	EESG	6-2 HESG	ARC-PMSG with SCL	ARC-PMSG with ACL
NdFeB PM	0	18000	22500	16500
Iron (stator + rotor)	3700	3200	3400	3400
Copper (stator + rotor)	9100	6700	7900	7400
Generator price	25600	42200	50700	42100

In general, the fuel consumption of a genset depends on the fuel consumption of the diesel engine acting as the prime mover. Based on this, the annual fuel consumption in [€] can be expressed as

$$\begin{aligned} \text{Annual fuel consumption [€]} &= \frac{P_{\text{out}} [\text{kW}]}{\eta} \times \\ &\times \frac{\text{diesel engine consumption} \left[\frac{\text{kg}}{\text{kWh}} \right]}{\rho_{\text{diesel}} \left[\frac{\text{kg}}{\text{l}} \right]} \times t [\text{h}] \times C_d \left[\frac{\text{€}}{\text{l}} \right], \end{aligned} \quad (2.9)$$

where P_{out} is the output power of the generator, η is the generator efficiency, ρ_{diesel} is the diesel mass density, t is time and C_d is the diesel fuel price per litre.

Assuming that the annual maintenance cost is 10 % of the annual fuel consumption, the annual operating cost is

$$\text{Annual operating cost [€]} = 1.1 \times \text{Annual fuel consumption [€]}. \quad (2.10)$$

The annual revenue of an HESG is a difference between the annual operating costs of the SG and the HESG. The profit of an HESG genset over its lifetime can be determined as

$$\text{Profit [€]} = \text{Annual revenue [€]} \times T [\text{years}], \quad (2.11)$$

where T is the lifetime of the HESG.

The price of 1 kWh produced by the generator is

$$\text{Electricity price} \left[\frac{\text{€}}{\text{kWh}} \right] = \frac{\text{Annual operating cost [€]}}{8760 [\text{h}] \times P_{\text{out}} [\text{kW}]}. \quad (2.12)$$

The simplified payback period SPP of the HESG can be estimated as

$$\text{SPP} = \frac{\text{Generator price}}{\text{Annual revenue}}. \quad (2.13)$$

Assuming that the SGs operate at rated load for the whole year, Table 2.10 presents the economical efficiencies of the proposed HESGs calculated based on the above simplified considerations, where a four-stroke diesel engine Wärtsilä 4L20 is used as an example. The fuel consumption of this diesel engine at 400 kW is about 0.2 kg/kW/h (Wärtsilä, 2009). The diesel mass density is 0.83 kg/l and the diesel price is assumed to

be equal to 1.14 €/l (ABC, 2012). The lifetime of the generator is assumed to be at least 20 years, for example.

Table 2.10: Economic efficiencies of the proposed HESGs.

Parameter	EESG	6-2 HESG	ARC-PMSG with SCL	ARC-PMSG with ACL
Annual fuel consumption, k€	1028	1017	1012	1011
Annual operating cost, k€	1131	1119	1113	1112
Annual revenue, k€	-	12	18	19
Total profit, k€	-	242	352	374
Electricity price, € cent/kW/h	32.27	31.9	31.8	31.7
SPP, years	-	3.5	2.9	2.3

Table 2.10 shows a good economic performance of the proposed HESGs compared with the EESG. In particular, the HESG with ACL has a better economic efficiency than the HESG with SCL.

2.7 Summary

This chapter dealt with the feasibility of an ARC-PMSG in island operation based on the comparison with the EESG. Four different SGs (EESG, 6-2 HESG and two ARC-PMSGs 4-4- and 8-8) were designed. The operation principle of the proposed ARC-PMSGs was discussed.

The study and comparison of the EESG and the proposed HESGs was made by the two-dimensional (2D) FEA. The results of the FEA showed that all four studied SGs can meet the main requirements for generators. However, the two proposed ARC-PMSGs showed better results than the traditional EESG and the 6-2 HESG especially from the efficiency point of view. This demonstrates that an ARC-PMSG could be the best solution. However, the proposed HESGs have two limitations. The first limitation relates to the stator winding: the base winding has to cover at least one pole pair. Parallel paths of single pole windings are not allowed. Finally, the second one refers to the complex brushless excitation system, if the generator load has an active-capacitive behaviour.

The ARC-PMSG with ACL showed a better performance than the ARC-PMSG with SCL both from the technical and economic point of views:

- high efficiency and high power density;
- low total mass;
- low mass of the expensive rare-earth PM material;
- low electricity price and short simplified payback period.

Therefore, it was decided to study an ARC-PMSG with ACL further.

3 Design procedure of an ARC-PMSG with ACL

In the previous chapter, the ARC-PMSG with ACL demonstrated a better performance than the ARC-PMSG with SCL, and therefore, it was decided to study this topology in more detail. This chapter presents an analytical approach to the design of an ARC-PMSG with ACL. The proposed design includes the electromagnetic design and thermal analysis of the ARC-PMSG with ACL.

3.1 Electromagnetic design

The main stages of the general electromagnetic design applied to the analytical calculation of either conventional EESGs or pure PMSGs can be considered to start from the definition of the machine dimensions, proceeding through the stator and rotor design to the determination of the main characteristics.

Structurally, a stator of an ARC-PMSG with ACL is the same as for conventional AC machines, that is, either asynchronous or synchronous machines. Thus, the stator design for an ARC-PMSG with ACL consists of

- determination of the main dimensions
 - inner and outer diameters;
 - real and equivalent lengths;
 - air gap length;
- determination of the stator winding
 - winding type;
 - number of slots per pole and phase and winding factor;
 - air gap flux density;
 - number of parallel paths and number of phase turns;
 - suitable slot form, teeth width and teeth height;
- calculation of the stator resistance and
- calculation of the stator leakage inductance.

The main characteristics of the HESG include calculation of losses and efficiency, machine parameters and active masses. The total losses include mechanical losses, stator and rotor copper losses, stator iron losses and additional losses, which were discussed in the previous chapter. The corresponding equations for the stator design and active masses can be found for example in (Pyrhönen et al., 2008), and are therefore not repeated here.

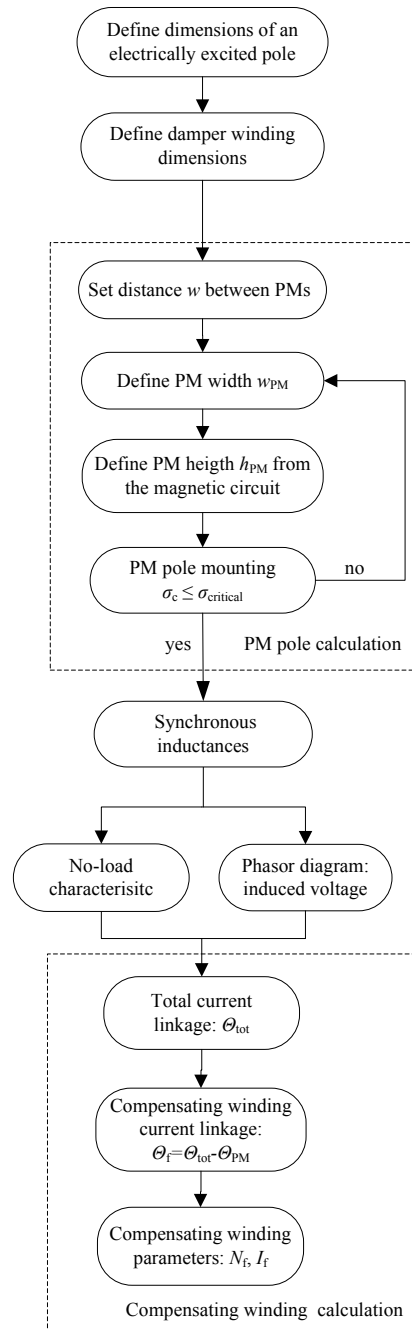


Fig. 3.1: Algorithm for the rotor design of an ARC-PMSG with ACL.

The rotor design includes the calculation of

- electrically excited poles;
- damper winding;
- PM poles and
- compensating winding.

The developed algorithm for the rotor design of an ARC-PMSG with ACL is presented in Fig. 3.1. Every item of this algorithm is described below.

3.1.1 Electrically-excited pole

An electrically excited (EE) pole of an ARC-PMSG with ACL is the same as for a salient-pole SM. The pole core usually consists of laminated sheets of 1–2 mm width, which are punched according to Fig. 3.2. The pole cores are usually made of constructional steel Fe52. To obtain a magnetic flux density that is close to a sinusoidal form, the pole shoes are shaped so that the air gap lengths at the pole edges are (1.5–3) times larger than in the middle, that is, $\delta_{\max}/\delta_0 = 1.5\text{--}3$. It has been shown that the pole can have a form of an arc of a circle having a smaller radius than the stator. According to (Boldea, 2006), the outer rotor radius can be expressed as

$$R_p = \frac{D_\delta}{2 + \frac{8D_\delta(\delta_{\max} - \delta_0)}{b_p^2}}, \quad (3.1)$$

where D_δ is the air gap diameter and b_p is the pole shoe width. The pole shoe width is

$$b_p = \alpha_p \tau_p, \quad (3.2)$$

where $\alpha_p = 0.67\text{--}0.75$ is the pole shoe relative width and τ_p is the pole pitch.

The average air gap length can be determined as in (Soldatenkova and Boronina, 1993)

$$\delta' = \delta_0 + \frac{\delta_{\max} - \delta_0}{3}. \quad (3.3)$$

Figure 3.2 also provides two possible installation methods of a pole core to a rotor yoke. In SMs where the speed is $v_p \approx \pi D_\delta n_{\text{st}}/60 > 30$ m/s, the pole cores are attached to the rotor yoke by a dove tail, Fig. 3.2. In low-speed SMs, the pole cores are attached to the rotor yoke by bolts, which go through the rotor yoke and the round solid rim, see Fig. 3.2b. The screws are tightened from the inner side of the round solid rim.

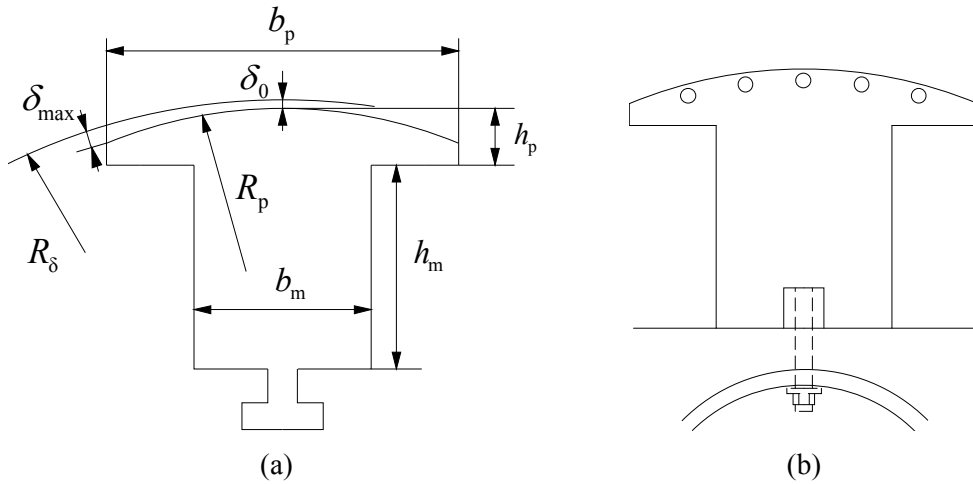


Fig. 3.2: Laminated pole sheet.

(a) Installation of a pole core with a dove tail.

(b) Installation of a pole core with bolts, which go through the rotor yoke and the solid rim.

The lengths of the pole shoe l_p and the pole core l_m are usually the same as the stator length l_1 .

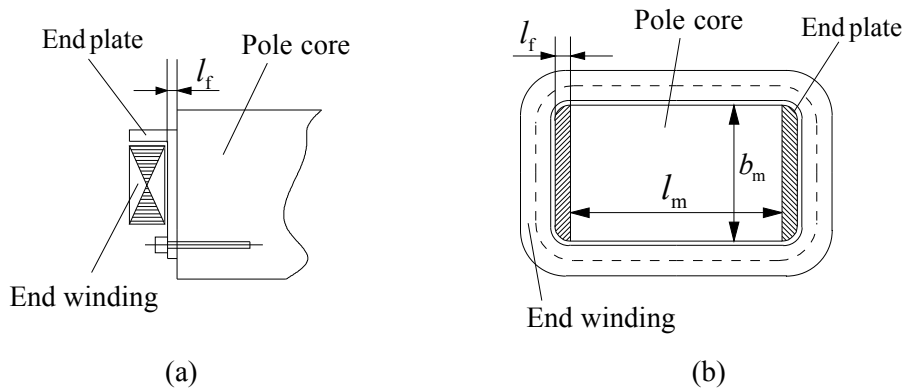


Fig. 3.3: End plates.

(a) Form of the end plate.

(b) Fillet of the end plates.

To support the compensating end winding, the pole core is compressed with the end plates and bolts, which go through the end plates and the laminated sheets of the pole core. The end plates are usually made of forged steel in the form of plates with curved edges or cast steel, see Fig. 3.3a. For the convenient installation of the excitation winding, the end plates are rounded at their edges as shown in Fig. 3.3b.

The thickness of the end plate l_f is selected in the range of $(1.5-3) \times 10^{-2}$ m depending on the dimensions of the pole core.

The pole core width is determined according to the allowable flux density $B_m \leq 1.4-1.6$ T. Based on this, the pole width is

$$b_m = \frac{\alpha_\delta B_{1\delta} \tau_p l'}{B_m k_{r,Fe} (l_m + l_f)}, \quad (3.4)$$

where $k_{r,Fe}$ is the space factor of the pole core.

The determination of the pole shoe height h_p is based on the space required for the damper winding. (Tokov, 1975) suggests to define the pole shoe height h_p as

$$h_p \approx 0.3(b_p - b_m) + d_r, \quad (3.5)$$

where d_r is the diameter of the damper bar.

The pole core height h_m depends on the dimensions of the compensating winding, which are not defined yet. Therefore, it can be preliminarily estimated that (Kasyanov, 1951)

$$h_m \approx 0.016 + 0.186 \sqrt[4]{\tau_p}. \quad (3.6)$$

The final dimensions of the pole shoe h_p and the pole core h_m heights are fixed after the design of the compensating winding.

The length of the rotor yoke l_y is assumed to be the same as the length of the pole core l_m . The height of the rotor yoke h_y can be expressed as

$$h_y = \frac{\alpha_\delta B_{1\delta} \tau_p l'}{2B_y k_{r,Fe} l_y}, \quad (3.7)$$

where B_y is the flux density in the rotor yoke, which is in the range of (1.0–1.3) T.

3.1.2 Damper winding

The design of a damper winding includes the determination of the number and dimensions of the damper bars and the short-circuit end rings presented in Fig. 3.4.

Usually, the material of the damper winding is copper. In some synchronous motor cases, the damper winding is made of brass or bronze to increase the resistance and use this winding as a “starting winding”.

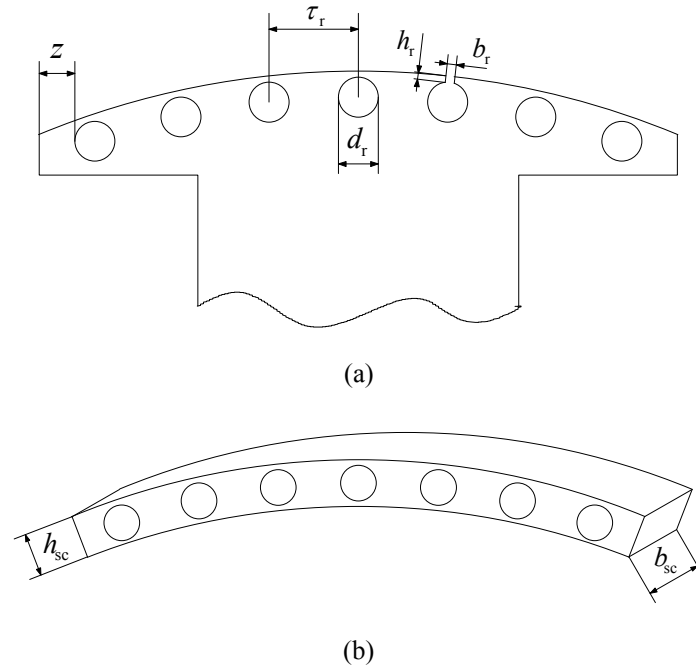


Fig. 3.4: Main parts of a damper winding.
 (a) Damper bars.
 (b) Segment of a short-circuit ring.

According to (Vogt, 1996), the cross-sectional area of all damper bars located in the pole is taken as 20–30 % of the stator winding cross-sectional copper area per pole. The cross-sectional area of the short-circuit ring is selected approximately equal to 30–50 % of the cross-sectional area of the damper bars per pole. In order to reduce additional losses and distortions of the EMF, it is desirable to have the damper winding slot pitch τ_r close to the stator slot pitch τ_s (τ_r should diverge from τ_s by 10–15 %) but not the same. Based on these guidelines, it is possible to design a damper winding.

The cross-sectional area of the damper bar is

$$S_r = \frac{(0.2 \div 0.3) \cdot \tau_p \cdot A_s}{N_r \cdot J_s}, \quad (3.8)$$

where τ_p is the pole pitch, A_s is the linear current density and J_s is the stator current density and N_r is the number of damper bars per pole.

The diameter of the damper bar is then

$$d_r = \sqrt{\frac{4S_r}{\pi}}. \quad (3.9)$$

The result from Eq. (3.9) is usually rounded up to a multiple of 0.5 [mm].

The damper winding slot pitch is

$$\tau_r = \frac{b_p - d_c - 2z}{N_r - 1}, \quad (3.10)$$

where b_p is the pole shoe width, z is the distance between the pole shoe edge and the bar close to it. From the manufacturing point of view it is $z \geq (0.3-0.7) \times 10^{-2}$ [m].

The form of the slot for the damper bar is round and can be closed or semi-closed. The diameter of the rotor slot d_s is equal to $d_c + (1-2)$, [mm]. The length of the damper bar l_c can be estimated as in (Kopylov et al., 2005)

$$l_c = l_p + (0.2 \div 0.4)\tau_p. \quad (3.11)$$

The cross-sectional area of the damper winding end ring is

$$S_{sc} = b_{sc} h_{sc} = (0.3 \div 0.5)N_r S_r. \quad (3.12)$$

where h_{sc} is the height of the end ring and b_{sc} is the end ring thickness.

To make the damper winding robust enough, (Antonov, 1993) suggests to choose the end ring thickness as

$$b_{sc} \geq \frac{2}{3}d_r. \quad (3.13)$$

3.1.3 PM pole

A PM pole core of an ARC-PMSG with ACL consists of laminated sheets of 1–2 mm thickness. The material of the PM pole cores is the same as for the EE pole cores. The PM pole shoes are also shaped in the same way as the EE pole shoes to obtain an air gap magnetic flux density that is close to sinusoidal, and therefore, the PM pole employs the same pole shoe arc radius as the EE pole.

The PM pole contains for instance two PMs embedded in a V position, see Fig. 3.5. To attach the PM pole to the rotor yoke as shown in Fig. 3.2b, the distance w between the PMs is needed for the bolts, which go through the rotor yoke and the round solid rim. The screws are tightened from the inner side of the round solid rim. The distance w

depends on the stress, which acts upon the bolt as a result of the centrifugal forces. Setting the initial values of w , the PM width can be defined as

$$w_{PM} = \frac{R_r \sin\left(\frac{\alpha_p \pi}{2p}\right) - w}{\cos\left(\frac{\pi}{p}\right)}, \quad (3.14)$$

where R_r is the outer rotor radius and α_p is the pole shoe relative width, which is the same as for the EE pole.

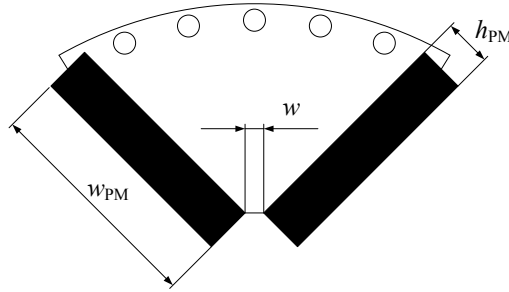


Fig. 3.5: PM pole.

The PM height h_{PM} is determined based on the magnetic circuit of the studied topology operating at no load.

3.1.4 Magnetic circuit

Figure 3.6 presents the magnetic flux paths of an ARC-PMSG with ACL. Because the machine works without electrical excitation at no load, then according to Ampere's law the permanent magnet current linkage at no load over a complete pole pair has to correspond to the magnetomotive force (mmf) of the magnetic circuit as

$$\oint \mathbf{H} \cdot d\mathbf{l} = \Theta_{PM} = H_c h_{PM} = 2U_{m\delta} + 2U_{m_{ds}} + 2U_{m_{dr}} + U_{m_{pEE}} + U_{m_{yr}} + U_{m_{ys}} + U_{m_{PM}}, \quad (3.15)$$

where Θ_{PM} is the PM current linkage, H_c is the PM coercive force, $U_{m\delta}$ is the magnetic voltage of the air gap, $U_{m_{ds}}$ is the magnetic voltage of the stator tooth, $U_{m_{dr}}$ is the magnetic voltage of the rotor tooth, $U_{m_{pEE}}$ is the magnetic voltage of the EE pole, $U_{m_{ys}}$ is the magnetic voltage of the stator yoke, $U_{m_{yr}}$ is the magnetic voltage of the rotor yoke and $U_{m_{PM}}$ is the magnetic voltage of the PM.

The solution for the PM height is

$$h_{PM} = \frac{2U_{m\delta} + 2U_{m\delta s} + 2U_{m\delta r} + U_{mpEE} + U_{myr} + U_{mys}}{H_c - \frac{H_c}{B_r} B_{PM}}, \quad (3.16)$$

where B_r is the PM remanent flux density and B_{PM} is the PM flux density. The PM flux density can be determined from the following expression:

$$\Phi_{PM} = (1 + \sigma)\Phi_{\delta 1} = 2B_{PM}w_{PM}l', \quad (3.17)$$

where σ is the leakage factor, which is equal to the ratio of the leakage flux to the main flux $\sigma = \Phi_{\sigma}/\Phi_{\delta 1}$, and l' is the equivalent machine length. The fundamental peak value of the main flux is

$$\hat{\Phi}_{\delta 1} = \alpha_1 \hat{B}_{1\delta} \tau_p l', \quad (3.18)$$

where $\hat{B}_{1\delta}$ is the fundamental peak value of the air gap flux density and α_1 the saturation factor, which in the case of a sinusoidal flux density gets the value $\alpha_1 = 2/\pi$.

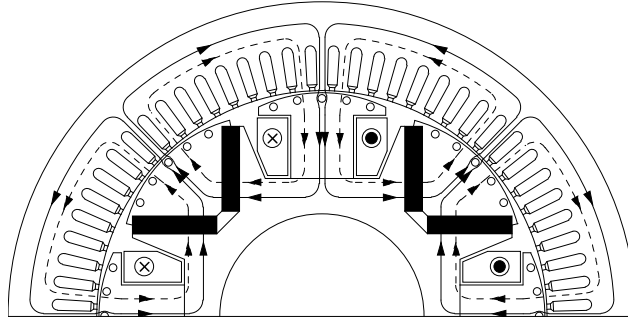


Fig. 3.6: Magnetic flux paths of an ARC-PMSG with ALC.

The solid lines correspond to the PM flux paths, and the dotted lines represent the magnetic flux paths produced by the field coils. At no load, the machine operates without electrical excitation, that is, there is only PM flux.

Since an ARC-PMSG with ACL works at no load without electrical excitation, and taking into account the main constraints, that is, the induced voltage at no load may differ only by 10 % of the rated voltage, the induced voltage at no load is set to $E_{PM} = 1.1$ p.u.

3.1.5 Mechanical consideration

To ensure a proper mounting of PM poles, the distance w between the PMs must be considered from the mechanical point of view.

The centrifugal force F_c acting upon the bolt is

$$F_c = m_{\text{pPM}} \cdot \Omega^2 \cdot R_{\text{av}} = m_{\text{pPM}} \cdot \frac{v^2}{R_{\text{av}}}, \quad (3.19)$$

where m_{pPM} is the mass of a PM pole, which includes the masses of the PMs, the iron core and the damper bars, Ω is the mechanical angular speed, R_{av} is the average radius, which can be equal to the outer rotor radius R_r , and v is the linear velocity.

The stress acting upon the bolt is

$$\sigma = \frac{F_c}{S_b \cdot N_b}, \quad (3.20)$$

where S_b is the cross-sectional area of the bolt and N_b is the number of bolts, which fix the PM pole.

If the calculated stress exceeds the maximum allowable bolt yield strength, the distance w between the PMs must be increased to ensure a proper mounting of the PM poles. Naturally, special form magnets with space for the bolts could also be used, if desired.

It should be kept in mind that the above mechanical calculation is simplified, and it includes only a small part of the calculation process that is related to the considered electromagnetic design. A more thorough mechanical analysis requires a separate study.

3.1.6 Synchronous inductances

In general, the direct-axis L_d and quadrature-axis L_q synchronous inductances are the sums of the corresponding magnetizing inductances L_{md} or L_{mq} and the stator leakage inductance L_{st} .

First, it should be noted that because of the special rotor structure, the ARC-PMSG with ACL has different air gap flux densities along the EE and PM poles, and therefore, the stator winding sees the average value of the flux densities, see Fig. 3.7. Consequently, the fundamental harmonics of the air gap flux densities in the d- and q-axes are

$$\hat{B}_{1d,q} = \frac{\hat{B}_{1d,q\text{PM}} + \hat{B}_{1d,q\text{EE}}}{2}, \quad (3.21)$$

where $\hat{B}_{1d,q\text{PM}}$ are the fundamental harmonics of the air gap flux densities along the PM pole in the d- and q-axes and $\hat{B}_{1d,q\text{EE}}$ are the fundamental harmonics of the air gap flux densities along the EE pole in the d- and q-axes.

The magnetizing flux linkage of a single-phase winding in the d- and q-axes can be expressed as

$$\hat{\Psi}_{\text{md,q}} = k_{\text{wl}} N_s \frac{2}{\pi} \tau_p l' \hat{B}_{1\text{d,q}}. \quad (3.22)$$

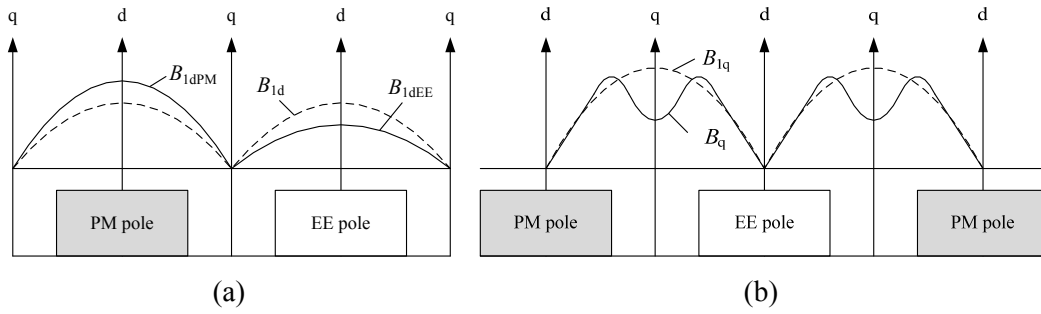


Fig. 3.7: Air gap flux density distributions resulting from the d- and q-axis armature reactions.

(a) Air gap flux density distributions caused by the d-axis armature reaction.

(b) Air gap flux density distributions caused by the q-axis armature reaction.

Notations: $B_{1\text{dPM}}$ are the fundamental harmonics of the air gap flux densities along the PM pole in the d-axes, $B_{1\text{dEE}}$ are the fundamental harmonics of the air gap flux densities along the EE pole in the d-axes and $B_{1\text{d,q}}$ are the fundamental harmonics of the air gap flux densities in the d- and q-axes.

On the other hand, the air gap flux density can be determined by applying the current linkage of the phase $\hat{\Theta}_{1\text{s}}$

$$\hat{B}_{1\text{d,q}} = \frac{\mu_0 \hat{\Theta}_{1\text{s}}}{\delta_{\text{d,qeff}}}, \quad (3.23)$$

where $\delta_{\text{d,qeff}}$ are the effective air gap lengths in the d- and q-axes.

Since the stator current linkage depends on the stator winding parameters, it can be concluded that the behaviour of the air gap flux densities in the d- and q-axes comes from the effective air gap lengths in the corresponding axes. Thus, the effective air gap lengths can be defined as

$$\delta_{\text{d,qeff}} = \frac{\delta_{\text{d,qeffEE}} + \delta_{\text{d,qeffPM}}}{2}, \quad (3.24)$$

where $\delta_{\text{d,qeffEE}}$ are the effective air gap lengths in the d- and q-axes along the EE pole and $\delta_{\text{d,qeffPM}}$ are the effective air gap lengths in the d- and q-axes along the PM pole.

The d-axis effective air gap length along the EE pole consists of the air gap length above this pole and the effect of iron. As the EE pole shoe is cut to produce a sinusoidal air gap flux density, then

$$\delta_{\text{defEE}} = \frac{4}{\pi} k_C \delta' + k_{\text{sat}} k_C \delta', \quad (3.25)$$

where the coefficient k_{sat} takes into account the effect of iron

$$k_{\text{sat}} = \frac{2\hat{U}_{\text{mds}} + 2\hat{U}_{\text{mdr}} + \hat{U}_{\text{mpEl}} + \hat{U}_{\text{mys}} + \hat{U}_{\text{myr}}}{\hat{U}_{\text{mPM}} + \hat{U}_{\text{m}\delta\delta}}. \quad (3.26)$$

The d-axis effective air gap length along the PM pole comprises the air gap length above this pole, the PM height h_{PM} and the effect of iron. The PM pole has the same pole shoe form as the EE pole, and therefore

$$\delta_{\text{defPM}} = \frac{4}{\pi} k_C \delta' + h_{\text{PM}} + k_{\text{sat}} k_C \delta'. \quad (3.27)$$

Inserting Eqs. (3.25) and (3.27) into Eq. (3.24) gives the expression for the d-axis effective air gap

$$\delta_{\text{def}} = \frac{2}{\pi} k_C \delta' + \frac{h_{\text{PM}}}{2} + k_{\text{sat}} k_C \delta'. \quad (3.28)$$

The q-axis armature reaction flux does not pass the PMs but bypasses them. It goes along the rotor pole shoes mostly above the PMs. Since both the EE and PM poles have almost the same pole shoe widths, δ_{qeffEE} and δ_{qeffPM} are almost the same. The effective air gap in the q-axis with an air gap producing sinusoidal air gap no-load flux density can be determined for example according to (Heikkilä, 2002)

$$\delta_{\text{qeff}} = \frac{3\pi k_C \delta'}{4 \sin\left(\frac{\alpha_p \pi}{2}\right)^2} k_{\text{sat}} k_C \delta'. \quad (3.29)$$

Inserting Eqs. (3.28) and (3.29) into Eq. (1.2) results in L_{md} and L_{mq} .

3.1.7 No-load characteristic

The no-load characteristic $E_0 = f(\Theta_0)$ is defined based on the magnetic circuit calculation by varying the induced phase voltage. Figure 3.8 presents an example of the no-load characteristic in p.u., which is defined at five different values of E_0 . Because the HESG with ACL at no load works without excitation current, the initial point of its no-

load characteristic corresponds to the PM-induced phase voltage, whereas in traditional SGs it is a zero point. The no-load curve below E_{PM} is assumed to be linear with the slope of E_{PM}/Θ_{PM} .

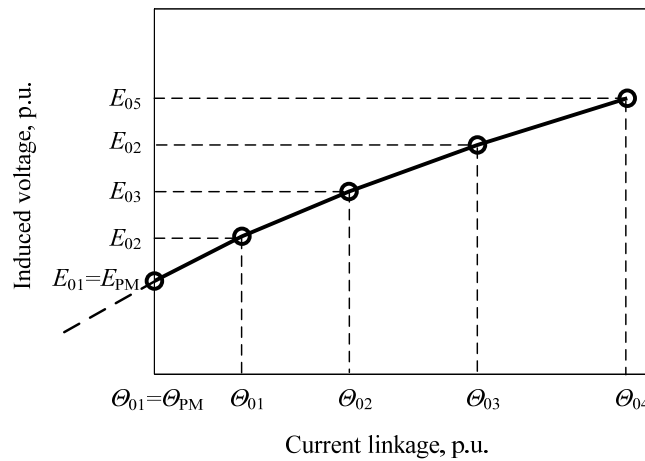


Fig. 3.8: No-load characteristic of the HESG with ACL.

3.1.8 Phasor diagram

As the voltage U_s , the current I_s , the power factor $\cos \varphi$ and the synchronous inductances L_d, L_q are known, the total induced voltage E_{PM+f} in the rated point can be determined from a phasor diagram. Figure 3.9 provides a phasor diagram of an ARC-PMSG with ACL, where the stator resistance is neglected.

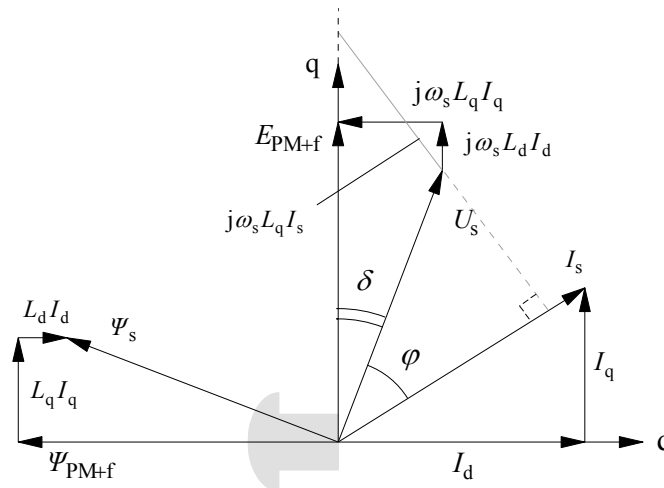


Fig. 3.9: Phasor diagram of the HESG with ALC.

The q-axis in the phasor diagram can be found by adding $j\omega_s L_q I_s$ to the stator voltage U_s . Further, the total induced voltage E_{PM+f} is determined by adding the armature reaction to the stator voltage U_s :

$$E_{PM+f} = U_s + j\omega_s L_d I_d + j\omega_s L_q I_q. \quad (3.30)$$

3.1.9 Compensating winding

In the series HESM, the total current linkage Θ_{PM+f} can be expressed as the sum of the excitation current linkage Θ_f and the PM current linkage $\Theta_{PM} = H_c h_{PM}$. Therefore, the desired excitation current linkage Θ_f is the difference between the total current linkage Θ_{PM+f} which corresponds to E_{PM+f} in the no-load characteristic and Θ_{PM} .

The cross-sectional area of the excitation winding conductor S_f is

$$S_f = \frac{\rho_f l_{fav} p \Theta_f}{U_f}, \quad (3.31)$$

where ρ_f is the resistivity of the material, U_f is the excitation voltage and l_{avf} is the average coil turn length, which can be expressed as in (Sergeev, 1969)

$$l_{fav} = 2(l_m + b_m) + 0.25. \quad (3.32)$$

The excitation current I_f in the rated point is a product of the cross-sectional area S_f and the excitation current density J_f in rated operation. The number of excitation winding turns N_f is

$$N_f = \frac{\Theta_f}{I_f} = \frac{\Theta_f}{S_f j_f}. \quad (3.33)$$

3.1.10 Machine parameters

To study the transient and steady states of the SMs, the machine parameters are required. The machine parameters of the SMs mainly contain resistances and inductances of

- stator winding;
- field/compensating winding and
- damper winding.

Based on the parameters of the above windings, it is possible to calculate the corresponding time constants and the transient and subtransient parameters.

The resistance of the series-connected compensating winding of an ARC-PMSG with ACL can be expressed as

$$R_f = \frac{\rho_f p N_f I_{fav}}{S_f}. \quad (3.34)$$

The leakage inductance of the compensating winding $L_{f\sigma}$ is determined as the difference between the compensating winding L_f and the magnetizing inductances L_{md} , where L_f can be calculated for instance according to the empirical equation presented in (Sergeev, 1969)

$$\underline{L}_f = 1.27 k_d \underline{L}_{md} \left[1 + \frac{2\Theta_{PM} I_m \lambda_f}{\Phi_{\delta 1} 10^8 0.4\pi} \right], \quad (3.35)$$

where λ_f is the field winding leakage permeance and k_d is the d-axis armature reaction coefficient, which can be obtained for example according to (Balagurov, 1982)

$$k_d = 0.78 + 0.25(1 - \alpha_p)(1 - \beta_0) + 0.01\gamma_0, \quad (3.36)$$

where $\beta_0 = \delta_0 / \tau_p$ is the ratio between the minimum air gap length δ_0 and the pole pitch τ_p , and $\gamma_0 = \delta_{max} / \delta_0$ is the ratio between the maximum (at the edge of the pole shoe) δ_{max} and minimum δ_0 air gap lengths.

The field winding leakage permeance λ_f is expressed as the sum of the following permeances:

$$\lambda_f = \lambda_p + 0.654\lambda_m + 0.377\lambda_{mf}. \quad (3.37)$$

The required permeances are calculated in the following way:

$$\lambda_p = \left[1.4 \left(\frac{d_t}{C_p} - 0.25 \right) + 0.55 \left(\frac{a_p}{C_p} + 0.2 \right) - 0.4 \left(\frac{a_p}{C_p} - 0.5 \right)^2 \right] 0.4\pi, \quad (3.38)$$

$$\lambda_m = \frac{0.4\pi 0.55 h_m}{\tau_p - b_m - (\pi/2p)(h_m + 2h_p + 2\delta_0)}, \quad (3.39)$$

$$\lambda_{mf} = \frac{0.37 b_m 0.4\pi}{l_m}, \quad (3.40)$$

where $a_p = (b_p - b_m) / 2$, $d_t = h_p + \delta_0 - b_p^2 / (4D_s)$ and $C_p = \tau_p - b_p - \pi d_t / p$. If $d_t / C_p < 0.25$, the first component in Eq. (3.38) must be neglected.

(Danilevich et al., 1965) suggest to calculate the direct R_D and quadrature R_Q damper winding resistances according to the following empirical equations:

$$\underline{R}_D = \frac{3.55 \cdot 10^{-6} \Theta_{s1}}{f \Phi_{\delta 1}} \left(\frac{C_c I_c}{S_r N_r} + \frac{0.13 \tau_p C_{ring}}{S_{sc}} \right), \quad (3.41)$$

$$\underline{R}_Q = \frac{2.66 \cdot 10^{-6} \Theta_{s1}}{f \Phi_{\delta 1}} \left(\frac{C_c I_c}{S_r N_r} + \frac{0.25 \tau_p C_{ring}}{S_{sc}} \right), \quad (3.42)$$

where Θ_{s1} is the fundamental component of the stator current linkage, C_c is the ratio of the resistivity of the damper winding bar to the copper resistivity and C_{ring} is the ratio of the resistivity of the short-circuit ring to the copper resistivity. If the material of the damper winding is copper, then $C_c = C_{ring} = 1$, and if the winding is made of brass, then $C_c = C_{ring} = 4$.

The fundamental component of the stator current linkage is

$$\hat{\Theta}_{s1} = \frac{\sqrt{2}}{\pi} m \frac{N_{ph} k_{wl} I_s}{p}. \quad (3.43)$$

Following (Danilevich et al., 1965), the damper winding leakage inductances in the direct $L_{D\sigma}$ and quadrature $L_{Q\sigma}$ axes are:

$$\underline{L}_{D\sigma} = 4\mu_0 \frac{\Theta_{s1}}{\Phi_{\delta 1}} \left[\frac{l_p \left(1.7 + 2.8 \frac{h_r}{b_r} \right)}{N_r} + \frac{\tau_p}{2\pi} \right], \quad (3.44)$$

$$\underline{L}_{Q\sigma} = 0.75 \underline{L}_{D\sigma}. \quad (3.45)$$

3.2 Thermal analysis

One of the main drawbacks of the NdFeB magnets is the sensitivity to the temperature change, in other words, when the temperature increases, the magnet properties deteriorate. In the studied ARC-PMSG with ACL, the PMs are close to the compensating winding, which is one of the main sources of the heat flow. Therefore, special attention must be paid to the thermal analysis of the ARC-PMSG with ACL.

The fundamentals of heat transfer are discussed for example in (Poole and Sarvar, 1989). The general method for the thermal evaluation of electrical machines is the

thermal network model (Mellor et al., 1991; Liu et al., 1993; Kylander, 1995; Saari, 1995). The thermal analysis applying this model is based on dividing the studied machine into several simple components, such as frame, yoke, stator tooth, stator coils, stator end-windings, air gap, rotor pole, rotor coils, rotor end-windings, magnets and rotor yoke. All of these components are represented by thermal resistances connected with nodes. Each node is coupled with the neighbours by radial and axial conduction and convection resistances. In the presented thermal model, the heat flows propagate only in the radial and axial directions.

Because of the symmetricity of the ARC-PMSG, it suffices to consider only one-eighth of the machine, see Fig. 3.10.

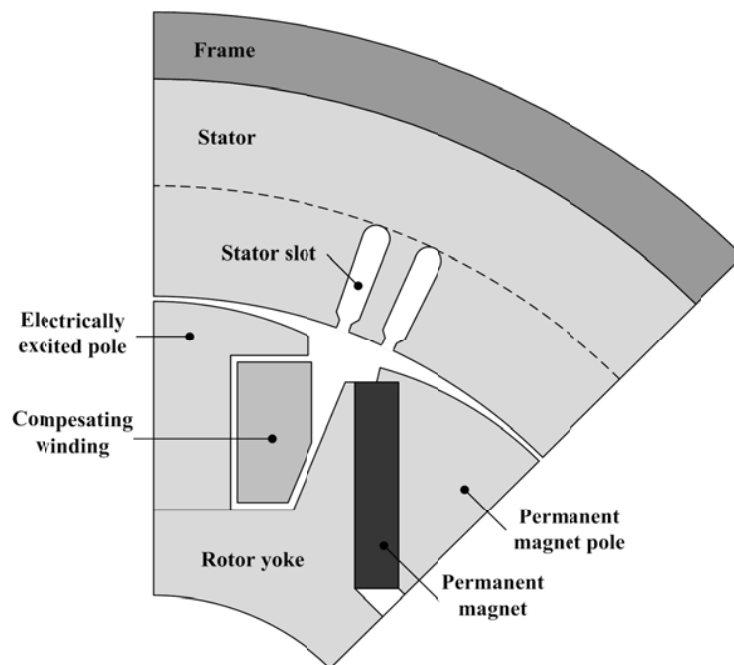


Fig. 3.10: Part of the ARC-PMSG with ACL considered in the thermal analysis.

Figure 3.11 and Figure 3.12 present the thermal networks in the radial and axial directions, taking into account the simplified geometry of the ARC-PMSG with ACL. The combination of these both thermal networks gives the equivalent thermal network for the ARC-PMSG with ACL, see Fig. 3.13. The definitions of the thermal resistances and definitions of the node numbers are given in Appendix B.1 and Appendix B.2, respectively.

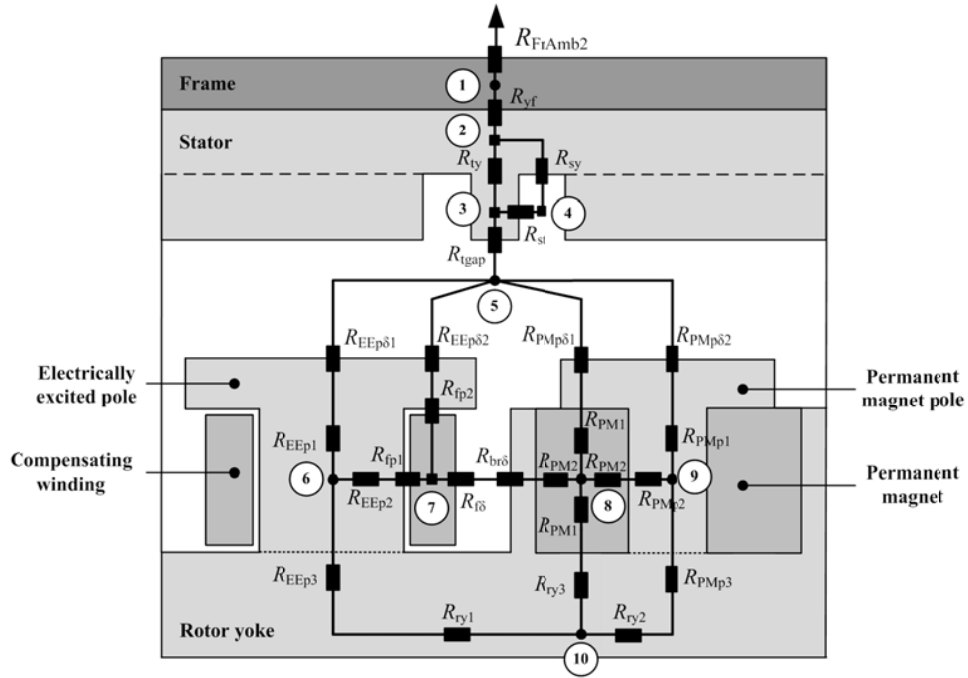


Fig. 3.11: Thermal network for the ARC-PMSG with ACL in the radial direction. The solid squares indicate the heat sources, and the solid circles correspond to the intersections of the heat flows.

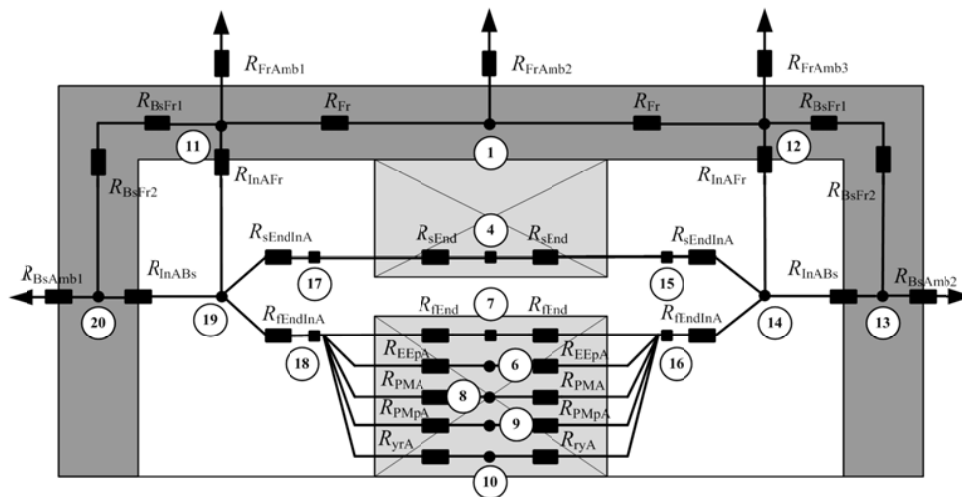


Fig. 3.12: Thermal network for the ARC-PMSG with ACL in the axial direction. The solid squares indicate the heat sources, and the solid circles correspond to the intersections of the heat flows.

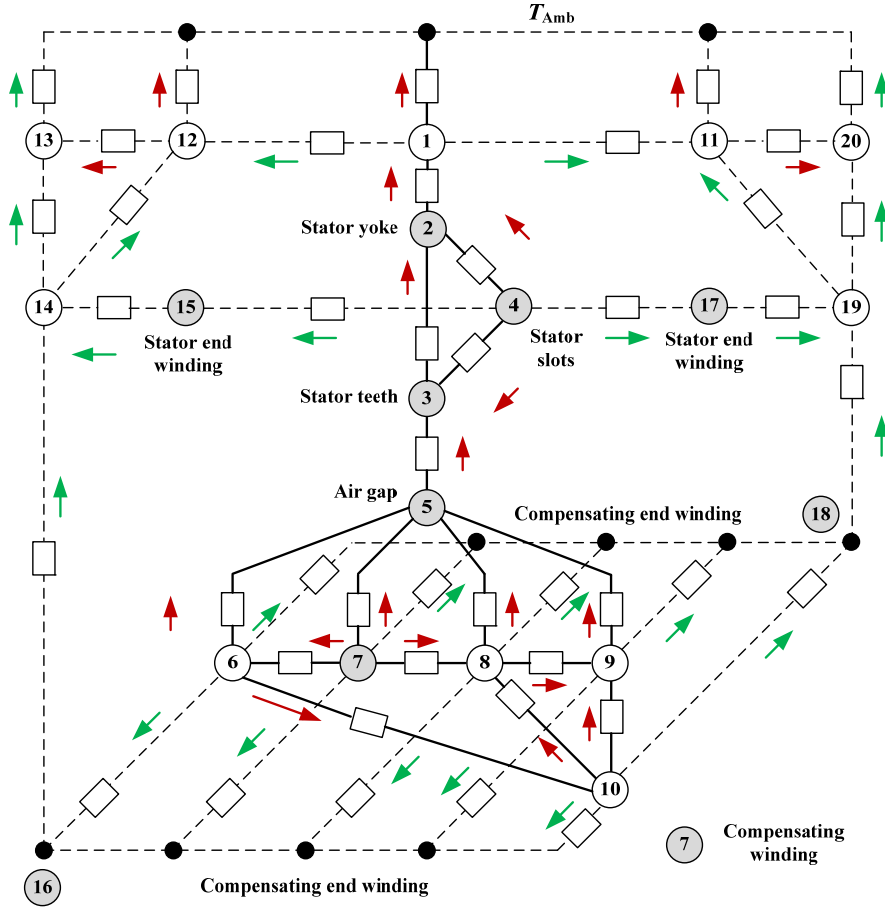


Fig. 3.13: Equivalent thermal network of an ARC-PMSG with ARC. The grey nodes depict the places where the machine losses are concentrated. The green arrows refer to the heat flow in the axial direction, and the red ones correspond to the radial direction of the heat flow.

The thermal resistances depicted in Figs. 3.11–3.13 are the convection and conduction resistances of the components, which are defined by the following equations:

$$R_{\text{conduction}} = \frac{l_i}{\lambda A_i}, \tag{3.46}$$

$$R_{\text{convection}} = \frac{1}{\alpha A_i}, \tag{3.47}$$

where l_i is the length of the body in the heat flow direction, A_i is the cross-sectional area, λ is the thermal conductivity and α is the convection coefficient. The coefficients λ and α can be obtained for example according to (Nerg et al., 2008).

To establish a system of equations where the temperatures are unknown, two laws are needed. The first one is the first Kirchhoff's law, where the sum of the heat flows into a node is equal to the sum of the heat flows out of the node. The second law is the Fourier equation stating that the heat always flows from a hotter body to a colder body:

$$t_1^o - t_2^o = Q_{12} R_{12}, \quad (3.48)$$

where t_1^o and t_2^o are the temperature in nodes 1 and 2, respectively, Q_{12} is the heat flow between nodes 1 and 2, and R_{12} is the thermal resistance between these nodes.

The desired temperatures in the steady state are calculated by solving the following matrix equation

$$\Delta \mathbf{T} = \mathbf{G}^{-1} \mathbf{P}, \quad (3.49)$$

where $\Delta \mathbf{T}$ is the temperature rise vector, \mathbf{P} is the single-row power loss matrix containing the losses in each node, and \mathbf{G} is the thermal conductance square matrix defined based on the thermal resistances shown in Fig. 3.13

$$\mathbf{G} = \begin{bmatrix} \sum_{i=1}^n R_{1,i}^{-1} & \cdots & -R_{1,n}^{-1} \\ \vdots & \ddots & \vdots \\ -R_{n,1}^{-1} & \cdots & \sum_{i=1}^n R_{n,i}^{-1} \end{bmatrix}. \quad (3.50)$$

3.3 Summary

This chapter addressed the analytical calculation for the design of the studied ARC-PMSG with ACL. Nowadays, analytical design guidelines for the traditional electrical machines are based on the experimental data gathered from different actual machines. Therefore, they give relatively reliable results. Based on this and the fact that the ARC-PMSG with ACL inherently represents a combination of the EESG and the PMSG, the presented electromagnetic design of the machine relies on a combination of the guidelines for the analytical calculation of the EESG and the PMSG. The simplified thermal analysis was made mainly to check the average temperature in the PMs. Since the PMs are placed close to the compensating winding, the proposed topology can be criticized for the performance of the PMs, which are quite sensitive to the temperature rise. A detailed thermal analysis requires a separate thorough study of the topic.

The proposed ARC-PMSG with ACL has not yet been used for commercial purposes. Thus, the presented analytical design is the first effort into the analytical estimation of the machine performance, which must be confirmed by numerical calculation and experimental measurements. The next two chapters consider the test machine that was built to verify the design of the studied ARC-PMSG with ACL.

4 Test machine

This chapter addresses the test machine of the ARC-PMSG with ACL. The main targets of the test machine are: to verify the developed electromagnetic design presented in the previous chapter by a finite element analysis (FEA), and to build a prototype to carry out the experimental measurements. The design requirements and main dimensions of the test machine are presented. The results of the analytical calculation given in the previous chapter and the FEA results are compared. The experimental prototype is discussed.

4.1 Design requirements

Since the stator of an ARC-PMSG with ACL is the same as for a conventional AC machine, it was decided to use the already existing stator and perform only the rotor design. The stator of the test machine originally belongs to an induction machine with 69 kVA apparent power. The stator carries a three-phase single-layer full-pitched winding with three slots per pole and phase and four pole pairs. The rated voltage and frequency of the induction machine are 660 V and 50 Hz. The air gap diameter and length of the stator are 330 mm and 310 mm, respectively. By adding the main constraints (see Table 1.2) to the induction machine parameters, Table 4.1 presents the design requirements of the test machine.

Table 4.1: Design requirements of the test machine.

Parameter	Value	Unit
Phase number, m	3	-
Apparent power, S_n	69	kVA
Nominal line-to-line voltage, U_n	660	V
Frequency, f	50	Hz
Power factor, $\cos \varphi$	0.8 _{ind}	-
Short-circuit current, I_{sc}	$3I_n$	-
Air gap diameter, D_s	330	mm
Length, l	310	mm
Number of slots per phase and pole, q	3	-

4.2 Main dimensions

Based on the electromagnetic design discussed in the previous chapter and the FEA given below, a rotor of the test machine that satisfies the design requirements was designed, see Fig. 4.1. The stator winding concept of the test machine is given in Appendix C.1. The main geometry data of the test machine are provided in Table 4.2.

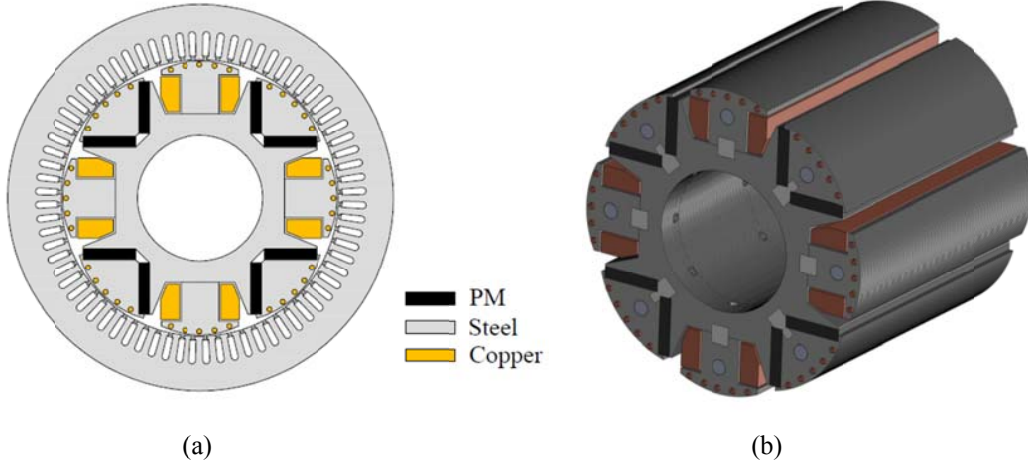


Fig. 4.1: Designed test machine with 69 kVA apparent power.

(a) Cross-sectional view.

(b) Rotor 3D view.

Table 4.2: Main geometry data of the test machine.

Parameter	Value	Unit
Outer stator diameter, D_{out}	460	mm
Air gap diameter, D_s	330	mm
Shaft diameter, D_{in}	150	mm
Active length, l	310	mm
Air gap length, δ	1.5	mm
Number of stator slots, Q_s	72	-
Number of slots per phase and per pole, q	3	-
Number of phase turns, N_{ph}	81	-
Number of parallel paths, a	4	-
Number of PMs per pole	2	-
Number of compensating winding turns per pole, N_f	90	-

4.3 Finite element analysis

A 2D time stepping FEA were performed applying the Flux-2D software package by Cedrat Ltd. The 2D FEA model includes some simplifications. The actual stator or rotor end winding are not modelled. Only the values of the end winding inductances are included in the circuit model. The end-winding inductances calculated based on (Pyrhönen et al., 2008) are equal to $6.9 \cdot 10^{-5}$ H. The damper winding bars were modelled as solid conductors, which are short-circuited at the machine ends. The compensating winding was modelled as a stranded coil conductor with the imposed current. Because of the test machine symmetry, only a quarter of the cross-sectional view is modelled,

which in turn decreases the calculation time.

Figure 4.2 shows the flux lines and the flux density plot at no load. It can be seen that the flux densities in the teeth, the stator and rotor yokes and the poles do not exceed critical values.

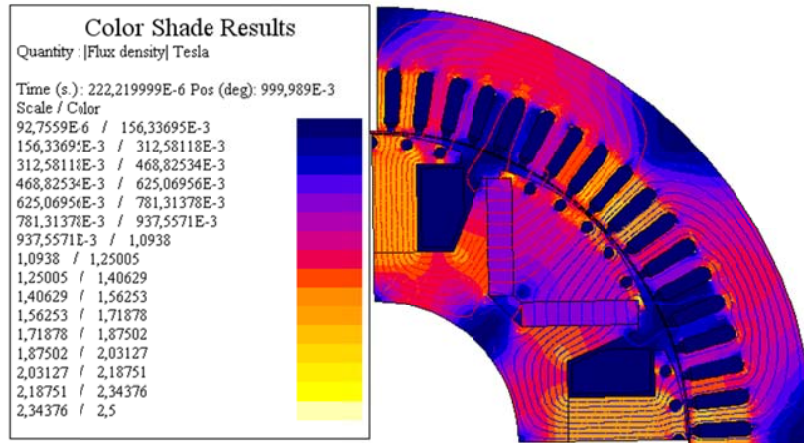


Fig. 4.2: Flux lines and the flux density plot at no load.

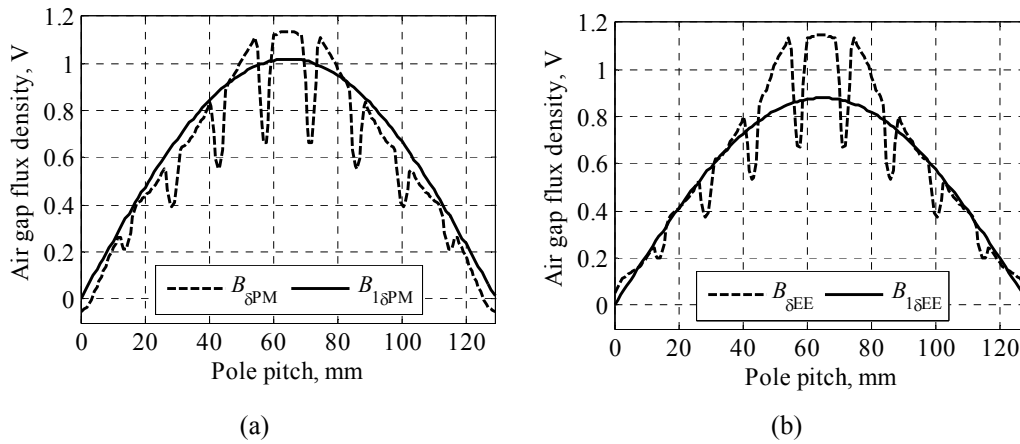


Fig. 4.3: No-load air gap flux density distributions of the ARC-PMSG with ACL.

(a) Air gap flux density distribution across the PM pole. The fundamental peak component is $B_{1\delta PM} = 1.02$ T.

(b) Air gap flux density distribution across the EE pole. The fundamental peak component is $B_{1\delta EE} = 0.88$ T.

The fundamental peak component of the air gap flux density across one pole pair pitch $B_{1\delta}$ is the average value of $B_{1\delta PM}$ and $B_{1\delta EE}$, that is, $B_{1\delta} = 0.95$ T.

The no-load air gap flux density distributions across different poles are presented in Fig. 4.3. The fundamental peak value of the air gap flux density across one pole pair pitch is 0.95 T. To obtain the desired air gap flux density, the PM width/height must be 62/13 mm. The analytical calculation gives the PM width/height of 64/12 mm, which shows quite a good agreement with the FEA.

Figure 4.4 demonstrates the no-load PM-induced phase voltage waveform distribution and its harmonic content. In general, the voltage waveform distributions of synchronous generators have to be close to a sinusoidal one. The fulfilment of this requirement can be estimated for example by an index term called the total harmonic distortion (THD), which can be expressed as:

$$\text{THD} = \frac{100}{U_1} \sqrt{\sum_{v=2}^{\infty} U_v^2}, \quad (4.1)$$

where U_1 is the RMS or peak voltage of the fundamental harmonic and U_v is the RMS or peak voltage of the v^{th} harmonic.

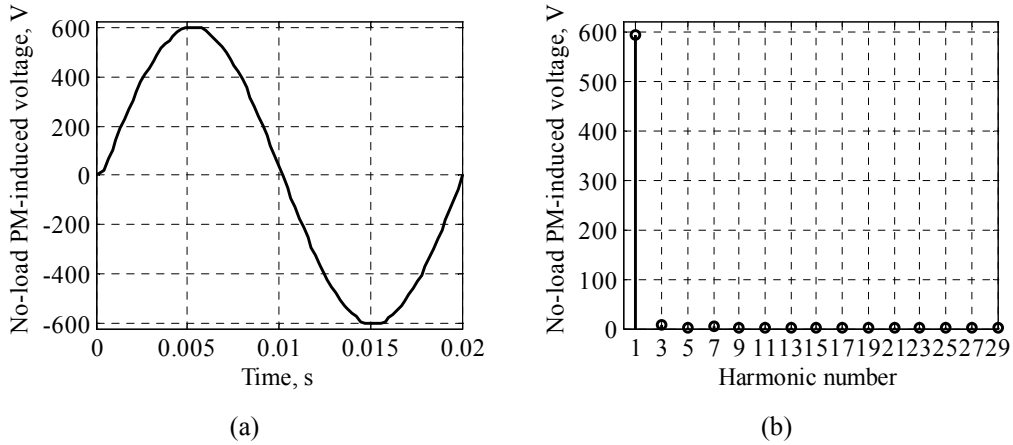


Fig. 4.4: No-load PM-induced phase voltage and its harmonic content.

(a) No-load PM-induced phase voltage waveform distribution.

(b) Harmonic content of the no-load PM-induced phase voltage waveform distribution ($E_{PM,1}=596.8$ V, $E_{PM,3}=6.1$ V, $E_{PM,5}=2.7$ V, $E_{PM,7}=3.9$ V, $E_{PM,9}=1.7$ V, $E_{PM,11}=0.4$ V, $E_{PM,13}=1.1$ V, $E_{PM,15}=1.2$ V, $E_{PM,17}=2.4$ V, $E_{PM,19}=1.4$ V, $E_{PM,21}=1$ V, $E_{PM,23}=1$ V, $E_{PM,25}=0.5$ V, $E_{PM,27}=0.6$ V, $E_{PM,29}=0.5$ V).

Based on the FEA, the THD of the no-load PM-induced phase voltage is 1.4 %, which demonstrates an almost sinusoidal waveform.

Calculation of the magnetizing inductances is carried out as for the PM machine by the flux linkages determined by the Flux-2D for the direct and quadrature axis. To define the d- and q-axes of the test machine, as shown in Fig. 4.5, the rotor is rotated with the

PMs modelled as air. The phase U of the stator winding is injected by a maximum current amplitude. The currents in the phases V and W are opposite and equal to half of the maximum magnitude injected in the phase U.

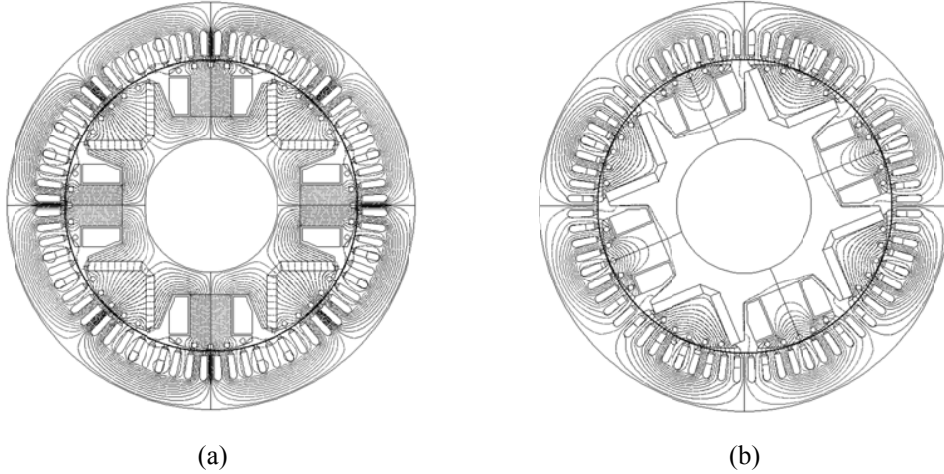


Fig. 4.5: Flux lines in the direct- and quadrature-axis positions.

(a) Direct-axis.

(b) Quadrature-axis.

It is seen that the quadrature armature reaction is strong, and it may be necessary to restrict it in high-stress machines with different rotor constructions.

In the case of determining the d-axis magnetizing inductance, the PMs were included in the calculations, in other words, they were not modelled as air. In order to determine the d-axis magnetizing inductance L_{md} , the FEA is carried out in two steps (Tapia, 2002). First, no current is applied to the phase winding so that the fundamental harmonic of the air gap flux density produced by the PMs, $B_{\delta 1PM}$, is solved. In the second step, the effect of the armature reaction is added by feeding the phase coils to produce negative current in the direct-axis position. The negative current is demagnetizing the flux in the air gap. The fundamental harmonic of the total air gap flux density contributed both by the PM and the armature flux, $B_{\delta 1tot}$, is then calculated. The d-axis magnetizing inductance L_{md} is determined from the magnetic flux difference of these two magnetic flux fundamental solutions:

$$L_{md} = \frac{\Delta \hat{\Psi}_{d1}}{\Delta \hat{I}_s} = \frac{k_{w1} N_{ph} \Delta \hat{\Phi}_{\delta 1}}{\Delta \hat{I}_s} = \frac{k_{w1} N_{ph} (\hat{\Phi}_{\delta 1, PM} - \hat{\Phi}_{\delta 1, tot})}{\hat{I}_s}, \quad (4.2)$$

where $k_{w1} N_{ph}$ is the effective number of turns in series per stator winding, \hat{I}_s is the peak value of the stator current, $\hat{\Phi}_{\delta 1PM} = \frac{2}{\pi} \hat{B}_{\delta 1, PM} \tau_p l'$ is the peak of the air gap flux per pole

pitch caused by the PMs in the direct axis and $\hat{\Phi}_{\delta 1P, \text{tot}} = \frac{2}{\pi} \hat{B}_{\delta 1, \text{tot}} \tau_p l'$ is the peak of the air gap flux per pole pitch contributed both by the PM and the armature flux in the direct axis.

Since the magnetic flux in the quadrature axis does not pass the magnets, they are modelled as vacuum in the quadrature axis. The magnetizing inductance is calculated from the air gap flux density, which is caused by the stator current only:

$$L_{mq} = \frac{\hat{\Psi}_{q1}}{\hat{I}_s} = \frac{k_{w1} N_{ph} \hat{\Phi}_{\delta 1}}{\hat{I}_s}, \quad (4.3)$$

where $\hat{\Phi}_{\delta 1} = \frac{2}{\pi} \hat{B}_{\delta 1} \tau_p l'$ is the peak air gap flux per pole pitch caused by the stator current in the q-axis.

The comparison of the magnetizing inductances from the analytical and numerical calculations given in Table 4.3 gives tolerable errors, which give a good agreement between the analytical calculations and the FEA.

Table 4.3: Comparison of the calculated magnetizing inductances.

Parameter	Analytical	FEA	Error
d-axis magnetizing inductance, L_{md}	6.38 mH 0.32 p.u.	7.05 mH 0.35 p.u.	8.6 %
q-axis magnetizing inductance, L_{mq}	9.69 mH 0.48 p.u.	9.56 mH 0.47 p.u.	2.1 %

Besides the achievement of the three-phase short circuit requirement, the ARC-PMSG has to withstand the demagnetization risk of the PMs. In the case of a short circuit there is a risk of irreversible demagnetization of the magnets (parts) caused by the strong opposing armature reaction at the beginning of the short circuit when the peak of the stator current is high enough. The low direct-axis synchronous inductance and the presence of a damper winding result in the low direct-axis subtransient inductance, and therefore, the first peak of the short-circuit current tends to be large.

Unfortunately, in addition to the three-phase short circuit, a generator can suffer from two-phase or single-phase short circuits, which also expose the PMs to the demagnetization risk at the first peak of the short-circuit current. A single-phase short circuit is a short circuit of the grounded neutral, star-point-coupled cable with one of the stator winding phases. Two-phase and three-phase short circuits can occur as a result of a fault at the terminals of the generator or because of a damage in the cable connecting the generator with the load.

The magnets can be protected by selecting the generator geometry and the magnet grade carefully, which means choosing grades with the knee in the BH curve in the 3rd quadrant. This, however, leads to an increase in the PM price. The properties of the PM material used in this analysis are given in Appendix C.2. As it was mentioned above, the damper winding protects the magnets during a short circuit by not letting the armature fields to immediately penetrate the rotor.

To observe the short-circuit endurance of the test machine, single-phase, two-phase and three-phase short-circuit tests are performed. The electrical circuits of the corresponding short circuits are depicted in Appendix C3. All the short circuits are applied in two conditions: 1) at no load when the compensating current is equal to zero, and 2) at rated load, that is, $P = P_n$, $U_s = U_n$, $\cos \varphi = 0.8_{ind}$, where the compensating current equals its rated value. The short-circuiting of all three phases is carried out at a moment when one of the line-to-line voltages changes its sign. This time period results in the highest first peak in the short-circuit current in that particular phase (Rilla, 2012).

Figure 4.6 and Figure 4.7 demonstrate the short-circuit currents as a function of time when the short circuit is applied in no-load and rated load conditions, correspondingly. The single-phase short circuit gives the highest first peak in the short-circuit current in no-load and rated load conditions. Again, the two-phase short circuit gives lower peaks in the stator currents in both conditions.

The short-circuit endurance is analysed based on the normal components of the magnetic flux densities along the paths 1–4 shown in Fig. 4.8 at a moment when the first high peak of the short-circuit current takes place. Table 4.4 presents the results of the flux densities along paths 1–4.

Table 4.4: Normal component of the magnetic flux densities along paths 1–4 when the short circuit is applied in no-load and rated load conditions.

Parameter	Short circuit	Path 1	Path 2	Path 3	Path 4
Short circuits are applied at no load condition					
Normal component of the magnetic flux density along paths 1–4, T	Single-phase	0.49	0.5	0.5	0.5
	Two-phase	0.4	0.41	0.41	0.41
	Three-phase	0.34	0.35	0.35	0.36
Short circuits are applied in rated load condition.					
Normal component of the magnetic flux density along paths 1–4, T	Single-phase	0.45	0.46	0.46	0.46
	Two-phase	0.32	0.35	0.37	0.38
	Three-phase	0.77	0.78	0.78	0.78

As it can be seen in Table 4.4, the three-phase short circuit is the most dangerous when applied at no load, while the two-phase short circuit is more critical than the two other ones when the short circuit is applied at the rated load. The results of the short-circuit

tests reveal that the test machine can tolerate short circuits because the critical knee point of the BH curve of the magnet at 100°C is lower than 0.3 T. It should be noted that the above evaluation was carried out in the worst case, when the short circuit is applied at the terminals of the generator, which is quite rare. Usually, the short circuits occur somewhere close to the generator load. The cables that connect a generator with its load have impedances of their own, which decrease the first high peak of the short-circuit current thereby reducing the demagnetization risk of the PMs.

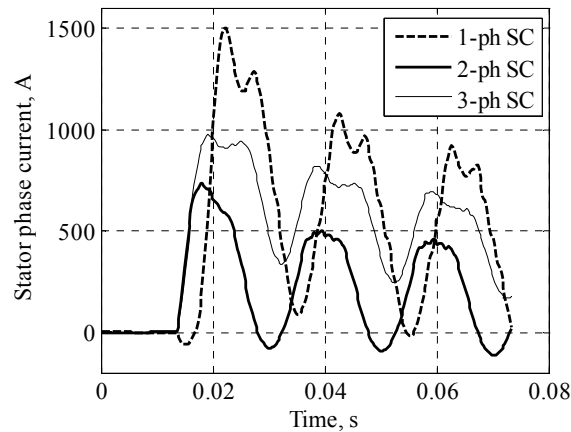


Fig. 4.6: Short-circuit currents as a function of time when the short circuit is applied at no load. The short circuits are initialized at 0.014 s. The first high current peaks at single-phase, two-phase and three-phase short circuits are 1501 A, 737 A and 973 A, respectively.

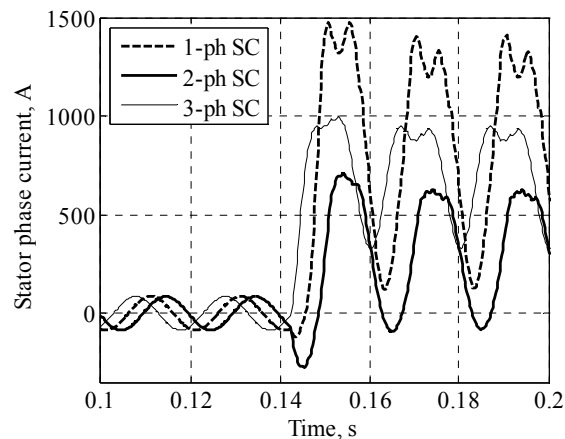


Fig. 4.7: Short-circuit currents as a function of time when the short circuit is applied at the rated load. The short circuits are initialized at 0.143 s. The first high current peaks at single-phase, two-phase and three-phase short circuits are 1473 A, 709 A and 997 A, respectively.

The results of other numerical calculations and their comparison with the analytical and experimental ones are presented in the next chapter.

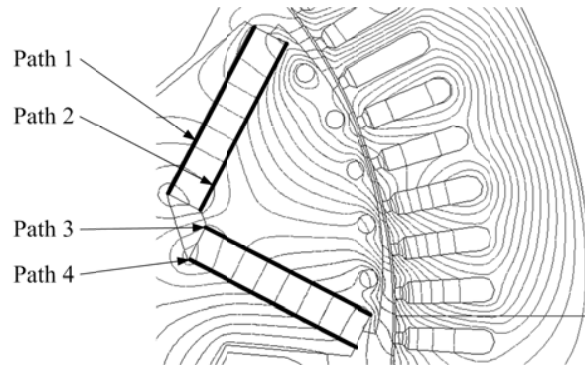


Fig. 4.8: Paths 1–4 along the PM widths.

The normal component of the magnetic flux density is determined along these paths when the first high peak of the short-circuit current occurs.

4.4 Experimental prototype

Based on the analytical calculations and the FEA, the rotor of an experimental prototype of the proposed ARC-PMSG was built. The laminated stator and rotor shown in Fig. 4.9 are made of the electrical steel M600-50A and the construction steel Fe52, respectively. The material of the permanent magnets is Neodymium (NdFeB) 33UH.

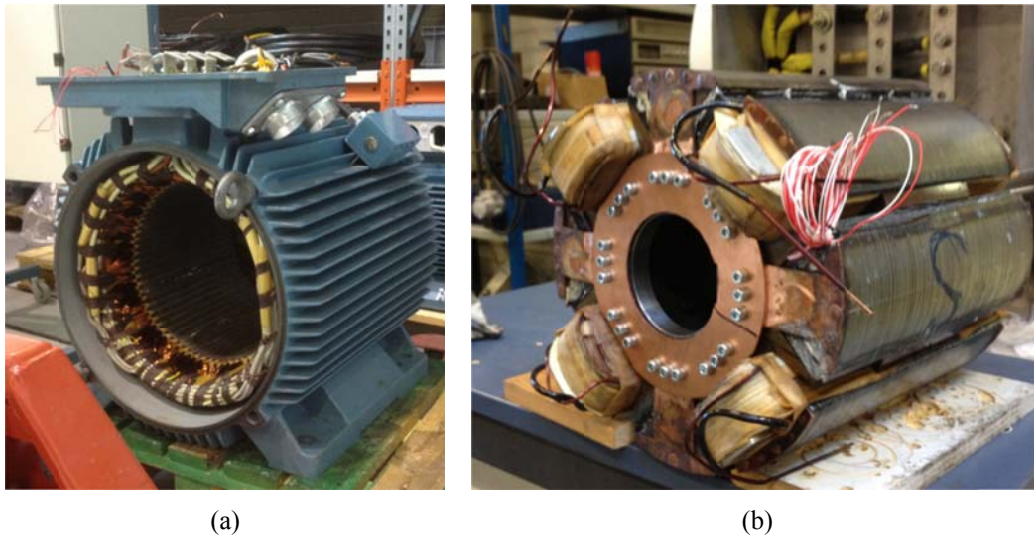


Fig. 4.9: Photos of the stator and rotor parts.

(a) Stator part.

(b) Rotor part.

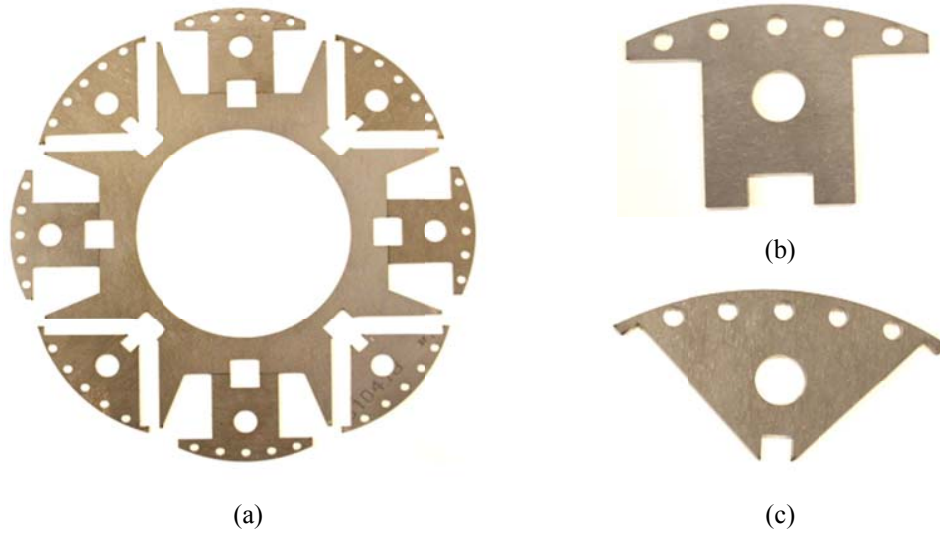


Fig. 4.10: Rotor laminations of the test machine.
 (a) Rotor lamination sheets in the assembled view.
 (b) Electrically excited pole lamination sheet.
 (c) PM pole lamination sheet.

4.5 Summary

To demonstrate the operation principle of the ARC PMSG and verify the predicted analytical electromagnetic design, a down-sized prototype is needed. Therefore, it was decided to design the test machine and then build a prototype of it. In order to reduce the cost of the prototype, the test machine uses the already existing stator that originally belongs to an induction machine of 69 kVA apparent power.

Based on the design requirements, which include the main constraints and dimensions of the stator, the test machine was first pre-designed using the electromagnetic analysis discussed above and then modified in the FEA.

The FEA results give a relatively good correspondence with the analytical calculations of the PM dimensions and magnetizing inductances, which represent the key issues in the design of the rotor of the ARC PMSG.

The short circuits tests carried out in the FEA demonstrate that the test machine has to withstand different short circuit faults in no-load or rated load conditions.

Based on the analytical calculation and the FEA, the prototype of the ARC PMSG was built. The results of the experimental measurements of the test machine as well as the comparison of the experimental results with the analytical and FEA ones are considered in the next chapter.

5 Experimental results

The following subsections present the dynamic and steady-state performance of the 55 kW power test machine. A number of experimental tests presented in Fig. 5.2 were carried out to evaluate the performance of the test machine. The analysis of the machine performance is based on different experimental characteristics and machine parameters considered below. All the experimental tests are based on international standards (IEC 60034-2, 1972; IEC 60034-4, 1985) and (Zherve, 1984; Gurevich et al., 2004) with some modifications resulting from the combination of electrical and permanent magnet excitations.

The laboratory test setup is shown in Fig. 5.1. In the laboratory test, the rotor of the generator was driven by a DC motor with 180 kW power connected with the test machine through a torque transducer. The voltage and current measurements were made at the terminals of the machine, whereas the speed and torque measurements were performed through the torque transducer. The compensating winding was supplied by a stationary DC supply.

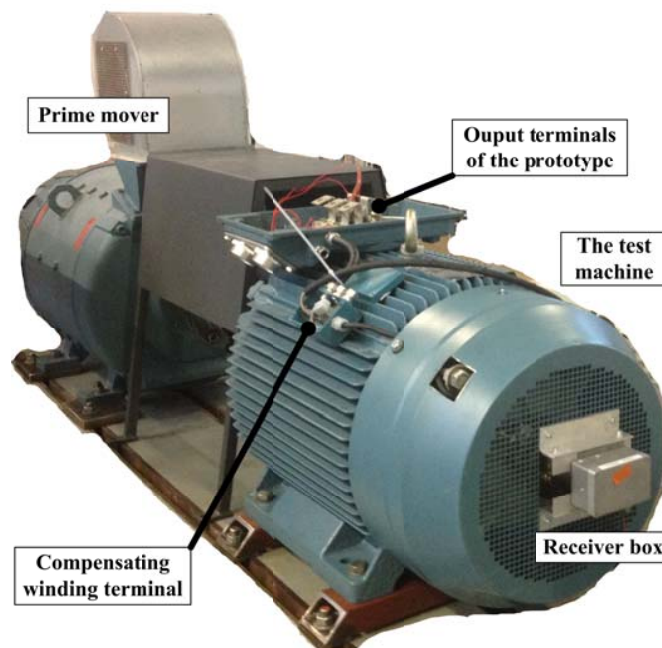


Fig. 5.1: Laboratory test setup for experimental tests. The DC machine with 180 kW power acts as the prime mover. The compensating winding is supplied by a stationary DC supply.

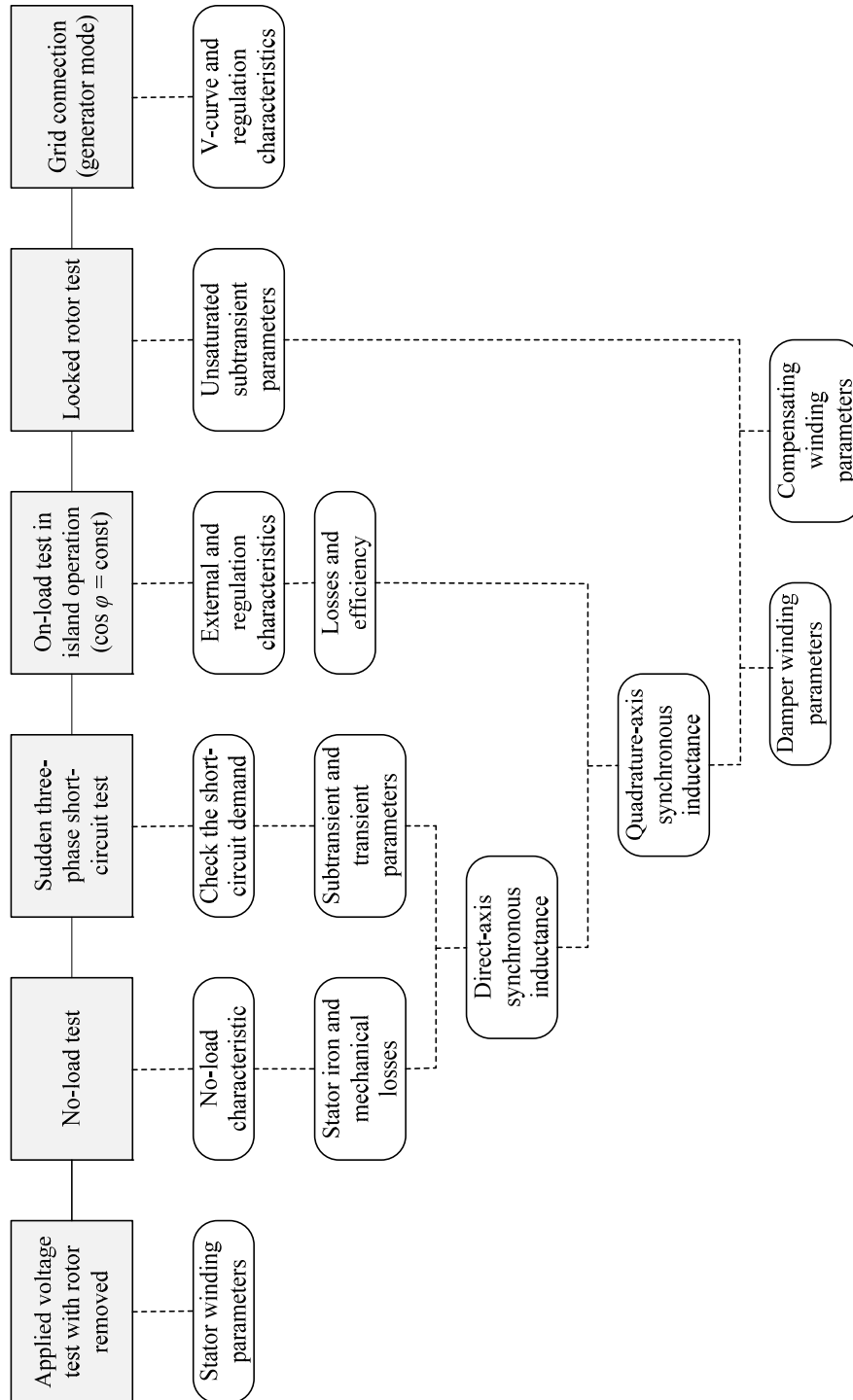


Fig. 5.2: Experimental tests to define the experimental characteristics and the test machine parameters

5.1 Stator winding measurements

The objective of this test is to determine the stator winding resistance R_s and the stator leakage inductance $L_{s\sigma}$, which represent the stator winding parameters. For accurate measurements of the stator winding parameters, the rotor of the test machine has to be removed. The analytical equations for the determination of these parameters can be found for instance in (Boldea, 2006).

The experimental stator phase resistance R_s can be determined for example by supplying the stator winding with a DC current. Since the resistances of all phases are small and almost equal, it is advisable to connect them in series, as shown in Fig. 5.3.

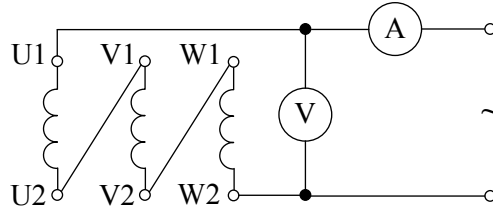


Fig. 5.3: Electrical circuit for the determination of the stator phase resistance.

The stator phase resistance R_0 can then be determined according to Ohm's law as

$$R_0 = \frac{U}{3I}, \quad (5.1)$$

where U and I are the results of the voltmeter and ammeter readings.

The results of the voltmeter and ammeter readings are obtained at ambient temperature of $t_{\text{Amb}}^{\circ} = 20^{\circ}\text{C}$. Usually in operation conditions, the working temperature is higher than the ambient temperature. Therefore, the "cold" stator winding phase resistance R_0 must be referred to the working temperature t_w° . Since the design temperature of the stator is class 130 and the insulation of the stator winding is class 155, the working temperature is $t_w^{\circ} = 75^{\circ}\text{C}$ and the corresponding referred phase resistance R_{75} can be defined as

$$R_{75} = R_0 \frac{235 + t_w^{\circ}}{235 + t_{\text{Amb}}^{\circ}}. \quad (5.2)$$

To determine the stator leakage inductance $L_{s\sigma}$, the stator is supplied from a controllable three-phase voltage source. By controlling the voltage, the stator current is set to its rated value if possible. Despite the missing rotor, the three phase currents produce a rotating field in the stator bore. The stator represents an impedance Z . This impedance consists of the stator winding resistance R_s and the stator winding inductance L_s . The

last component comprises the stator leakage inductance $L_{s\sigma}$ and the inductance L_a , which refers to the field along the active part of the stator in the space where the rotor should be in a normal situation. To extract the effect of the air gap field, a measuring coil is placed over the stator teeth. The length of this coil equals the stator stack length, and the width of the coil is equal to the pole pitch. The end parts of the measuring coil are extended towards the machine centre to exclude the effect of the end winding leakage, as shown in Fig. 5.4. A voltmeter is connected to the measuring coil to measure the induced voltage U_{mc} .



Fig. 5.4: Measuring coil arrangement.

If the search coil consists of N_{mc} turns, the inductance referred to the air gap field can be expressed as

$$L_a = \frac{U_{mc} N_{ph} k_{w1}}{2\pi f_s I_s N_{mc}}, \quad (5.3)$$

where $N_{ph} k_{w1}$ is the effective number of turns in the stator, f_s is the frequency and I_s is the input phase current.

During the test, the applied phase voltage U_s , the input phase current I_s and the input phase power P_{ph} as well as the induced voltage in the measuring coil U_{mc} are measured. Based on these measured results, the stator leakage inductance is

$$L_{s\sigma} = L_s - L_a, \quad (5.4)$$

where

$$\begin{aligned}
L_s &= \frac{\sqrt{Z^2 - R_s^2}}{\omega}, \\
Z &= \frac{U_{\text{ph}}}{I_{\text{ph}}}, \\
R_s &\approx \frac{P}{3I_{\text{ph}}^2} = \frac{P_{\text{ph}}}{I_{\text{ph}}^2}.
\end{aligned} \tag{5.5}$$

The comparison of the analytically calculated and experimentally determined stator winding parameters, see Table 5.1, demonstrates quite a good correspondence between calculated and experimental parameters.

Table 5.1: Comparison of the calculated and experimentally determined stator winding parameters.

Parameter	Test		Calculated	
	Absolute value	Per unit value	Absolute value	Per unit value
Stator phase resistance, R_{75}	0.12 Ω	0.02	0.11 Ω	0.02
Stator leakage inductance, $L_{s\sigma}$	2 mH	0.1	1.6 mH	0.08

5.2 No-load test

The no-load test was carried out according to the electrical scheme presented in Appendix D.1. In the no-load test, the star-connected stator winding of the prototype is open circuited and the field winding is supplied with different DC current values. The rotor of the generator is rotated at the nominal speed by the DC machine. The objectives of the no-load test are:

- to estimate the air gap flux density;
- to determine the PM-induced voltage;
- to observe the no-load induced voltages;
- to build the no-load characteristic and
- to reveal the stator iron and mechanical losses.

To estimate the air gap flux density, a search coil of one turn was placed in the slots and wound around one pole pitch. Figure 5.5 illustrates the induced voltage E_{sc} waveform distribution in the search coil and its first harmonic component $E_{\text{sc},1}$ as a function of time.

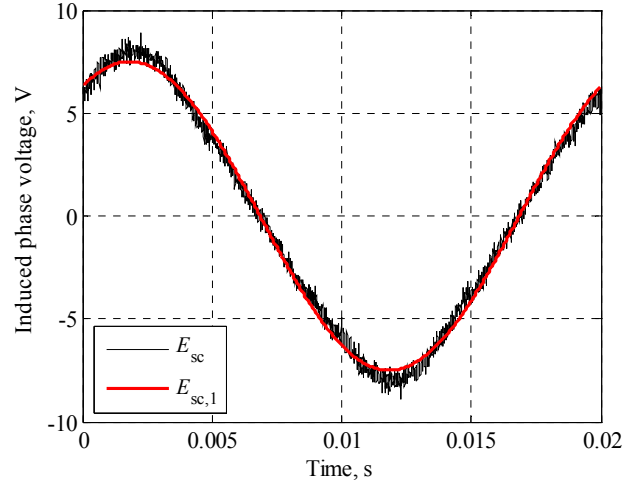


Fig. 5.5: Induced voltage of the search coil and its first harmonic component as a function of time.

Since one turn of the search coil represents two conductors, the induced voltage of one turn E_{turn} can be presented by the induced voltage of the conductor E_{cond} as

$$E_{\text{turn}} = 2E_{\text{cond}}, \quad (5.6)$$

where E_{cond} is determined in Eq. (2.1).

Based on Eq. (5.6) and Eq. (2.1), the fundamental peak air gap flux density is 0.93 T. According to the FEA, the air gap flux density is 0.95 T, which shows quite a good agreement with the experimental results.

Figure 5.6a shows the no-load PM-induced phase voltage distributions in three phases and Fig. 5.6b provides the calculated and measured phase voltages waveforms. The measured RMS value of the PM-induced phase voltage is 402 V, whereas the calculated RMS value is 422 V, which gives a 5 % difference. This discrepancy can be explained partly by the fact that the effective length of the PM rotor is less than the real length of the machine because of the end effects. This issue has been studied for instance in (Pyrhönen et al., 2010). To increase the rotor effective length, the rotor length should be made longer than the stator length. Another explanation is based on the inaccuracy of the manufacturing of the rotor poles or a slight variation in the PM material properties.

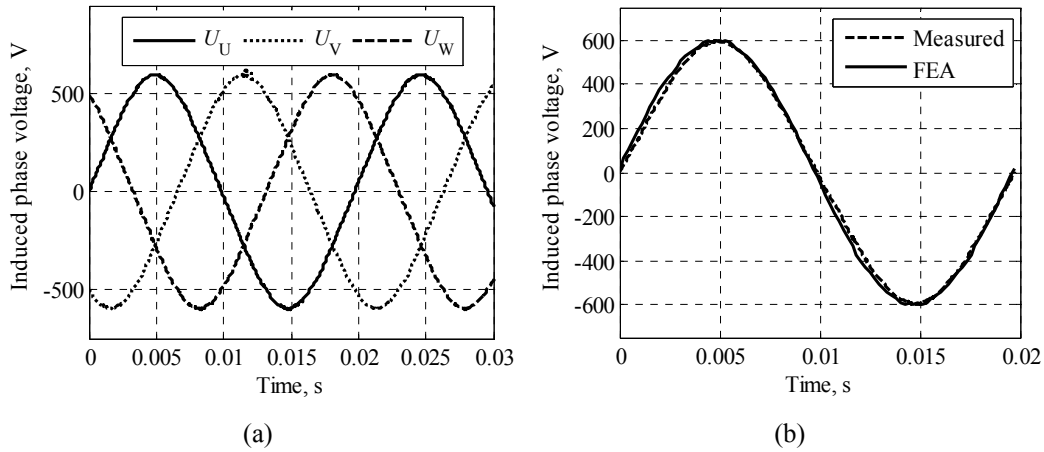


Fig. 5.6: Induced phase voltages.

(a) Measured no-load PM-induced phase voltages E_{PM} . The RMS value is $E_{PM} = 402$ V.

(b) Calculated and measured induced phase voltages E_{PM} . According to the FEA $E_{PM} = 422$ V.

The difference in the PM-induced voltages, again, influences the difference in the calculated and measured no-load characteristics, shown in Fig. 5.7. The no-load characteristic represents the open-circuit voltage E_0 as a function of the compensating winding current I_f , i.e. $E_0 = f(I_f)$, at a zero stator current I_s . As can be seen in Fig. 5.7, the measured no-load characteristic is almost linear compared with the calculated characteristic, which means that the machine will start to saturate at slightly higher compensating currents than calculated.

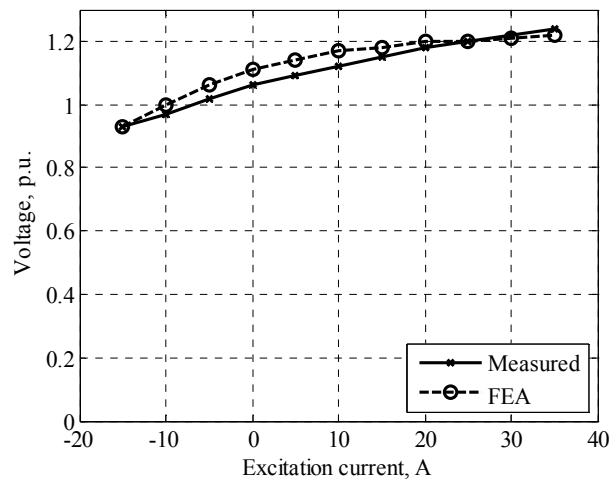


Fig. 5.7: Calculated and measured no-load characteristic of the test machine.

By measuring the input power P_{m0} for each open-circuit voltage, it is possible to determine the iron, windage and friction losses. The last two terms represent mechanical losses P_{mech} . As the speed is kept constant, the mechanical losses are constant, that is, $P_{mech} = \text{const}$. Only the iron losses $P_{s,Fe}$ increase approximately with voltage squared, see Fig. 5.8.

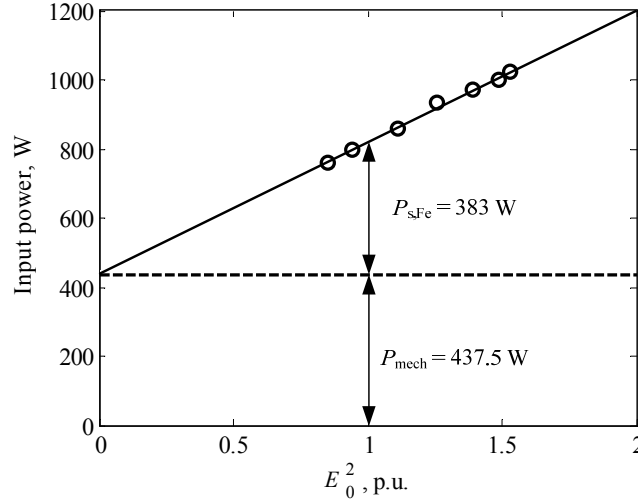


Fig. 5.8: Input power as a function of squared open-circuit voltage at the rated speed.

Table 5.2 presents the comparison of the calculated and experimentally determined iron and mechanical losses. The results of the analytical calculation of the iron losses were obtained by using the equation given in (Vogt, 1983):

$$P_{Fe} = k_{Fe,ys} P_{15} \left(\frac{B_{ys}}{1.5} \right)^2 m_{Fe,ys} + k_{Fe,ds} P_{15} \left(\frac{B_{ds}}{1.5} \right)^2 m_{Fe,ds}, \quad (5.7)$$

where $m_{Fe,ys}$ and $m_{Fe,ds}$ are the masses of the stator yoke and teeth, respectively, B_{ys} and B_{ds} are the flux densities in the stator yoke and teeth, respectively, P_{15} is the specific total loss of the material at 1.5 T and the frequency under observation, and $k_{Fe,ys}$ and $k_{Fe,ds}$ are the empirical correction coefficients, which for the SM are $k_{Fe,ys} = 1.5-1.7$ and $k_{Fe,ds} = 2$. The specific total loss of M600-50A according to (Surahammars Bruk, 2008) is 5.17 W/kg.

The results of the FEA presented in Table 5.2 were obtained by the Loss Surface Model (LSM), which is integrated in the FEM software FLUX®. In Eq. (5.7) it is assumed that the flux densities in the stator yoke and teeth are uniformly distributed, which is not correct, and as a result, the difference between the analytical and experimental results is close to three times. The LS method in the 2D FEA also gives overestimated iron losses with the difference of about 30 %. The 3D FEA should give the results with low errors.

As it can be seen in Table 5.2, the mechanical losses are underestimated. The mechanical losses were calculated based on Eq. (2.3), which is usually used for the traditional SGs. The difference between the calculated and experimentally determined mechanical losses is about 40 %, which can be explained partly by the special structure of the test machine. Another reason lies in the fact that the rotor of the test machine was not balanced. A special analysis should be made in this area.

Table 5.2: Comparison of the calculated and experimentally determined stator iron and mechanical losses.

Parameter	Analytical	FEA	Test
Stator iron losses, $P_{s,Fe}$	1080 W	532 W	383 W
Mechanical losses, P_{mech}	270 W	-	438 W

5.3 Sudden three-phase short-circuit test

The sudden three-phase short-circuit test was carried out in order 1) to study whether the short-circuit requirement mentioned in the machine constraints is met: the sustained short-circuit current must be 300 % of the rated current for at least 2 s. This condition is one of the most challenging requirements for pure PMSGs; and 2) to determine the d-axis synchronous inductance L_d . The sudden three-phase short-circuit test is made according to the electrical scheme presented in Appendix C.3.

During the test, the generator is rotated at the nominal speed, and all three output phases are short circuited through switches. At the beginning, the switches are turned off and the generator is running at no load without electrical excitation. In the whole test, the excitation is produced only by the PMs, and the compensating winding is short-circuited. After some time (several periods), the switches are turned on. The objective of the test is to observe the short-circuit currents in all phases. Figure 5.9 presents the variation of voltages and currents in time before and after short-circuiting the terminals of the armature winding with the shorted field winding. After short-circuiting the terminals, the armature currents stabilize into the sustained values I_{sc} of the short-circuit currents.

When the sustained short-circuit current I_{sc} is reached, the field winding current I_f is increased until $I_{sc} = 3I_s$. Figure 5.10 provides the calculated and experimentally determined short-circuit characteristics where the sustained short-circuit current I_{sc} is a function of the compensating current I_f .

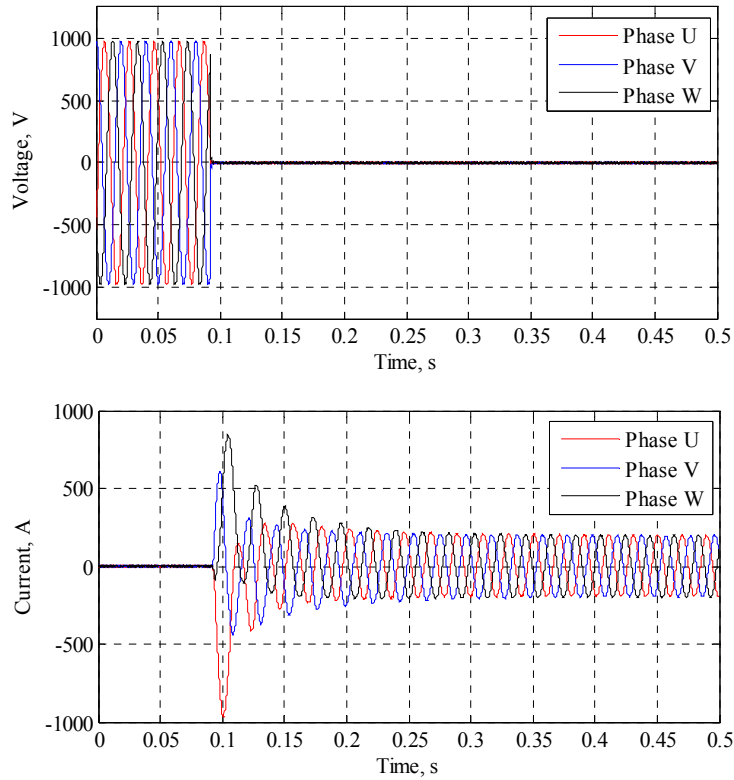


Fig. 5.9: Variation in voltage and currents in time before and after a sudden three-phase short circuit.

The sustained short-circuit current I_{sc} is 2.3 times the generator nominal current I_s .

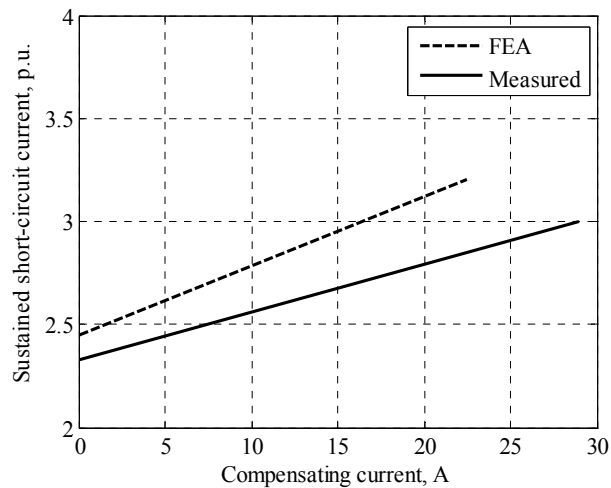


Fig. 5.10: Short-circuit characteristic.

As it can be seen in Fig. 5.10, the results of the calculated I_{sc} at $I_f = 0$ are in a fairly good agreement with the experimental one, but a further increase in the excitation current gives different values of I_{sc} . This can be explained by the difference between the calculated and actual PM-induced voltages E_{PM} of the machine. The test machine requires more compensating current to compensate the armature reaction at short circuit. The short-circuit characteristic, however, proves that the test machine can meet the short-circuit requirement, that is, $I_{sc} = 3I_s$, when the excitation current is $I_f = 29$ A and the corresponding excitation current density is moderate $J_f = 3.9$ A/mm².

By the results of the short-circuit test it is also possible to determine the following quantities:

- the short-circuit current components, e.g. subtransient I'' , transient I' and sustained short-circuit I_{sc} currents;
- direct-axis subtransient L''_d , transient L'_d and synchronous L_d inductances and
- direct-axis subtransient τ''_d and transient time constants τ'_d .

The d-axis synchronous inductance L_d in p.u. can be expressed as:

$$L_d = \frac{E_{PM}}{I_{sc}}, \quad (5.8)$$

where E_{PM} is the no-load PM-induced voltage. The results of the calculated and experimentally determined d-axis synchronous inductances presented in Table 5.3 give quite a good correspondence between the FEA and the experimental results. The result of the analytical calculation is in a relatively good correspondence with the experimental one.

Table 5.3: Comparison of the determined direct-axis inductances.

Parameter	Analytical	FEA	Test
d-axis inductance, L_d	0.4 p.u.	0.45 p.u.	0.46 p.u.

The subtransient and transient current components as well as the subtransient and transient inductances and time constants are defined using the curves of the short-circuit currents, see Fig. 5.11. To separate the asymmetrical or aperiodic armature current component from the alternating or periodic current component in each phase, the upper and lower envelopes of the short-circuit current curve must be extrapolated, as shown in Fig. 5.11a. An algebraic half-sum and algebraic half-difference of the ordinates of the upper and lower envelopes of the short-circuit current in different phases give the asymmetrical and alternating armature current components, respectively.

The average curve of the armature current alternating component, which is determined as the mean arithmetic value of all alternating current components of all three phases,

consists of the sustained short-circuit I_{sc} , the transient I' and the subtransient I'' components. To determine I' and I'' , I_{sc} is subtracted from the average curve of the armature current alternating component. The remaining part, which is the sum of $(I' + I'')$, is plotted on a semi-log scale, see Fig. 5.11b. The extrapolation of the latter part of this plot to the time corresponding to the start of the short circuit gives the initial value of the transient current component I'_0 . The time needed for the transient current component I' to decay to $1/e \approx 0.368$ of its initial value from $I'_0 = 146.6$ A to $I' = 53.9$ A is called the d-axis transient short-circuit time constant τ'_d . In this test $\tau'_d = 83$ ms. The d-axis transient inductance L'_d is the ratio of the no-load voltage E_{PM} to the sum of the $(I_{sc} + I'_0)$:

$$L'_d = \frac{E_{PM}}{\omega_s (I_{sc} + I'_0)}. \quad (5.9)$$

The subtransient short-circuit current component I'' is defined as the difference between the $(I' + I'')$ curve and the curve representing I' . I'' as a function of time is also plotted on the semi-log scale, see Fig. 5.11c. Extrapolation of this plot to the beginning of the short circuit gives the initial value of the subtransient current component I''_0 . The d-axis subtransient short-circuit time constant $\tau''_d = 12.6$ ms is the time needed for the I'' to decay to $1/e \approx 0.368$ of its initial value from $I''_0 = 309.7$ A to $I'' = 113.9$ A. The d-axis subtransient inductance L''_d is the ratio of the no-load voltage E_{PM} to the sum of the $(I_{sc} + I'_0 + I''_0)$:

$$L''_d = \frac{E_{PM}}{\omega_s (I_{sc} + I'_0 + I''_0)}. \quad (5.10)$$

When the field winding is open circuited the test machine becomes a pure PMSG. The analyses of the short-circuit results in this case are carried out as discussed above with the exception that there is no transient current component I' in the short-circuit current curves, and hence, there are no L'_d and τ'_d in this case.

Table 5.4 presents the comparison of the experimentally determined inductances and time constants with the FEA. It should be noted that since the no-load voltage in the short-circuit tests was close to the rated value, the determined quantities are saturated. To obtain the unsaturated quantities, the tests should be made at lower no-load voltages, for instance $(0.1-0.4)U_n$, which results in a high demagnetization compensating current.

Table 5.4: Comparison of the determined inductances and time constants.

Parameter	Test	FEA
d-axis subtransient inductance, L''_d	0.13 p.u.	0.14 p.u.
d-axis transient inductance, L'_d	0.19 p.u.	0.18 p.u.
d-axis subtransient time constant, τ''_d	0.013 s	0.140 s
d-axis transient time constant, τ'_d	0.083 s	0.218 s

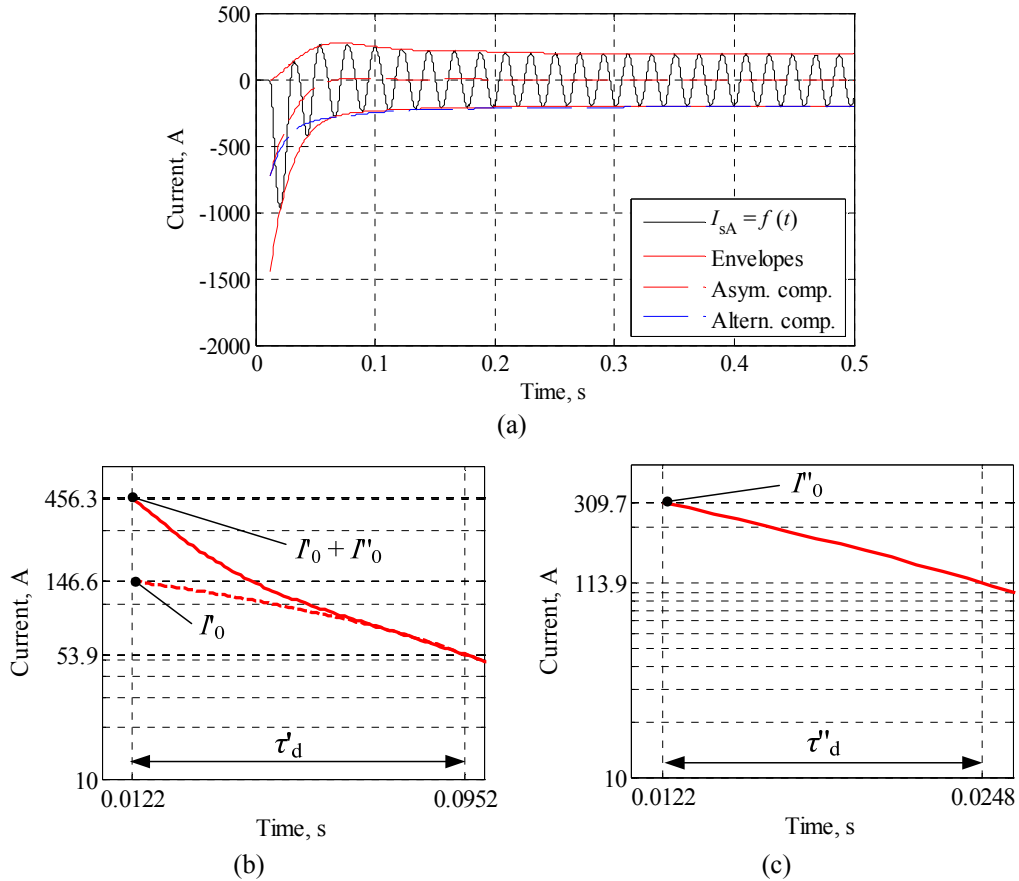


Fig. 5.11: Determination of the short-circuit current components and the corresponding time constants.

(a) Short-circuit current of one phase as a function of time with the shorted field winding. The magnitude of the sustainable short-circuit current is $I_{sc} = 198.4$ A.

(b) Determination of the initial value of the transient current component I_0 and the d-axis transient short-circuit time constant τ'_d .

(c) Determination of the initial value of the subtransient current component I''_0 and the d-axis subtransient short-circuit time constant τ''_d .

5.4 On-load test in island operation

The on-load test in island operation was performed according to the electrical scheme presented in Appendix D.2. In these tests, the rotor of the generator was rotated at the nominal speed, that is, $n = 750$ rpm, and the generator supplied active resistors with different resistance values and an induction machine working at no load. The objectives of these tests are:

- to determine the quadrature-axis synchronous inductance L_q ;
- to build the external $U_s = f(I_s)$ and regulation $I_f = f(I_s)$ characteristics and
- to calculate the test machine losses P_{loss} and efficiency η ;

5.4.1 Quadrature-axis inductance

The q-axis synchronous inductance L_q is determined applying Eq. (1.14) and Eq. (1.15), where L_d and L_q are represented as a function of the load angle δ and the power factor angle φ . Figure 5.12 presents the behaviour of L_d , L_q as a function of δ when the generator supplies the resistive load at a zero compensating current. The terminal voltage is $U_s = 1.04$ p.u. and the stator current is $I_s = 0.34$ p.u.

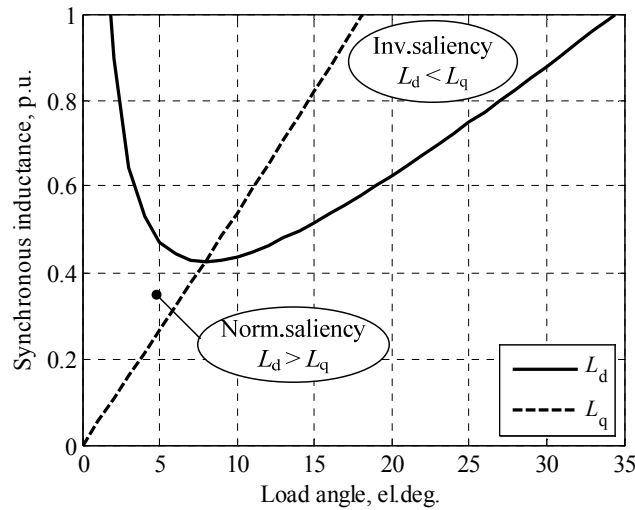


Fig. 5.12: Synchronous inductances as a function of load angle at a pure resistive load. The PM-induced voltage is $E_{PM} = 1.05$ p.u., the terminal voltage is $U_s = 1.04$ p.u., and the stator current is $I_s = 0.34$ p.u. The determined q-axis synchronous inductance is $L_q = 0.63$ p.u.

Table 5.5: Comparison of the calculated and experimentally determined q-axis inductances.

Parameter	Analytical	FEA	Test
q-axis synchronous inductance, L_q	0.56 p.u.	0.59 p.u.	0.63 p.u.

As it can be seen in Fig. 5.12, the curves $L_d = f(\delta)$ and $L_q = f(\delta)$ define the normal salient and inverse-salient pole areas. Since $L_d < L_q$ in the test machine, the determined value is $L_q = 0.63$ p.u. The final L_q is calculated as the average value at different resistive loads. The results of the calculated and experimentally determined q-axis

inductances presented in Table 5.5 give quite a good correspondence between each other.

5.4.2 External and regulating characteristics

For the traditional SGs, the voltage regulation characteristic shows how the machine voltage changes as a function of load at constant excitation, that is, $U_s = f(I_s)$ at $i_f = \text{const}$, $\cos \phi = \text{const}$, $f = f_n$. Since the PM excitation is dominating in a machine of this type, the external characteristic is built at a zero compensating current $i_f = 0$.

Figure 5.13a provides the voltage regulation characteristics at three different power factors: $\cos \phi = 1$, $\cos \phi = 0.9_{\text{ind}}$ and $\cos \phi = 0.8_{\text{ind}}$, the performance of which can be explained by the behaviour of the armature reaction. If the terminal voltage of the SG is expressed as

$$\underline{U}_s = \underline{E}_m - j\omega_s L_{s\sigma} \underline{I}_s - R_s \underline{I}_s, \quad (5.11)$$

because of the relatively small values of $L_{s\sigma}$ and R_s , it is easy to show that the terminal voltage is mainly determined by the air gap EMF E_m . The behaviour of E_m , or more precisely, the air gap flux linkage Ψ_m inducing this EMF, mainly determines the performance of the voltage regulation curve. The air gap flux linkage Ψ_m is more sensitive to the direct axis armature reaction since it is oriented in the same axis as the rotor excitation.

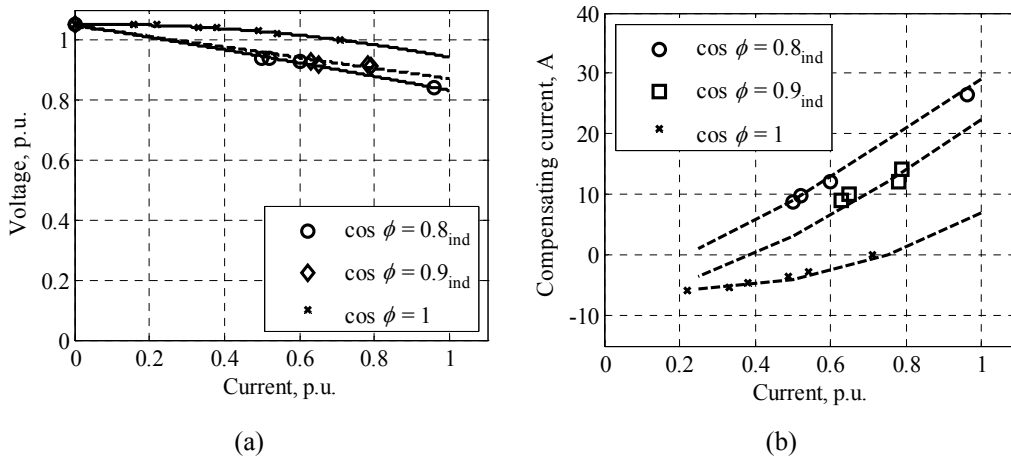


Fig. 5.13: External and regulating characteristics.

(a) External characteristic $U_s = f(I_s)$ at $i_f = \text{const}$, $\cos \phi = \text{const}$ and $f = f_n$.

(b) Regulating characteristic $i_f = f(I_s)$ at $U_s = \text{const}$, $\cos \phi = \text{const}$ and $f_n = \text{const}$.

When the load is resistive-inductive, that is, the current lags the voltage, see Fig. 5.13, there is a significant demagnetization armature reaction, which increases with the

machine load current I_s , and therefore, the terminal voltage U_s reduces when the current I_s increases. At a pure resistive load, see Fig. 5.13a, there is also a demagnetization armature reaction, but the angle ψ between the q-axis and the current I_s is less compared with the situation when the power factor is $\cos \varphi < 1$. Therefore, the armature reaction is weaker than in the previous case, and the decrease in the terminal voltage U_s is lower when the current I increases. At a resistive-capacitive load or when the current I_s leads the voltage U_s , the armature reaction is magnetizing, and thus, the terminal voltage U_s should increase with the load rise.

In general, the regulating characteristic is $i_f = f(I_s)$ at $U_s = \text{const}$, $\cos \varphi = \text{const}$ and $f_n = \text{const}$ and reveals how the excitation current i_f should be changed at different loads to keep the terminal voltage U_s constant. The regulating characteristics depicted in Fig. 5.13b are built for three different power factors: $\cos \varphi = 1$, $\cos \varphi = 0.9_{\text{ind}}$ and $\cos \varphi = 0.8_{\text{ind}}$.

As it can be seen in Fig. 5.13b, because of the overmagnetized magnetic circuit at some low loads, depending on the load power factor, the test machine must operate with a negative compensating current. In most of the cases, the SGs are loaded at 60–80 % of the load, and therefore, no negative compensating currents are needed at resistive-inductive loads. However, if the SG must supply purely resistive loads at the rated terminal voltage, some negative compensating current is needed at a low power. It should be noticed that at 70 % of the load and $\cos \varphi = 1$, the test machine can work without compensating current.

If $U_n \pm 10\%$ voltage is allowed, the generator can work with a resistive load from zero to the rated power as a pure PMSG.

With $\cos \varphi = 0.8_{\text{ind}}$ load and -10% voltage allowed, the generator can work up to 70 % of the rated load as a pure PMSG.

5.4.3 Losses and efficiency

The efficiency of an electrical machine is the ratio of the output power P_{out} to the input power P_{in} . Since it is much easier to measure the output power of the generator with relatively small errors, it is more convenient to present the input power P_{in} as the sum of the output power P_{out} and the total sum of losses ΣP_{loss} , and thereby calculate the efficiency as

$$\eta = \frac{P_{\text{out}}}{P_{\text{in}}} = \frac{P_{\text{out}}}{P_{\text{out}} + \Sigma P_{\text{loss}}}. \quad (5.12)$$

Table 5.6 presents the comparison of the calculated and experimentally determined losses and the efficiency in the rated point and $\cos \varphi = 0.8_{\text{ind}}$. The total losses in Table 5.6 contain mechanical losses, stator and rotor copper losses, stator iron losses and additional losses. The additional losses were not determined experimentally because of

the limited measuring tools. However, (Pahomin, 2007) as suggests, the additional losses are assumed to be 0.5% of the output power P_n for the SGs with the power less than 1 MW. Thus, the additional losses are equal to 275 W.

Table 5.6: Comparison of the calculated and experimentally determined losses and efficiency in the rated point and $\cos \phi = 0.8_{\text{ind}}$.

Parameter	Analytical	FEA	Test
Output power, P_n	55 kW	55 kW	55 kW
Mechanical losses, P_m	270 W	-	440 W
Iron losses, P_{Fe}	-	530 W	385 W
Stator copper losses, P_{sCu}	1190	-	1300 W
Rotor copper losses, P_{rCu}	587 W	-	760 W
Additional losses, P_{add}	275 W	275	275
Total losses, P_{loss}	2855 W		3160 W
Efficiency, η	95.1 %		94.6 %

Figure 5.14 depicts the partial load efficiency characteristics with different load power factors as parameters, where the efficiency η is shown as a function of the load current I_s . Usually, SGs do not work at a full load, but they are typically loaded in the range of 60–80 % of the load. Therefore, the maximum efficiency should be in this range as in Fig. 5.14.

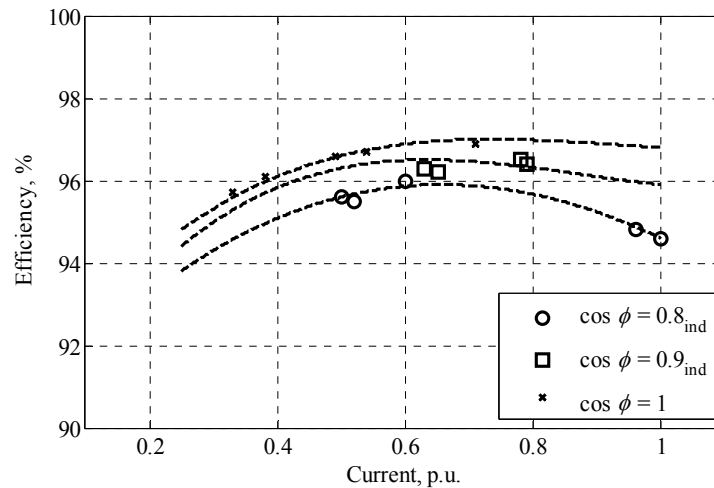


Fig. 5.14: Partial load efficiency characteristics with different load power factors as parameters.

5.5 Locked rotor test

The subtransient inductances L''_d , L''_q characterize the machine behaviour in transients when their additional role is to deliver the electromagnetic coupling between the stator

and rotor windings. Figure 5.15 presents the equivalent circuit for the subtransient inductances L''_d and L''_q , where the notations are: $L_{s\sigma}$ and $L_{f\sigma}$ are the leakage inductances of the stator and field windings, respectively; $L_{D\sigma}$ and $L_{Q\sigma}$ are the damper winding leakage inductances in the direct and quadrature axes, and L_{md} and L_{mq} are the magnetizing inductances resulting from the direct and quadrature armature reactances.

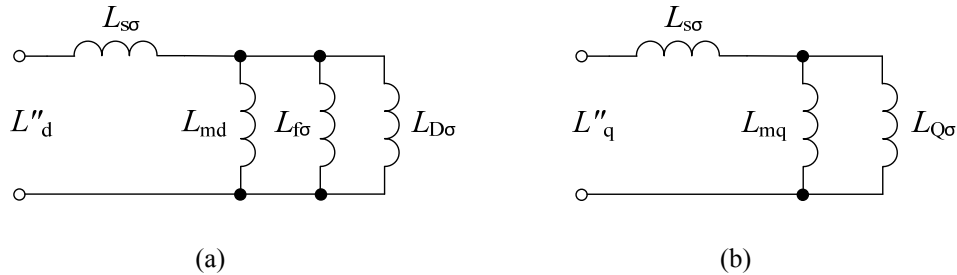


Fig. 5.15: Equivalent circuits for the subtransient inductances of an SM.
 (a) Direct axis.
 (b) Quadrature axis.

The equivalent circuits of a transformer and an asynchronous machine in a short-circuit condition resemble the equivalent circuits for the SM subtransient inductances depicted in Fig. 5.15. By taking this resemblance into account, the applied voltage test with the rotor locked in direct and quadrature axes can be used to determine the subtransient inductances L''_d and L''_q . During the measurements, the non-rotatable but pulsating air gap magnetic flux is produced to take into account the structural features of an SM and to ensure the inductive coupling between the stator and rotor windings in measurements similar to actual processes. The notion of "locked in the direct and quadrature axes" is relative to a particular phase. Indeed, the axis of one phase can be aligned with the direct axis or the quadrature axis, while the two other phases are not. The locking of the rotor should be defined in relation to one phase.

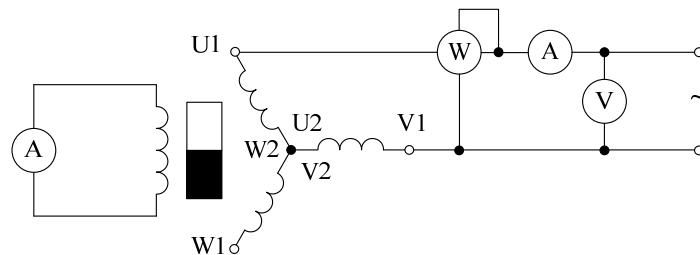


Fig. 5.16: Machine test circuit for the determination of the subtransient parameters.

When the symmetrical supply power occurs at some time instant, a current in one phase is equal to zero, whereas in two other phases the currents are equal and oppose each

other. The same situation is found in the test circuit presented in Fig. 5.16. The sinusoidal AC voltage with a constant frequency is supplied to two terminals of the generator. The field winding is short-circuited through an ammeter, where an AC current is flowing. The ammeter will have the maximum deviation if the magnetic field is oriented along the rotor pole axis, which corresponds to the direct-axis position. The minimum deviation in the ammeter corresponds to the quadrature-axis position.

The direct and quadrature positions can also be defined by applying DC current into any two line terminals of the armature winding. It is also possible to connect one phase coil branch in series with the parallel connection of the other two phase coil branches and let a DC current run in the windings. The rotor aligns with the flux generated by the DC-current-fed phase coils. If the polarity of the DC current is changed, the rotor should be aligned accordingly. These positions are determined as d-axis positions, and the q-axis position is in the middle of these two d-axis positions.

When the AC voltage supply is applied, the rotor is slowly rotated to determine the direct and quadrature axis positions. At the beginning, the AC voltage is set so that $I \leq (0.3-0.4) I_n$. After that, the AC voltage is decreasing with 4–5 approximately equal intervals of the current. To determine the field winding leakage inductance in the direct-axis position, the tests are carried out in two different conditions: 1) the field winding is short circuited and 2) the field winding is open circuited.

Table 5.7: Comparison of the calculated and experimentally determined subtransient parameters.

	Absolute value	Per unit value
Direct-axis subtransient inductance, L''_d (the field winding is open circuited)	4.93 mH	0.24
Direct-axis subtransient inductance, L''_d (the field winding is short circuited)	3.67 mH	0.18
Quadrature-axis subtransient inductance, L''_q	7.63 mH	0.38
Direct-axis subtransient resistance, R''_d (the field winding is open circuited)	0.325 Ω	0.05
Direct-axis subtransient resistance, R''_d (the field winding is short circuited)	0.190 Ω	0.03
Quadrature-axis subtransient resistance, R''_q	0.389 Ω	0.06

The subtransient inductances are determined based on the following equations:

$$Z''_{d,q} = \frac{U}{2I}, \quad (5.13)$$

$$R''_{d,q} = \frac{P}{2I^2}, \quad (5.14)$$

$$L''_{d,q} = \sqrt{Z''_{d,q}{}^2 - R''_{d,q}{}^2}. \quad (5.15)$$

Table 5.7 presents the results of the measured subtransient parameters.

5.5.1 Damper winding parameters

The damper winding parameters are calculated from the applied voltage test with the fixed rotor when the field winding is open circuited. The damper winding resistance seen by the stator is:

$$R_{D,Q} = R''_{d,q} - R_s. \quad (5.16)$$

If the iron losses are taken into account, the damper winding resistance seen by the stator becomes

$$R_{D,Q} = \frac{R_{Fe}(R''_{d,q} - R_s)}{2R_s - R''_{d,q}}. \quad (5.17)$$

In the case when an SM does not have a field winding that would correspond to the test when the field winding is open circuited, the subtransient inductances L''_d and L''_q are defined by a connection of the stator leakage inductance $L_{s\sigma}$ in series with the parallel connection of the damper winding leakage inductance $L_{D\sigma,Q\sigma}$ and the magnetizing inductance $L_{md,mq}$

$$L''_d = L_{s\sigma} + \frac{L_{md}L_{D\sigma}}{L_{md} + L_{D\sigma}}, \quad (5.18)$$

$$L''_q = L_{s\sigma} + \frac{L_{mq}L_{Q\sigma}}{L_{mq} + L_{Q\sigma}}. \quad (5.19)$$

The direct- and quadrature-axes damper winding leakage inductances solved from Eq. (5.19) and Eq. (5.20) are:

$$L_{D\sigma} = \frac{L_{md}(L''_d - L_{s\sigma})}{L_{md} - L''_d + L_{s\sigma}}, \quad (5.20)$$

$$L_{Q\sigma} = \frac{L_{mq}(L''_q - L_{s\sigma})}{L_{mq} - L''_q + L_{s\sigma}}. \quad (5.21)$$

Table 5.8 presents the measured and analytically calculated values of the damper winding parameters.

Table 5.8: Comparison of the calculated and experimentally determined damper winding parameters.

Parameter	Measured		Calculated
	Absolute value	Per unit value	Per unit value
D-axis damper winding resistance, R_D	0.317 Ω	0.05	0.06
Q-axis damper winding resistance, R_Q	0.380 Ω	0.06	0.05
D-axis damper winding leakage inductance, $L_{D\sigma}$	4.64 mH	0.23	0.05
Q-axis damper winding leakage inductance, $L_{Q\sigma}$	12.9 mH	0.64	0.09

Table 5.8 shows that the calculated damper winding resistances are more or less close to the experimentally determined ones. However, the experimentally determined damper winding leakage inductances are much higher compared with analytical ones. This can be explained by the wrong arrangement of the damper bars when the laminations of the pole shoes were cut. As can be seen in Fig. 4.10, the central three bars are buried deeper than the edged ones. This leads to an increase in the damper winding leakage inductance.

5.5.2 Compensating winding parameters

The compensating winding parameters include the compensating winding resistance R_f and the compensating winding leakage inductance $L_{f\sigma}$. The DC compensating winding resistance is determined in the same way as the stator winding phase resistance, see Section 5.1.

The field winding leakage inductance is calculated from the applied voltage test with the fixed rotor when the field winding is short circuited. In this case, the subtransient inductances L''_d and L''_q are defined by a connection of the stator leakage inductance $L_{s\sigma}$ in series with the parallel connection of the damper winding leakage inductance $L_{D\sigma, Q\sigma}$, the field winding leakage inductance $L_{f\sigma}$ and the magnetizing inductance $L_{md, mq}$

$$L''_d = L_{s\sigma} + \frac{L_{md} L_{D\sigma} L_{f\sigma}}{L_{D\sigma} L_{f\sigma} + L_{md} L_{f\sigma} + L_{md} L_{D\sigma}}. \quad (5.22)$$

Further, the solution for the field winding leakage inductance derived from (5.23) is:

$$L_{f\sigma} = \frac{L_{md} L_{D\sigma} (L''_d - L_{s\sigma})}{(L_{md} L_{D\sigma} + (L_{s\sigma} - L''_d)(L_{D\sigma} + L_{md}))}. \quad (5.23)$$

Table 5.9 presents a comparison of the calculated and experimentally determined field winding parameters. According to this comparison, the difference between the calculated and experimentally determined results is about 30 %.

Table 5.9: Comparison of the calculated and experimentally determined field winding parameters.

Parameter	Measured		Calculated	
	Absolute value	Per unit value	Absolute value	Per unit value
Field winding resistance, R_f	0.936 Ω	0.13	1.076	0.17
Field winding leakage inductance, $L_{f\sigma}$	3.83 mH	0.19	2.62 mH	0.13

5.6 Network operation

In these experimental tests, the test machine is operated in parallel with the network. In general, the requirements for an SG working in parallel with the network are almost the same as for an SG working in the island operation. The main difference is that the SG in network operation should also supply the capacitive load with $\cos \varphi = 0.9_{\text{cap}}$. However, the operation of an SG differs in network operation. In network operation, the grid is rigid and the generator terminal voltage level fully depends on the network voltage. In island operation, the power factor is determined by the load power factor, whereas in network operation the power factor depends on the machine excitation level. If the SG is overexcited, that is, the generator EMF E_f is more than the network voltage U_s , the power factor has inductive behaviour, and if the SG is underexcited, that is, $E_f < U_s$, the power factor acts as a capacitive one.

The performance analyses of the test machine in network operation are based on the V-curve and the regulating characteristics discussed below.

The V-curve characteristic of an SG working in parallel with the network represents the stator current I_s and the power factor $\cos \varphi$ as a function of the excitation current I_f , or the compensating current in this prototype, at a constant voltage, frequency and active power, i.e. $U_n = \text{const}$, $f_n = \text{const}$, and $P = \text{const}$. As is known, the active power is $P = mU_{\text{nph}}I_s \cos \varphi = mU_{\text{nph}}I_a = \text{const}$, where $I_a = I_s \cos \varphi$ is the active component of the current. At the same time, $P = T_{\text{em}}\Omega_s$, where T_{em} is the electromagnetic torque of the generator, and the mechanical angular speed $\Omega_s = 2\pi n_s = \text{const}$, because the synchronous speed of the generator n_s is constant. Therefore, the condition $P = \text{const}$ means that the generator works at a constant electromagnetic torque. The experimentally determined V-curve characteristics of the test machine are presented in Fig. 5.17.

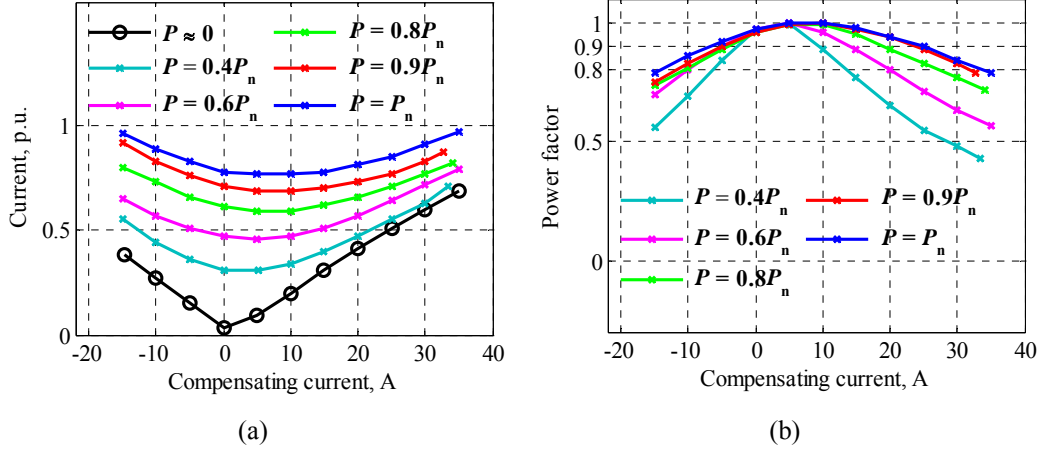


Fig. 5.17: V-curve characteristics of the test machine.

(a) Stator current I_s as a function of the compensating current I_f .

(b) Power factor $\cos \varphi$ as a function of the compensating current I_f .

As it can be seen in Fig. 5.17, the V-curves of the test machine resemble the V-curves of the traditional SGs with the exception that the underexcited parts (left parts of the V-curves) lie in the negative part of the compensating current. The experimentally determined V-curves show that the proposed machine can work in parallel with the network by meeting the power factor requirement, that is, $0.9_{\text{cap}} < \cos \varphi < 0.8_{\text{ind}}$.

As it was mentioned above, the regulating characteristic represents the compensating current as a function of stator current at a constant voltage, frequency and power factor, i.e. $U_n = \text{const}$, $f_n = \text{const}$, and $\cos \varphi = \text{const}$, as shown in Fig. 5.18.

As can be seen in Fig. 5.18, the curves of the regulating characteristics differ from the curves presented in Fig. 5.13b. According to Fig. 5.18, the test machine supplies the loads with the power factors $\cos \varphi_{\text{ind}} = 0 \leq \cos \varphi \leq 1$ at positive compensating currents. This can be explained by the grid voltage U_n , the nominal value of which is 400 V. During all these tests, the grid voltage was between 404 V and 405 V, which is higher than the test machine no-load voltage $E_{\text{PM}} = 402$ V. Thus, the test machine was underexcited all the time.

The behaviour of the regulating characteristics shown in Fig. 5.18 obviously demonstrates the effect of the armature reaction on the PM excitation. When the current I_s lags the voltage U_s , the armature reaction is demagnetizing, and to compensate this armature reaction, a positive compensating current I_f is needed. At a pure resistive load, the quadrature armature reaction does not significantly affect the PM excitation, and the compensating current is lower than in the previous case. When the current I_s leads the voltage U_s , the armature reaction is magnetizing, and therefore, the compensating

current I_f must change its polarity so that it becomes negative to compensate the magnetizing armature reaction.

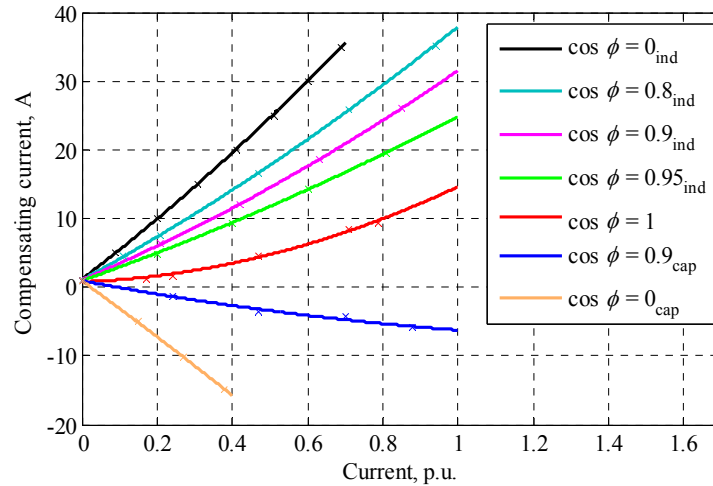


Fig. 5.18: Regulating characteristic of the test machine.

5.7 Thermal analysis

To determine the temperature in the PMs, two thermal sensors (Pt100) were placed between a PM and rotor iron, as shown in Fig. 5.19a. One sensor was placed right in the middle of the PM length and the second one was installed at 25 % of the PM length from it. The cables that connect the Pt 100 with a transmitter go into the shaft before the end shield bearing, see Fig. 5.19b. The transmitter is installed at the edge of the shaft whereas the receiver box is mounted on the end cap that covers the external fan. Inside the receiver box there is an IC chip FT245RL, which communicates with a PC over USB.

The analytical calculation is based on the thermal resistance network discussed in Chapter 3. Since the built rotor is placed in the frame of an induction machine, the test machine is a conventional totally enclosed (TE) design. The thermal conductivities of the test machine materials in different regions were taken from (Polikarpova et al., 2012). The convection coefficients calculated based on (Monushko and Pomogaev, 2009) are presented in Table 5.10. The temperature of the surrounding medium was 25°C. Table 5.11 presents the comparison of the calculated and measured temperatures in the PM, where the measured temperature is the average value of the results received from both sensors Pt 100.

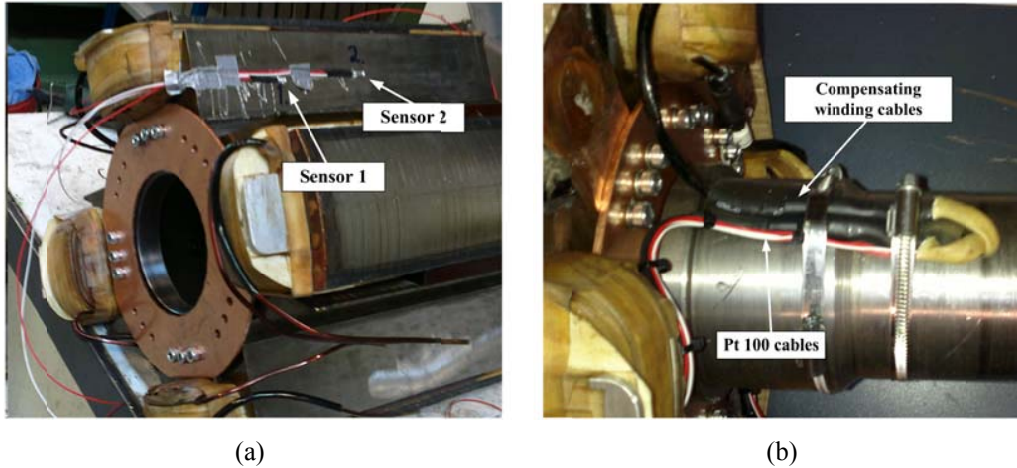


Fig. 5.19: Photos of the built rotor prototype.
 (a) Arrangement of the thermal sensors Pt 100.
 (b) Displacement of the compensating winding and the Pt 100 cables in the rotor.

Table 5.10: Convection coefficients used in the thermal design.

Convection coefficient	Value	Unit
Frame:		
fan side	105.02	W/(m ² K)
prime mover side	50.38	W/(m ² K)
central part	49.57	W/(m ² K)
Bearing shield	48.47	W/(m ² K)
Stator winding		
outer part	18.55	W/(m ² K)
inner part	26.61	W/(m ² K)
Rotor end winding	147.08	W/(m ² K)
Air gap	27.57	W/(m ² K)

Table 5.11: Comparison of the calculated and measured temperatures in the PM.

Parameter	Measured	Calculated
Temperature in the PM	50°C	66°C

Although the results of the analytical calculation give a higher temperature, both the measured and calculated results verify that the machine operates within safe temperature limits for the PMs.

5.8 Summary

This chapter presented the steady-state and dynamic performance of the test machine. A number of tests to determine different characteristics and machine parameters were considered in detail. The results of the experimental measurements fully demonstrated the operation principle of the proposed armature-reaction-compensated permanent magnet synchronous generator and fulfilment of the defined constraints. The main parameters of the test machine are gathered and presented in Table 5.12.

Table 5.12: Main parameters of the test machine.

Parameter	Symbol	Absolute value	Per unit value
Apparent power	S_n	69 kVA	1
Nominal power	P_n	55 kW	1
Nominal voltage	U_n	660 V	1
Nominal speed	n_n	750 rpm	-
Frequency	f_n	50 Hz	-
Nominal power factor	$\cos \varphi$	0.8 _{ind}	-
Electromotive force	E_{PM}	696 V	1.05
Stator resistance	R_s	0.12 Ω	0.02
Leakage inductance	$L_{s\sigma}$	2 mH	0.1
D-axis synchronous inductance	L_d	9.3 mH	0.46
Q-axis synchronous inductance	L_q	12 mH	0.6
D-axis damper winding resistance	R_D	0.317 Ω	0.05
Q-axis damper winding resistance	R_Q	0.380 Ω	0.06
D-axis damper winding leakage inductance	$L_{D\sigma}$	4.64 mH	0.23
Q-axis damper winding leakage inductance	$L_{Q\sigma}$	12.9 mH	0.64
Field winding resistance	R_f	0.936 Ω	0.13
Field winding leakage inductance	$L_{f\sigma}$	3.83 mH	0.19
Saturated d-axis subtransient inductance (with the compensating winding)	$L''_{d,s}$	2.6 mH	0.13
Saturated d-axis transient inductance	$L'_{d,s}$	3.8 mH	0.19
Non-saturated d-axis subtransient inductance (with the compensating winding)	$L''_{d,uns}$	3.67 mH	0.18
Non-saturated d-axis subtransient inductance (without compensating winding)	$L''_{d0,uns}$	4.93 mH	0.24
Non-saturated q-axis subtransient inductance	$L''_{q,uns}$	7.63 mH	0.38

6 Conclusions

One of the main contributions of this research work is to propose an alternative solution where an ARC-PMSG replaces a traditional EESG in island operation meeting all the requirements set for SMs. The requirements for SMs in AC island include: 1) allowable voltage range (it must be within $\pm 10\%$ of the nominal in all conditions); 2) the short-circuit requirement (the sustainable short-circuit current must be three times the rated current); 3) and the nominal power factor must be $\cos \varphi = 0.8_{\text{ind}}$.

Conventional SGs can easily meet the above requirements. However, when an SG tightly follows the main boundary requirements, it easily becomes quite a low-efficiency machine. A compromise to the conventional SG could be a pure PMSG that has a high efficiency in the absence of the field winding losses. But since the main flux of the PMSG is not adjustable, it suffers from difficulties to meet the machine constraints. To meet the requirements, a pure PMSG must be heavily overdimensioned, being thus economically inefficient. Even avoiding the short circuit requirement, which refers to the old-fashioned relays, the PMSG is economically inefficient as long as the power factor is $\cos \varphi = 0.8_{\text{ind}}$. Therefore, combining the features of both types of SMs led to the study of the HESMs.

Based on the main operation principle of the machine for island operation, that is, compensation of the armature reaction, two ARC-PMSGs (ARC-PMSG with SCL and ARC-PMSG with ACL) were proposed. The proposed ARC-PMSGs were compared with the series 6-2 HESG and the conventional EESG in Chapter 2. According to this comparison, the proposed ARC-PMSGs showed a better performance than the 6-2 HESG and EESG. At the same time, the proposed ARC-PMSGs have a disadvantage regarding the brushless excitation system: if negative compensating current is needed, the excitation system of the ARC-PMSG becomes more complex than that of the brushed system. In addition to this drawback, an ARC-PMSG with ACL has a limitation in the winding arrangement: the maximum number of parallel paths is equal to the number of pole pairs. However, from the technical and economical points of view, the ARC-PMSGs with ACL has a better efficiency, a lower total mass, less expensive PM material, a lower electricity price and a lower payback time than the ARC-PMSG with SCL. Therefore, it was decided to narrow down the research work to the ARC-PMSG with ACL.

The research work of the ARC-PMSG with ACL includes:

- development of the electromagnetic design and thermal network for the steady-state analysis;
- verification of the analytical results with the numerical results and
- building and testing of the prototype to compare the experimental results with the analytical and numerical ones.

The results of the developed electromagnetic design, that is, the PM dimensions and synchronous inductances, which represent the key issues in the design of the rotor of the ARC-PMSG, showed a relatively good correspondence with the numerical and experimental results. However, partly because the effective length of the PM-rotor is less than the actual length of the machine and partly because of the inaccuracy of the manufacturing of the rotor poles, the experimental results deviated slightly from the numerical calculations. The main discrepancy lies in the no-load PM induced voltage. The experimental no-load voltage was 5 % lower than the expected one. This in turn led to an increase in the compensating current under load and thereby to lower efficiencies at partial loads. Despite the insufficient efficiency of the test machine, the experimental results verified

- the operation principle of the ARC-PMSG with ACL: the main flux is first produced by the PMs and the excitation coil is needed only to compensate the armature reaction to keep the terminal voltage constant under load, and
- the sustainable short circuit current of the ARC-PMSG with ACL is three times the rated current for at least two seconds, which is one of the most challenging requirements for a pure PMSG.

The thermal analysis based on the thermal resistance network was carried out mainly to determine the temperature in the PMs. Although the results of the experimental and thermal resistance network had some differences, both results confirmed that the temperature in the PMs lies in a safe region.

To sum up, it could be concluded that the proposed ARC-PMSG with ACL seems a good high-efficiency alternative to replace a conventional EESG meeting the boundary requirements in an AC island.

6.1 Suggestions for future work

The future research of the ARC-PMSG with ACL for practical high-power applications requires designs limiting the q-axis armature reaction and minimizing the amount of PM material in the machines. This can be done by considering the topologies presented in Fig. 6.1. The original PMs shown in Fig. 4.1 can be split into two pairs of V-shaped PMs per pole, see Fig. 6.1a, or into three PMs per pole as shown in Fig. 6.1b.

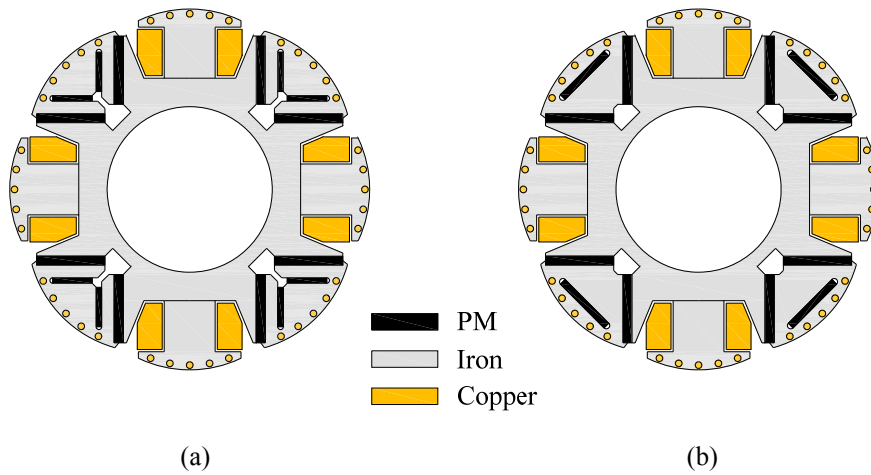


Fig. 6.1: Topologies proposed for the future work.
(a) Two pairs of V-shape PMs per pole.
(b) Three PMs per pole.

To improve the performance at a pure resistive load, which is characterized by the q -axis armature reaction, some flux barriers can be provided in the PM poles. These flux barriers could effectively compensate the q -axis armature reaction. The corresponding analysis must be made and compared with the original proposed topology.

References

- ABC (2012). [Retrieved September 20, 2012]. Available at <http://www.hok-elanto.fi/index.php?id=2460>.
- Akemakou, A.D. (2006). *Double excitation rotating electrical machine for adjustable defluxing*. Pat. US 2006/0119206 A1. Jun. 2006.
- Al-Adsani, A.S. and Schofield, N. (2009). Hybrid permanent magnet generators for electric vehicle applications. In: *IEEE International Electric Machines and Drives Conference, IEMDC 2009*, pp. 1754–1761.
- Amara, Y., Chabot, F., Gabsi, M. and Lecrivain, M. (2004). *Rotor for a rotating electric machine with hybrid excitation and corresponding electric machine*. Pat. EP 1416617 A1. May 2004.
- Amara, Y. et al. (2011). Comparison of open circuit flux control capability of a series double excitation machine and a parallel double excitation machine. *IEEE Transactions on Vehicular Technology*, vol. 60, no. 9, pp. 4194–4207.
- Amara, Y. et al. (2009). Hybrid excitation synchronous machines: energy-efficient solution for vehicles propulsion. *IEEE Transactions on Vehicular Technology*, vol. 58, no. 5, p. 2137–2149.
- Antonov, M.V. (1993). *Manufacturing process of electrical machines*. Energoatomizdat.
- Babajanyan, A. and Reutlinger, K. (2010). *Hybrid-excited electric machine*. Pat. WO 2010/023039 A1. Mar. 2010.
- Balagurov, V.A. (1982). *Design of special types of AC machines*. Vysshaya shkola (in Russian).
- Bali, H. et al. (2010). Analytical modeling of open circuit magnetic field in wound field and series double excitation synchronous machines. *IEEE Transactions on Magnetics*, vol. 46, no. 10, pp. 3802–3815.
- Boldea, I. (2006). *The Electrical Generators Handbook – Synchronous Generators*. Edition Taylor and Francis Group, LLC.
- But, D.A. (1990). *Brushless electrical machines*. Vysshaya shkola (in Russian).
- Chalmers, B.J., Akmeshe, R. and Musaba, L. (1997). PM reluctance motor with two-part rotor. In: *IEE Colloquium on New Topologies for Permanent Magnet Machines*, Digest No: 1997/090.

- Danilevich, Y.B., Dombrovskiy, V.V. and Kazovskiy E.Ya (1965). *Parameters of the AC machines*. Nauka publisher (in Russian).
- Dooley, K.A. (2011). *Saturation control of electric machine*. Pat. US 7999431. Aug. 2011.
- Fodorean, D., Djerdir, A., Viorel, I.-A. and Miraoui, A. (2007). A double excited synchronous machine for direct drive application - design and prototype tests. *IEEE Transactions on Energy Conversions*, vol. 22, no. 3, pp. 656–665.
- Fukami, T. and Shima, K. (2010). Steady-State Analysis of a Permanent-Magnet-Assisted Salient-Pole Synchronous Generator. *IEEE Transactions on Energy Conversions*, vol. 25, no. 2, pp. 388–393.
- Ganev, E., Oximberg, C.A. and Warr, W.H. (2007). *Excitation controlled synchronous permanent magnet machine*. Pat. US 7301310 B2. Nov. 2007.
- Geral, B.K. and Manoj, R.S. (2002). *Hybrid synchronous machines comprising permanent magnets and excitation windings in cylindrical element slots*. Pat. US 2002/0053850 A1. May 2002.
- Gieras, J.F. (2012). PM synchronous generators with hybrid excitation systems and voltage control capabilities: a review. In: *XXth International Conference on Electrical Machines, ICEM 2012*, Marseille, France.
- Gieras, J.F. and Rozman, G. (2011). *Voltage regulated permanent magnet generator*. Pat. US 8085003. Dec. 2011.
- Gurevich, E.I. et al. (2004). *Testing of synchronous machines*. St.Petersburg State Polytechnical University (in Russian).
- Han, J., Zhang, Z. and Jiansu, S.M. (2011). Investigation of field regulation performance of a new hybrid excitation synchronous machine with dual-direction magnetic shunt rotor. In: *International Conference on Electrical Machines and Systems (ICEMS)*, Incheon, Korea.
- Heikkilä, T. (2002). *Permanent magnet synchronous motor for industrial inverter applications – analysis and design*. Acta Universitatis Lappeenrantaensis No. 134, Doctoral thesis, Lappeenranta University of Technology.
- Hlioui, S. et al. (2008). PM and hybrid excitation synchronous machines: performances comparison. In: *18th IEEE International Conference on Electrical Machines (ICEM)*, Vilamoura, Portugal.

- Hoang, E., Lecrivain, M. and Gabsi, M. (2010). 3-D thermal model of an hybrid excitation flux switching synchronous machine using a 2-D FE method software. In: *International Symposium on Power Electronics Electrical Drives Automation and Motion, SPEEDAM 2010*, pp. 101–104.
- Hoang, E., Lecrivain, M., Hlioui, S. and Gabsi, M. (2011). Hybrid excitation synchronous permanent magnets synchronous machines optimally designed for hybrid and full electrical vehicle. In: *IEEE 8th International Conference on Power Electronics and ECCE Asia, ICPE & ECCE 2011*, pp. 153–160.
- Hosoi, T. et al. (2012). Demagnetization analysis of additional permanent magnets in salient-pole synchronous machines with damper bars under sudden short circuits. *IEEE Transactions on Industrial Electronics*, vol. 59, no. 6.
- Hua, W., Cheng, M. and Zhang, G. (2009). A novel hybrid excitation flux-switching motor for hybrid vehicles. *IEEE Transactions on Magnetics*, vol. 45, no. 10, pp. 4728–4731.
- IEC 60034-2 (1972). *Part 2: Methods for determining losses and efficiency of rotating electrical machines from tests*.
- IEC 60034-4 (1985). *Part 4: Methods for determining synchronous machine quantities from tests*. Second edition.
- Kamiev, K., Nerg, J., Pyrhonen, J. and Zaboin, V. (2010). Hybrid excitation synchronous generators for island operation. In: *XIX IEEE International Conference on Electrical Machines, ICEM 2010*, Rome, Italy.
- Kamiev, K. et al. (2012). Feasibility of different excitation methods of synchronous generators in island operation. In: *IEEE XXth International Conference on Electrical Machines, ICEM 2012*, Marseille, France, pp. 2902–2908.
- Kasyanov, V.T. (1951). *Desing of salient-pole synchronous machines*. VMAKV (in Russian).
- Kopylov, I.P., Klokov, B.K., Morozkin, V.P. and Tokarev, B.F. (2005). *Design of electrical machines*. Moscow: Vysshaya shkola (in Russian).
- Kosaka, T. and Matsui, N. (2008). Hybrid excitation machines with powdered iron core for electrical traction drive applications. In: *International Conference on Electrical Machines and Systems (ICEMS)*, Wuhan, China, pp. 2974–2979.
- Kosaka, T., Sridharbabu, M., Yamamoto, M. and Matsui, N. (2010). Design studies on hybrid excitation motor for main spindle drive in machine tools. *IEEE Transactions on Industrial Electronics*, vol. 57, no. 11, pp. 3807–3813.

- Kundur, P. (1994). *Power system stability and control*. McGraw-Hill. Inc.
- Kylander, G. (1995). *Thermal modeling of small cage induction motors*. Doctoral thesis, Chalmers University of Technology.
- Liaw, C.Z., Soong, W.L., Welchko, B.A. and Ertugrul, N. (2005). Uncontrolled Generation in Interior Permanent-Magnet Machines. *IEEE Transactions on Industry Applications*, vol. 41(4), pp. 945–954.
- Li, L. et al. (2009). Some armature reaction compensation methods numerical design of experiments and optimization for a hybrid excitation machine. In: *IEEE International Electric Machines and Drives Conference, IEMDC 2009*, Miami, United States, pp. 832–838.
- Lipo, T.A. (2011). *Analysis of synchronous machines*. Taylor & Francis Group, LLC.
- Liu, J., Howe, D., Mellor, P.H. and Jenkins, M.K. (1993). Thermal analysis of permanent magnet machines. In: *Sixth International Conference on Electrical Machines and Drives*, no. 376, pp. 359–364.
- Liu, X., Wang, C. and Zheng, A. (2011). Operation principle and topology structures of axial flux-switching hybrid excitation synchronous machine. In: *International Conference on Electrical Machines and Systems (ICEMS)*, Incheon, Korea.
- Lloyd's Register (2011). *Lloyd's register rules and regulations for the classification of ships*. Part 6, chapter 2. Available at <http://www.lloydsregister.axinteractive.com/products/208-rules-regulations-for-the-classification-of-ships-2011-part-6.aspx>.
- Luo, X. and Lipo, T.A. (1999). A synchronous/permanent magnet hybrid AC machine. In: *International Electric Machines and Drives Conference (IEMDC)*, Seattle, Washington, pp. 19–21.
- Mellor, P.H., Roberts, D. and Turner, D.R. (1991). Lumped parameter thermal model for electrical machines of TEFC design. *IEEE Proceedings B Electric Power Applications*, Vol. 138, no. 5, pp. 205–218.
- Mizuno, T. (1997). *Hybrid excitation type permanent magnet machine*. Pat. US 5682073.
- Moncada, R., Tapia, J. and Jahns, T. (2009). Inverse-saliency PM motor performance under vector control operation. In: *IEEE Energy Conversion Congress and Exposition (ECCE)*, San Jose, California, Sep. 2009, pp. 2368–2373.
- Monushko, N.D. and Pomogaev, G.V. (2009). *Thermal design of totally enclosed electrical machines*. South Ural State University (in Russian).

- Naoy, N. and Fukami, T. (2001). Trial production of a hybrid excitation type synchronous machine. In: *IEEE International Electric Machines and Drives Conference (IEMDC)*, Seattle, Washington, pp. 545–547.
- Nedjar, B. et al. (2011). A new parallel double excitation synchronous machine. *IEEE Transactions on Magnetics*, vol. 47, no. 9, pp. 2252–2260.
- Neorem Magnets (2008). *Neorem magnet Ne493a data sheet*. [Retrieved Aug. 31, 2012]. Available from <http://www.neorem.fi>.
- Nerg, J., Rilla, M. and Pyrhönen, J. (2008). Thermal analysis of radial-flux electrical machines with a high power density. *IEEE Transactions on Industrial Electronics*, vol. 55, no. 20, pp. 3543–3554.
- Pahomin, S.A. (2007). *Design of synchronous generators*. South-Russian State Technical University (in Russian).
- Patin, N. et al. (2008). Control of a hybrid excitation synchronous generator for aircraft applications. *IEEE Transactions on Industrial Electronics*, vol. 55, no. 10, pp. 3772–3783.
- Polikarpova, M. et al. (2012). Thermal design and analysis of a direct-water cooled direct drive permanent magnet synchronous generator for high-power wind turbine application. In: *IEEE XXth International Conference on Electrical Machines, ICEM 2012*, Marseille, France, pp. 1488–1495.
- Poole, N.J. and Sarvar, F. (1989). Fundamentals of heat transfer. In: *IEE Colloquium on Thermal Design of Electronic Systems*.
- Pyrhönen, J. (2007). *Lecture notes on electrical drives*. Lappeenranta University of Technology.
- Pyrhönen, J., Jokinen, T. and Hrabovcova, V. (2008). *Design of Rotating Electrical Machines*. Chichester: John Wiley & Sons.
- Pyrhönen, J. et al. (2010). Permanent-magnet length effects in AC machines. *IEEE Transactions on Magnetics*, vol. 46, no. 10, pp. 3783–3789.
- Reutlinger, K. (2010). *Electric machine comprising a rotor with hybrid excitation*. Pat. US 2010/0207480 A1. Aug. 2010.
- Rilla, M. (2012). *Design of salient pole PM synchronous machines for a vehicle traction application – analysis and implementation*. Acta Universitatis Lappeenrantaensis No. 497, Doctoral thesis, Lappeenranta University of Technology.

- Saari, J. (1995). *Thermal modelling of high speed induction machines*. Acta Polytechnica Scandinavica, Electrical Engineering series No. 82.
- Schüller, U. and Brandes, J. (1998). *Hybrid-energized synchronous electric machine*. Pat. US 5731647. Mar. 1998.
- Sergeev, P.S. (1969). *Design of electrical machines*. Energia (in Russian).
- Shi, M. et al. (2011). Design and practical implementation of a novel variable-speed generation system. *IEEE Transactions on Industrial Electronics*, vol. 58, no. 11, pp. 5032–5040.
- Shushu, Z., Chuang, L., Yihao, X. and Xiang, Z. (2010). Characteristics and experimental study on a novel tangential/radial hybrid excitation synchronous machine. In: *2nd IEEE International Symposium on Power Electronics for Distributed Generation Systems (PEDG)*, Hefei, China, pp. 883–886.
- Soldatenkova, N.A. and Boronina, L.F. (1993). *Calculation of salient-pole synchronous machines*. St.Petersburg State Polytechnical University (in Russian).
- Standard EN 50160 (2004). *Voltage Characteristics in Public Distribution Systems*. European Copper Institute, Wrocław University of Technology and Copper Development. Available at <http://www.copperinfo.co.uk/power-quality/downloads/pqug/542-standard-en-50160-voltage-characteristics-in.pdf>.
- Sulaiman, E., Kosaka, T. and Matsui, N. (2011). A novel hybrid excitation flux switching synchronous machine for a high-speed hybrid electric vehicle applications. In: *International Conference on Electrical Machines and Systems, ICEMS 2011*.
- Surahammars Bruk (2008). [Retrieved April 04, 2013]. Available from <http://www.sura.se>.
- Surahammars Bruk (2013). Ek Göran.[Personal communication]. 29 Jan. 2013.
- Syverson, C.D. and Curtiss, W.P. (1996). *Hybrid alternator with voltage regulator*. Pat. US 5502368. Mar. 1996.
- Tapia, J.A. (2002). *Development of the consequent pole permanent magnet machine*. Doctoral thesis, University of Wisconsin-Madison.
- Tokov, M.I. (1975). *Design of electrical machines. Calculations*. LPI (in Russian).
- Ugalde, G., Almandoz, G., Poza, J. and Gonzalez, A. (2009). Computation of iron losses in permanent magnet machines by multi-domain simulations. In: *13th European Conference on Power Electronics and Applications, EPE 2009*.

- Vogt, K. (1983). *Electrical machines. Design of rotating electrical machines (Elektrische Maschinen. Berechnung rotierender elektrischer Maschinen)*, 3rd edn. Berlin: VEB Verlag GmbH.
- Vogt, K. (1996). *Berechnung elektrischer Maschinen*. VCH Verlagsgesellschaft mbH Weinheim.
- Wärtsilä (2009). *Product guide for the diesel engine Wärtsilä 20*. [Retrieved September 20, 2012]. Available at <http://www.wartsila.com/en/engines/medium-speed-engines/Wartsila20>.
- Yamazaki, K. et al. (2012). Estimation of assist effects by additional permanent magnets in salient-pole synchronous generators. *IEEE Transactions on Industrial Electronics*, vol. 59, no. 6, pp. 2515–2523.
- Yiping, D. and Haizhen, C. (2001). A design research for hybrid excitation rare earth permanent magnet synchronous generator. In: *Fifth International Conference on Electrical Machines and Systems (ICEMS)*, vol. 2, pp. 856–589.
- Zhang, Q., Huang, S. and Xie, G. (2010). Design and experimental verification of hybrid excitation machine with isolated magnetic paths. *IEEE Transactions on Energy Conversions*, vol. 25, no. 4, pp. 993–1000.
- Zhao, C. (2010). The research of radial structure HESM of magnetic shunting type. In: *IEEE International Symposium on Industrial Electronics (ISIE)*, Seoul, Korea, pp. 2103–2108.
- Zherve, G.K. (1984). *Industrial tests of electrical machines*. Energoatomizdat (in Russian).
- Zhu, Z.Q. and Chan, C.C. (2008). Electrical machine topologies and technologies for electric, hybrid, and fuel cell vehicles. In: *IEEE Vehicle Power and Propulsion Conference, VPPC 2008*.

Appendix A

A.1 Base values

If the machine RMS rated phase current is I_s and the RMS rated phase voltage is U_s , the base value for

- the current is $I_b = \sqrt{2}I_s$;
- the voltage is $U_b = \sqrt{2}U_s$;
- the angular frequency $\omega_b = 2\pi f_s$;
- the flux linkage is $\Psi_b = \frac{U_b}{\omega_b} = \frac{\sqrt{2}U_s}{2\pi f_s}$;
- the impedance is $Z_b = \frac{U_b}{I_b} = \frac{U_s}{I_s}$;
- the inductance is $L_b = \frac{U_b}{\omega_b I_b} = \frac{U_s}{2\pi f_s I_s}$;
- the capacitance is $C_b = \frac{I_b}{\omega_b U_b} = \frac{I_s}{2\pi f_s U_s}$;
- the apparent power is $S_b = \frac{3}{2}U_b I_b = 3U_s I_s$.

Appendix B

B.1 Definitions of the thermal resistances

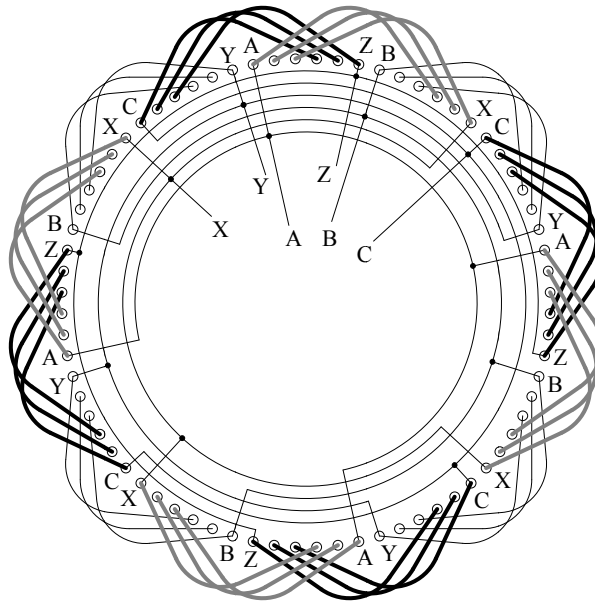
R_{vf}	Radial thermal resistance of the stator yoke and frame
R_{tv}	Radial thermal resistance of the stator teeth and yoke
R_{sv}	Radial thermal resistance of the stator slot and yoke
R_{st}	Tangential thermal resistance of the stator slots and the teeth
R_{tgap}	Radial thermal resistance of the stator teeth and the air gap
$R_{EEp\delta 1}$	Radial thermal resistance of the middle part of the EE pole shoe and the air gap
$R_{EEp\delta 2}$	Radial thermal resistance of the edged part of the EE pole shoe and the air gap
$R_{PMp\delta 1}$	Radial thermal resistance of the middle part of the PM pole shoe and the air gap
$R_{PMp\delta 2}$	Radial thermal resistance of the edged part of the PM pole shoe and the air gap
R_{fp2}	Radial thermal resistance of the compensating winding and the pole shoe
R_{EEp1}	Radial thermal resistance of the EE pole core
R_{EEp2}	Tangential thermal resistance of the EE pole core
R_{fp1}	Tangential thermal resistance of the compensating winding and the pole core
$R_{f\delta}$	Tangential thermal resistance of the compensating winding and the air gap
$R_{br\delta}$	Tangential thermal resistance of the iron bridge and the air gap
R_{PM2}	Tangential thermal resistance of the PM
R_{PM1}	Radial thermal resistance of the PM
R_{PMp2}	Tangential thermal resistance of the PM pole core
R_{PMp1}	Radial thermal resistance of the PM pole core
R_{PMp3}	Radial thermal resistance of the PM pole core and the rotor yoke
R_{EEp3}	Radial thermal resistance of the EE pole core and the rotor yoke
R_{rv3}	Radial thermal resistance of the rotor yoke
R_{rv1}, R_{rv2}	Tangential thermal resistances of the rotor yoke
R_{Fr}	Axial thermal resistance of the frame
$R_{BsFr1,2}$	Thermal resistances between the frame and the bearing shields
R_{InABs}	Thermal resistance between the inner air and the bearing shield
R_{InAFr}	Thermal resistance between the inner air and the frame
$R_{sEndInA}$	Thermal resistance between the stator end winding and the inner air
$R_{rEndInA}$	Thermal resistance between the rotor end winding and the inner air
R_{sEnd}	Axial thermal resistance of the stator winding
R_{rEnd}	Axial thermal resistance of the rotor winding
R_{EEpA}	Axial thermal resistance of the EE pole
R_{PMA}	Axial thermal resistance of the PM
R_{PMpA}	Axial thermal resistance of the PM pole
R_{rvA}	Axial thermal resistance of the rotor yoke
$R_{FrAmb1,2}$	Thermal resistance between the frame and ambient
$R_{BsAmb1,2}$	Thermal resistance between the end shield and ambient

B.2 Definitions of the node numbers

1, 11, 12	Temperature of the frame
2	Temperature of the stator yoke
3	Temperature of the stator teeth
4	Temperature of the active part of the stator winding
5	Temperature of the air gap
6	Temperature of the EE pole core
7	Temperature of the active part of the compensating winding
8	Temperature of the PM
9	Temperature of the PM pole core
10	Temperature of the rotor yoke
13, 20	Temperature of the bearing shields
14, 19	Temperature of the inner air
15, 17	Temperature of the stator end winding
16, 18	Temperature of the rotor end winding

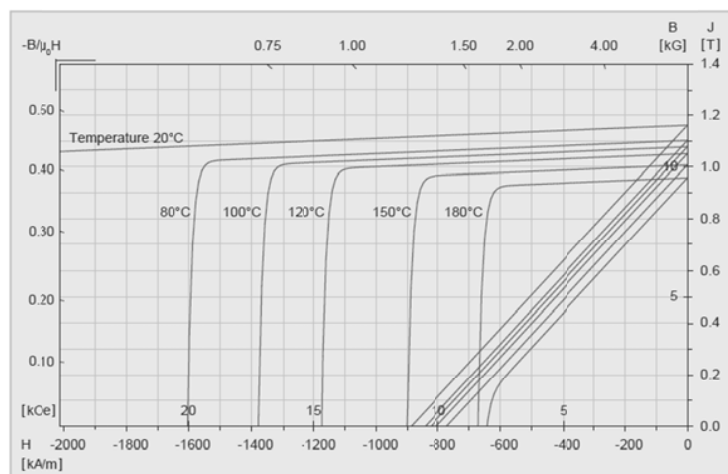
Appendix C

C.1 Stator winding concept of the test machine



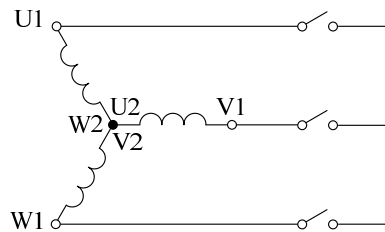
C.2 Properties of Ne795a grade data by Neorem Magnets

Neorem 795a

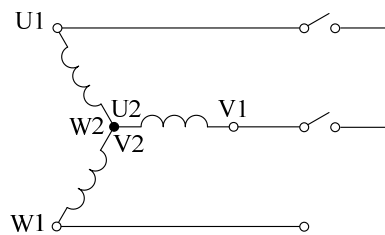


Typical demagnetization curves B(H) and J(H) at different temperatures

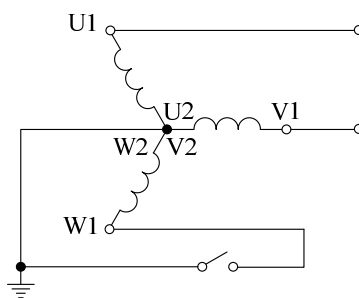
C.3 Electrical schematics of the short circuits



Electrical schematic of the three-phase short circuit.



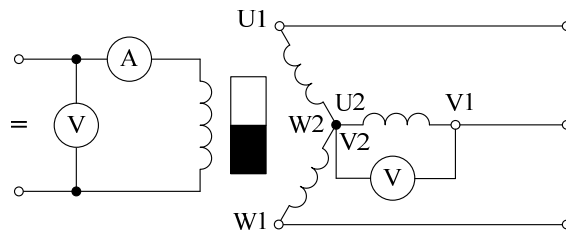
Electrical schematic of the two-phase short circuit.



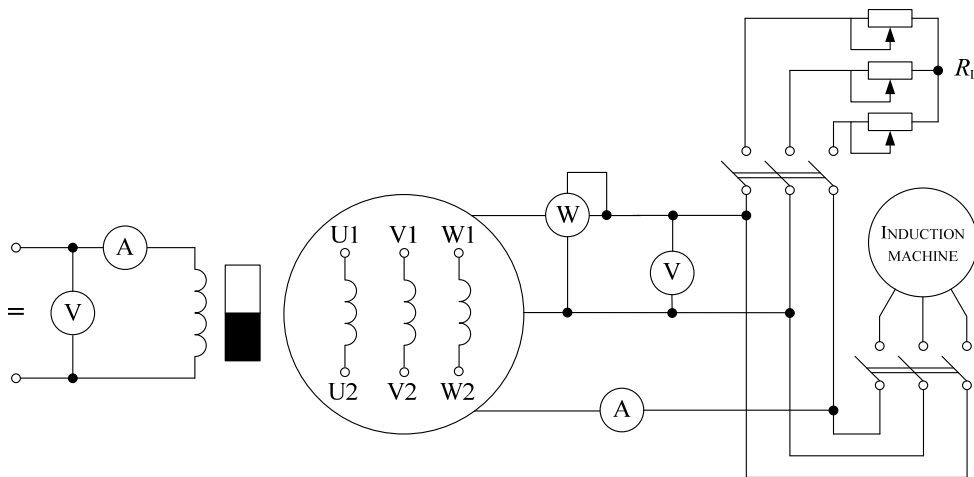
Electrical schematic of the single-phase short circuit.

Appendix D

D.1 Electrical schematic of the no-load tests



D.2 Electrical schematic of the on-load tests



ACTA UNIVERSITATIS LAPPEENRANTAENSIS

498. FEDOROVA, ELENA. Interdependence of emerging Eastern European stock markets. 2012. Diss.
499. SHAH, SRUJAL. Analysis and validation of space averaged drag model for numerical simulations of gas-solid flows in fluidized beds. 2012. Diss.
500. WANG, YONGBO. Novel methods for error modeling and parameter identification of redundant hybrid serial-parallel robot. 2012. Diss.
501. MAXIMOV, ALEXANDER. Theoretical analysis and numerical simulation of spectral radiative properties of combustion gases in oxy/air-fired combustion systems. 2012. Diss.
502. KUTVONEN, ANTERO. Strategic external deployment of intellectual assets. 2012. Diss.
503. VÄISÄNEN, VESA. Performance and scalability of isolated DC-DC converter topologies in low voltage, high current applications. 2012. Diss.
504. IKONEN, MIKA. Power cycling lifetime estimation of IGBT power modules based on chip temperature modeling. 2012. Diss.
505. LEIVO, TIMO. Pricing anomalies in the Finnish stock market. 2012. Diss.
506. NISKANEN, ANTTI. Landfill gas management as engineered landfills – Estimation and mitigation of environmental aspects. 2012. Diss.
507. QIU, FENG. Surface transformation hardening of carbon steel with high power fiber laser. 2012. Diss.
508. SMIRNOV, ALEXANDER. AMB system for high-speed motors using automatic commissioning. 2012. Diss.
509. ESKELINEN, HARRI, ed. Advanced approaches to analytical and systematic DFMA analysis. 2013.
510. RYYNÄNEN, HARRI. From network pictures to network insight in solution business – the role of internal communication. 2013. Diss.
511. JÄRVI, KATI. Ecosystem architecture design: endogenous and exogenous structural properties. 2013. Diss.
512. PIILI, HEIDI. Characterisation of laser beam and paper material interaction. 2013. Diss.
513. MONTO, SARI. Towards inter-organizational working capital management. 2013. Diss.
514. PIRINEN, MARKKU. The effects of welding heat input usability of high strength steels in welded structures. 2013. Diss.
515. SARKKINEN, MINNA. Strategic innovation management based on three dimensions diagnosing innovation development needs in a peripheral region. 2013. Diss.
516. MAGLYAS, ANDREY. Overcoming the complexity of software product management. 2013. Diss.
517. MOISIO, SAMI. A soft contact collision method for real-time simulation of triangularized geometries in multibody dynamics. 2013. Diss.
518. IMMONEN, PAULA. Energy efficiency of a diesel-electric mobile working machine. 2013. Diss.
519. ELORANTA, LEENA. Innovation in a non-formal adult education organisation – multi-case study in four education centres. 2013. Diss.

520. ZAKHARCHUK, IVAN. Manifestation of the pairing symmetry in the vortex core structure in iron-based superconductors. 2013. Diss.
521. KÄÄRIÄINEN, MARJA-LEENA. Atomic layer deposited titanium and zinc oxides; structure and doping effects on their photoactivity, photocatalytic activity and bioactivity. 2013. Diss.
522. KURONEN, JUHANI. Jatkuvan äänitehojakautuman algoritmi pitkien käytävien äänikenttien mallintamiseen. 2013. Diss.
523. HÄMÄLÄINEN, HENRY. Identification of some additional loss components in high-power low-voltage permanent magnet generators. 2013. Diss.
524. SÄRKKÄ, HEIKKI. Electro-oxidation treatment of pulp and paper mill circulating waters and wastewaters. 2013. Diss.
525. HEIKKINEN, JANI. Virtual technology and haptic interface solutions for design and control of mobile working machines. 2013. Diss.
526. SOININEN, JUHA. Entrepreneurial orientation in small and medium-sized enterprises during economic crisis. 2013. Diss.
527. JÄPPINEN, EERO. The effects of location, feedstock availability, and supply-chain logistics on the greenhouse gas emissions of forest-biomass energy utilization in Finland. 2013. Diss.
528. SÖDERHOLM, KRISTIINA. Licensing model development for small modular reactors (SMRs) – focusing on the Finnish regulatory framework. 2013. Diss.
529. LAISI, MILLA. Deregulation's impact on the railway freight transport sector's future in the Baltic Sea region. 2013. Diss.
530. VORONIN, SERGEY. Price spike forecasting in a competitive day-ahead energy market. 2013. Diss.
531. PONOMAREV, PAVEL. Tooth-coil permanent magnet synchronous machine design for special applications. 2013. Diss.
532. HIETANEN, TOMI. Magnesium hydroxide-based peroxide bleaching of high-brightness mechanical pulps. 2013. Diss.
533. TYKKÄLÄ, TOMMI M. Real-time image-based RGB-D camera motion tracking and environment mapping. 2013. Diss.
534. PEKKOLA, SANNA. Performance measurement and management in a collaborative network. 2013. Diss.
535. PANOREL, IRIS CHERRY. Pulsed corona discharge as an advanced oxidation process for the degradation of organic compounds in water. 2013. Diss.
536. TORKKELI, LASSE. The influence of network competence of internationalization of SMEs. 2013. Diss.
537. MOLANDER, SOLE. Productivity and services – safety telephone services for the elderly. 2013. Diss.
538. SITARZ, ROBERT. Identification of research trends in the field of separation processes. Application of epidemiological model, citation analysis, text mining, and technical analysis of the financial markets. 2013. Diss.

